Restoration of Images Taken Through a Turbulent Medium

Author:
Wen, Zhiying

Publication Date:
2010

DOI:
https://doi.org/10.26190/unsworks/23499

Restoration of Images Taken Through a Turbulent Medium

Zhiying Wen

A thesis submitted in fulfilment

of the requirements of the degree of

Doctor of Philosophy

School of Engineering and Information Technology

University College

University of New South Wales

Australian Defence Force Academy

February, 2010

Declaration

I hereby declare that this submission is my own work and to the best of my knowledge it contains no materials previously published or written by another person, or substantial proportions of material which have been accepted for the award of any other degree or diploma at UNSW or any other educational institution, except where due acknowledgment is made in the thesis. Any contribution made to the research by others, with whom I have worked at UNSW or elsewhere, is explicitly acknowledged in the thesis. I also declare that the intellectual content of this thesis is the product of my own work, except to the extent that assistance from others in the projects design and conception or in style, presentation and linguistic expression is acknowledged.

Zhiying Wen
UNSW@ADFA
February, 2010

Acknowledgements

Many, many thanks to my supervisors, A/Prof. Donald Fraser, and Dr. Andrew Lambert, for proposing such a great project and offering amiable and incisive guidance. Thanks to Don for his nice patience and spirit support when I had to do two of the most difficult jobs at the same time: being a PhD student and being a mother of two babies. Thanks to Andrew for his construction of outdoor experiments and providing exciting natural data. Thanks also to them for their kindly, and patiently proofreading and polishing all my paper works. Their supervision, help and support makes it a fantastic three years.

Many thanks also to Dr. Feng Li, Dr. Murat Tahtali, Ph.D candidates David Bowman, and Surasak Prommahorm. Meeting and Discussing with them benefited me and widened my knowledge. Thanks also to Dr. Xiuping Jia for her generous assistance in my research, and in the life in Australia as well.

Huge thanks to my children, Jessica and Alan, for being wonderful after their birth. They always bring happiness to my life. Enormous thanks to my husband, for his love and support throughout my PhD. Also, I gratefully thank my parents, and parents-in-law for their support and help for looking after my children, making me have time for my research.

Last but not least, many thanks to all my friends at UNSW@ADFA, and those who gave me support and friendship, making it such a wonderful experience in my PhD period.

Abstract

This thesis investigates the problem of how information contained in multiple, short exposure images of the same scene taken through (and distorted by) a turbulent medium (turbulent atmosphere or moving water surface) may be extracted and combined to produce a single image with superior quality and higher resolution. This problem is generally termed image restoration. It has many applications in fields as diverse as remote sensing, military intelligence, surveillance and recognition at a long distance, and other imaging problems which suffer from turbulent media, including e.g. the atmosphere and moving water surface. Wide-area/near-to-ground imaging (through atmosphere) and water imaging are the two main focuses of this thesis.

The central technique used to solve these problems is speckle imaging, which is used to process a large number of images of the object with short exposure times such that the turbulent effect is frozen in each frame. A robust and efficient method using the bispectrum is developed to recover an almost diffraction-limited sharp image using the information contained in the captured short exposure images. Both the accuracy and the potential of these new algorithms have been investigated.

Motivated by the lucky imaging technique which was used to select superior frames for astronomical imaging application, a new and more efficient technique is proposed. This technique is called lucky region, and it is aimed at selecting image regions with high quality as opposed to selecting a whole image as a lucky image. A new algorithm using bicoherence is proposed for lucky region selection. Its performance, as well as practical factors that may affect the performance, are investigated both theoretically and empirically.

To further improve the quality of the recovered clean image after the speckle bispectrum processing, we also investigate blind deconvolution. One of the original contributions is to use natural image sparsity as a prior knowledge for the turbulence image restoration problem. A new algorithm is proposed and its performance is validated experimentally.

The new methods are extended to the case of water imaging: restoration of images distorted by moving water waves. It is shown that this problem can be effectively solved by techniques developed in this thesis. Possible practical applications include various forms of ocean observation.

Contents

List of Figures

List of Tables

Chapter 1

Introduction

This thesis studies a special type of image restoration problem, where the input is an image sequence of a scene taken through some turbulent media (e.g., turbulent atmosphere, or moving water surface), and the task is to recover a single clear image by unscrambling information contained (but hidden) in the turbulence-distorted image sequence. Our aim is to develop efficient, robust and automated image restoration techniques and algorithms which can be applied to real turbulent image sequences.

Different from other *generic* image restoration techniques (which have been researched extensively in the digital image processing field), the techniques to be studied in this thesis make special use of the knowledge of the turbulent medium and the imaging process. Thanks to this, we shall see it is not only possible to overcome the effect of turbulence, to reduce noise, to restore high-frequency content, but also increase the spatial resolution and dynamic range as well.

The optical media, which are of central interest to this thesis, include turbulent atmosphere (e.g., convective air currants), and similar media such as moving water waves. In the literature, these two problems (known as *wide-area/near-to-ground imaging* and *water* *imaging* respectively) have been studied mostly separately in their distinct fields with quite different techniques. However, in this thesis we will provide a unified approach that solves both problems in a similar way with almost the same techniques.

To make all the above goals possible, a central technique that has been adopted and further developed in this thesis is the so-called *speckle imaging* technique. Specifically, in using this technique, a sequence of short-exposure images of the scene is taken, the exposure time for each of the frames is so short that the effect of turbulence has been effectively "frozen", and information about the scene can be effectively reconstructed using this short-exposure sequence, as we shall see later.

Two typical forms of speckle imaging methods will be studied in this thesis: the *bispectrum method* and the *lucky region method*. The bispectrum method is essentially a phase recovery technique which uses higher order analysis and "temporal averaging" operation to remove the phase distortion caused by the turbulent medium. The lucky region method is based on selecting and extracting superior image subregions which retain more useful information than the rest for recovering a clear image. In practice, often the result obtained by these two methods may still have some residual blur due to the averaging operation explicitly or implicitly used by both methods, so that a blind deconvolution technique is sometimes applied to further improve the final image quality.

Traditionally, the speckle imaging technique is largely studied in the astronomical observation/imaging field where the targets are often a very small pinpoint or delta function (e.g. a star). In contrast to this, a unique feature of this thesis is that, we are concerned with wide-area, near-to-ground, extended targets (e.g., natural or man-made scenes, street views, buildings, trees, vehicles, pedestrians, etc.). In wide-area/near-to-ground imaging, the object is in wide-field-of view and suffers more severe turbulence than astronomical imagery. Another element is that no prior knowledge of the turbulence, its motion, or its characteristics is assumed. To take advantage of these specialities of our problems to improve the result is another main theme of the thesis. We propose a new method, whose power is demonstrated with both simulated and real image sequences taken through different types of turbulent media (viz., atmospheric turbulence and moving water waves).

1.1 Problem Statement

A simple model for image capture in an optical device, such as a telescope and camera, considers an ideal image to be convolved with a point spread function, or PSF, according to

$$i = o * h + n, \tag{1.1}$$

where i is the recorded image, o is the true image, h is the PSF, $*$ is the convolution operator, and n is a term used to account for various forms of additive noise.

In Eq.1.1, it is assumed that the PSF is position invariant across the image field of view. For imaging through atmospheric turbulence, this requirement is called isoplanatic imaging. In practice, the PSF may well vary across the field of view, which is then known as anisoplanatic imaging. This is because the PSF includes both the inherent behaviour of the telescope, and atmospheric effects. In this case, Eq.1.1 can be considered to approximate conditions over small regions within an image, with a PSF, h, being a function of position within the captured view.

In a typical time sequence of images affected by atmospheric turbulence, the resulting PSF may not only be position dependent, but also rapidly time varying. This makes the restoration problem difficult. However, as each image retains different information of the object and the turbulence, it allows the possibility that an inverse operation may be able to unscramble the intervening effects of turbulence from the necessarily static scene.

The problem of wide-area/near-to-ground imaging, where the objects are near to the Earth's surface and captured over horizontal paths (near-to-ground imaging), is similar to those of ground-based astronomical telescopes. The presence and motion of turbulent eddies between an observing device and the object of interest can introduce severe information loss in imaging by telescope. In this case, a telescope-camera system is usually used. Fig.1.1 is a simple illustration of a common scenario of wide-area/near-to-ground imaging, and Fig.1.2 is a typical observing device.

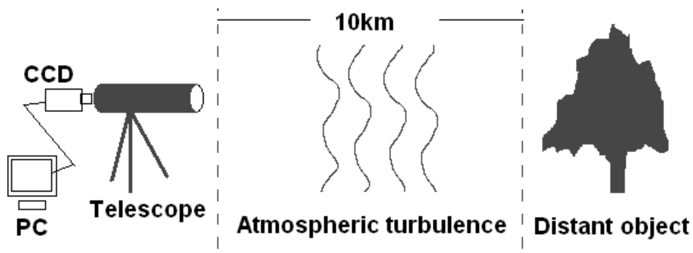

Figure 1.1: Simple illustration of wide-area/near-to-ground imaging.

Figure 1.2: The equipment for wide-area/near-to-ground imaging of turbulence affected scenes at long range. A portable 0.14m dia f14 Cassegrain telescope used in our experiments.

For several decades, researchers have tackled this problem, both with post-processing algorithms, as discussed in this thesis, and by real-time correction techniques employing Adaptive Optics (AO). The AO system senses the wave front deformations and compensates in real time for the deformation. It has been proven to successfully tackle the atmospheric problem experienced over a wide field of view. This technique is not within the scope of this thesis.

A prominent class of post-processing techniques are known as *speckle imaging*, which is also the central technique for this thesis. The name of speckle imaging stems from the fact that, within a narrow optical wavelength band, very short exposure images of an object such as a star, exhibit a speckle pattern resulting from the optical interference due to atmospheric turbulence. (This is true for isoplanatic imaging, while the idea can be generalized to anisplanatic imaging by considering the behaviour within small regions.) The image of an unresolvable star is the PSF of the system, at that position in the image and at that instant of image capture. Each point in a general scene is modified by such a PSF, either varying by region in anisoplanatic imaging, or by direct convolution in isoplanatic imaging. In the simplest case, tip and tilt effects cause the PSF to change location between images, and between regions. However, higher order abberations also detract from image quality.

Fig.1.3 shows a sample sequence of short exposure image. It also provide a long exposure image for comparison. Short exposure images have different characteristics to those of the long exposure image. Short exposure images look 'speckled' in appearance, and have a wider range of spatial frequencies, thus containing finer detail, being less blurred but possibly more noisy. Speckle imaging is a technique to perform image restoration using a number of such short exposure images.

This technique was originally (and largely) studied in the astronomical imagery field. This thesis proposes new methods of using this technique and applies them to our problem. However, the imaging conditions for our wide-area/near-to-ground application are different to most in astronomy, due to its different characteristics.

First of all, wide-area/near-to-ground imaging suffers from much more severe atmo-

(a) A sample sequence of short exposure image

(b) A long exposure image

Figure 1.3: Illustration of short exposure images and a long exposure image.

spheric turbulence than most astronomical imaging, which makes the problem more difficult. This can be explained by the cause and effect of atmospheric turbulence.

The changing temperature of the Earth's surface between night and day is the main driving force of atmospheric turbulence. The Earth's surface heats in the daytime and cools during the night along with the sun as it rises and sets, which leads to changes of air temperature. Temperature fluctuation drives the air to move and so to produce atmospheric turbulence. Moreover, the closer to the Earth's surface, the higher the temperature fluctuation, and the more severe the atmospheric turbulence, which may exist throughout the volume between the observer and the scene.

Images captured by ground-based telescope suffer from atmospheric turbulence. Such effects happen when light propagates through the atmosphere, when it does not have a uniform index of refraction. A moving and turbulent atmosphere can be thought of as consisting of many turbulent eddies of varying size. Eddies can be thought of as regions with different indices of refraction, varying from eddy to eddy. The refractive index of air is particularly sensitive to its temperature, so that eddies resulting from mixing air at varying temperature have varying refractive index. This results in random light wave abberation, which is particularly bad in the wide-area/near-to-ground imaging case. The resulting PSF is also likely to be strongly position-dependent in addition to its time-varying nature.

Secondly, another difference from astronomical imaging is that wide-area imaging deals with near-to-ground, and extended targets. The images of these possess natural image characteristics which can be used as a constraint in image restoration. While in astronomical imaging, the objects of interest are often stars or the Moon or Galaxies, which are far from the Earth and the images may have few natural characteristics (e.g., the stars are usually considered as point source).

The research in this thesis is not limited to atmospheric turbulence. It extends to other turbulent media having similar characteristics to atmospheric turbulence such as a moving water surface. We call the problem of restoration of images distorted by moving water waves as water imaging.

A sample scenario of water imaging is: In a swimming pool lies a static object, a camera is hung still over the water surface and records the object. The water surface is moving (driven by a fan or natural wind), which introduces spatial distortion to images of the object.

As in wide-area/near-to-ground imaging, the effect of moving water surface can be captured with short exposure images (as in Fig.1.4). Each image retains some information of the moving water waves. The mixed information from an image frame stream is then used to remove the distortion.

In both cases, wide-area/near-to-ground imaging and water imaging, besides turbulence, short exposure images suffer another effect: information loss introduced by the instrument. Bandwidth reduction, quantization, frequency aliasing and noise are common degradations found in imaging systems. This effect is fixed compared with the degradation introduced

Figure 1.4: A sample image sequence of water imaging.

by atmospheric turbulence. As a result, an image does not completely record the fine detail of a scene, in the absence of atmospheric turbulence, and is said to have diffraction limited resolution.

The scope of this thesis is to study new and efficient speckle imaging techniques to remove the distortion introduced by a turbulent medium, thus produce a single image that approachs a diffraction limited, or even a high resolution estimate of a scene.

1.2 Thesis Contribution

This thesis studies how to remove the image distortion caused by viewing through turbulent media. It develops several new and efficient techniques to solve the problem. We propose two speckle methods of overcoming the effect of atmospheric turbulence, and one blind deconvolution method for gaining a higher resolution estimate from the result by the speckle methods.

- The bispectrum method for phase recovery is studied and applied to wide-area/near-to-ground imaging.

- A novel technique, the lucky region, is proposed. It favours the condition of wide-area/near-to-ground imaging and has a higher probability of obtaining lucky regions than the classical lucky imaging technique. A new and efficient method, the bicoherence method, is then developed for lucky region selection.

- A blind deconvolution method using a natural image prior is developed to boost high frequency content of an image.

- An original algorithm is proposed for water imaging. For the first time, we apply astronomical techniques (the bispectrum technique and the lucky region) for the restoration of images distorted by moving water waves.

1.3 Constraints and Assumptions

Our work is based on some constraints and assumptions of the imaging system and conditions. This helps better to regularize the problem, leading to improved image restoration results.

Atmospheric turbulence results in a point spread function that varies rapidly, both temporally and spatially, thereby causing each point in a scene to appear to move about randomly when observed over a long period. This thesis assumes that the movement of each point in an image oscillates around a zero-mean displacement from its true position when the observing period is long enough. Similar assumptions are inherent for higher order corrections by the bispectrum.

For the purpose of image restoration for near-to-ground and long range imaging systems affected by atmospheric turbulence, and for imaging through and off water surfaces, this thesis is concerned only with images that are captured under the following conditions:

- The distance between the telescope and the scene is large (typically $> 0.1km$ through to many kilometers), so wide-area effects of the turbulence are present in the imaging. In the same way, rippled water creates similar effects.

- All parts of the scene are within the system's depth of focus.

- The evolution of the media is frozen in each exposure.

- The scene may contain movement but not within the bracket of exposures being used.

1.4 Applications

The research covered in this thesis contributes to wide-area imaging or long-range surveillance, which carries a lot interest in many fields such as remote sensing, military intelligence, and text recognition over a long range, where the observations are degraded and limited by the atmospheric turbulence.

To our knowledge, so far only a few organizations/laboratories in the world have been working in this area. Carrano built up an imaging restoration system to reconstruct a diffraction limited image of an object from a number of short exposure images using the bispectrum technique[1, 2, 3]. The same technique is applied to obtain high-resolution of moving targets[4, 5]. Fienup used phase retrieval methods for the reconstruction of an image taken through atmospheric turbulence[6]. The image restoration problem of atmospheric turbulent video containing real motion has been studied by Fishbain[7, 8, 9, 10]. Fraser and Lambert et al have contributed to long range surveillance and wide-field imaging[11, 12, 13], they proposed an effective method based on locally-nonrigid image registration that has been successfully used for turbulent image restoration. Moreover, Tahtali et al presented an improved Kalman filter for restoration of atmospheric warped images.

Even though a few methods have been proposed, the research in this area remains relatively new: more applications are emerging and few effective techniques are available. In this thesis, we contribute further research of the bispectrum technique and its application to wide-area imaging. Moreover, an original technique and strategy, the lucky region method is proposed. This technique can also be applied to super resolution for turbulent imagery.

An offshoot of the bispectrum approach led to a novel form of image quality measure, namely the mean bicoherence used as a method for determining lucky images or lucky regions of an image. In addition to bispectral phase restoration, selection of superior images or image regions by this approach leads to even better image restoration. The system is useful in long range surveillance, for example in reading text or tracking people at a considerable distance.

The methods developed for restoration of atmospheric turbulence affected images provide an interesting, alternative medium for its application. Light passing through, or reflected from, waves on the surface of a water body, results in distortion and degradation of images in a similar way to atmospheric turbulence. It is shown that image restoration in these cases can be achieved by the techniques developed in this thesis, contributing to various forms of ocean observation.

1.5 Thesis Structure

The remaining chapters and their principal contributions are as follows.

Chapter 2: Survey of Related Work

- A detailed survey is made of the literature pertaining to speckle imaging for optical imaging, and traditional blind deconvolution techniques.

Chapter 3: Bispectral Analysis

- The bispectrum technique is analyzed theoretically. The foundation of the utilization of the averaged bispectrum for the Fourier phase recovery of an object using of interest multiple observations is developed.

  This chapter also describes several available algorithms in detail. Moreover, the phase ambiguity when recovering the Fourier phase from the averaged bispectrum, and the difficulty of data storage and computation when computing the four-dimensional bispectrum of a two-dimensional image are discussed. Finally, the bispectrum technique is tested and results are shown to be impressive.

Chapter 4: Lucky Region and Bicoherence

- An original technique, lucky region, is developed in this chapter. The lucky region technique is based on the idea of the lucky imaging method in astronomical imagery, but improves conditions that fit in our problem. With this technique, the image sequence is divided into a number of smaller subregion sequences. Then superior subregions are selected as lucky regions instead of choosing an entire lucky image. It ensures that lucky region selection and further image processing in subsequent steps are performed in isoplanatic image patches.

  Moreover, a new algorithm using bicoherence, the normalization of the magnitude of the bispectrum, is proposed to be an indicator for predicting the quality of an image region. Lucky regions are selected according to the rank of the bicoherence of each region in the sequence.

  In experiments, we applied the lucky region technique to two cases: image restoration and super resolution for atmospheric turbulence. Both simulated and real-world results are impressive, demonstrating the superior performance of this method in wide-area imaging.

Chapter 5: Imaging Through Turbulent Water Surface

- The methods developed for restoration of atmospheric turbulence affected images provide an interesting, alternative medium for its application: water imaging, image restoration of a still object from a number of images degraded and limited by the moving water surface. Two cases, looking through the water surface and water reflection, are studied and solved in this chapter.

  To our knowledge, this is the first successful attempt at applying higher order statistics, in particular, the bispectrum, for water observation/surveillence. It shows that post processing techniques of astronomical imagery like AO (Adaptive Optics) can also be applied to remove water surface turbulence.

Chapter 6: Image Restoration Using Sparsity

- A new blind deconvolution method is described. This method is applied to remove any remaining blur in the estimate image obtained by the current methods such as the bispectrum technique, which has spatial invariant PSF but may be still low-pass filtered.

  The sparsity in natural image gradient is of importance, and the compressed sensing theory is applied. In particular, the ℓ_1-norm minimization is used in our algorithm. The performance is tested and compared with simulated and real-world data.

Chapter 7: Closing Remarks

- Conclusions of the thesis and several possible avenues of future research are drawn.

1.6 Author's Publications Relevant to the Thesis

- Zhiying Wen, Donald Fraser, and Andrew Lambert, "Bicoherence Used to Predict Lucky Regions in Turbulence Affected Surveillance", IEEE International Conference on Video and Signal Based Surveillance (AVSS 2006), Sydney, Australia. pp. 108, 2006.

- Zhiying Wen, Andrew Lambert, and Donald Fraser, "Reconstruction of Imagery Reflected from Water Surface", in Signal Recovery and Synthesis, Optical Society of America Technical Digest, (OSA 2007), Vancouver, BC, Canada. June, 2007.

- Zhiying Wen, Hongdong Li, Donald Fraser, Andrew Lambert, "Reconstruction of underwater image by bispectrum", IEEE International Conference on Image Processing (ICIP 2007), San Antonio, Texas, USA. Vol. 3, pp. 545-548, September 2007.

- Zhiying Wen, Donald Fraser, and Andrew Lambert, "Restoration of Atmospherically Degraded Images using a Sparse Prior", Applications of Digital Image Processing, Proceeding of Society of Photo-Optical Instrumentation Engineers (SPIE 2008), USA. Vol. 7073, pp. 70731P-70731P-8, 2008.

- Zhiying Wen, Donald Fraser, and Andrew Lambert, "Image Restoration Using Natural Image Statistics", in Signal Recovery and Synthesis, Optical Society of America Technical Digest (OSA 2009), San Jose, California, USA. October, 2009.

- Zhiying Wen, Feng Li, Donald Fraser, Andrew Lambert, Xiuping Jia, "A Super Resolution Algorithm for Atmospherically Degraded Images Using Lucky Regions and MAP-uHMT", IEEE International Conference on Digital Imaging Computing: Techniques and Applications (DICTA 2009), Melbourne, Australia. December, 2009.

- Zhiying Wen, Donald Fraser, and Andrew Lambert, "Bicoherence: A New Lucky

Region Technique in Anisoplanatic Image Restoration", Applied Optics, Vol. 48, No. 32, pp. 6111-6119. November 2009.

- Zhiying Wen, Andrew Lambert, Donald Fraser, and Hongdong Li, "Bispectral analysis and recovery of images distorted by a moving water surface", Applied Optics Vol. 49, No. 33, pp. 6376C6384. November 2010.

Chapter 2

Survey of Related Work

In this chapter, we will give a brief overview of published work for image restoration for images viewed through a turbulent medium, as well as generic image deconvolution. Our focus is given to some relevant techniques developed in the past that are akin to our methods to be researched in this thesis. These relevant techniques are grouped into two categories: speckle imaging techniques and blind deconvolution.

2.1 Speckle Imaging

Since the first short exposure images were measured in the late 1950's in the domain of astronomical observation, remarkable advances have been made in the theoretical understanding of atmospheric turbulence effects in imaging science and the related post processing techniques. The post processing techniques, which are used to overcome the effects of atmospheric turbulence and to reconstruct a clear image of the observed objects from a set of short exposure image frames, are generally termed as "speckle imaging" techniques. The goal of speckle imaging is, in essence, to analyze the information hidden in those captured short exposure images and to recover an estimate of the object (mostly) through the Fourier domain.

Short exposure images refer to images "measured using exposure times short enough to effectively freeze the turbulence, typically on the order of a few milliseconds"[14]. It has been demonstrated that short exposure images contain more high spatial frequency information than long exposure images.

There is also a technique termed as *speckle interferometry* which is closely related to *speckle imaging*, but these two are somewhat different, as they produce different results. Speckle interferometry aims at estimating the modulus spectrum of an object, often through optical means. In contrast, speckle imaging extends this to estimating a true reconstructed image of an object using both modulus and phase information contained in the short exposure images. A more detailed (yet necessarily brief) explanation is given below.

2.1.1 Speckle Interferometry

Speckle interferometry was first proposed by Labeyrie in 1970 to obtain information about binary stars in astronomical imaging. To perform speckle interferometry, two image data sets are required, one is the sequence of short exposure images of the object, and the other is a short exposure image set of a reference star which is bright and nearby to the object [15, 16, 17, 18, 19, 20, 21, 22].

This technique permits the Fourier modulus of an object to be recovered up to the telescope cut-off frequency[23, 24, 14]. In this context, the computation of the averaged power spectrum of the short exposure images is required:

$$< I^{(2)}(u) >=< |I(u)|^2 >= |O(u)|^2 < |H(u)|^2 > \tag{2.1}$$

Recall that in Eq.1.1, $o(x)$ is the true image, $h(x)$ is the point spread function (PSF). $O(u)$ and $H(u)$ are the Fourier transforms of these , respectively. $I^{(2)}(u)$ is the power spectrum, and $I(u)$ is the Fourier transform of the detected image $i(x)$. $< \cdots >$ denotes an ensemble average, and $| \cdot |$ the absolute value.

$< I^{(2)}(u) >$ is the averaged power spectrum of an image set. Assuming additive noise having zero mean, the averaging process will improve the signal-to-noise ratio of the result. If the observed object $o(x)$ is an unresolved source point, e.g., a reference star, then Eq.2.1 yields an estimate of $< |H(u)|^2 >$. Such that $|O(u)|^2$ can be achieved by dividing $|I(u)|^2$ by $|H(u)|^2$.

$H(u)$ is also called the optical transfer function (OTF). The second moment of the OTF, $< |H(u)|^2 >$, is finite out to the telescope cut-off frequency[24, 25]. Thus, $< |I(u)|^2 >$ contains diffraction-limited information about the object if $< |H(u)|^2 >$ is larger than zero for frequencies approaching the telescope cut-off frequency.

Theoretically, $< |O(u)|^2 >$ has a maximum at zero frequency and generally diminishes with the increase of the frequency[23]. The effect of the OTF further attenuates the high frequency content. This can be overcome by using a reference star which is an unresolved source. The reference star should have an irradiance distribution such that it can be considered as a delta function and its Fourier transform is a constant. Using Eq.2.1, $< |H(u)|^2 >$ is estimated. Roggemann has shown that $< |H(u)|^2 >$ is greater than zero up to the telescope cut-off frequency[14].

One may note that dividing by $< |H(u)|^2 >$ boosts the mid and high frequency components of $< I^{(2)}(u) >$, thereby obtaining a better value of $< O^{(2)}(u) >$. This is also the purpose of collecting and processing the short exposure images of the reference data. The absence of zeros in $< |H(u)|^2 >$ maintains the conditioning of the problem.

This method is straightforward and can be extended for general objects, so long as they are not too visually complex. It requires the imaging device having the ability to take short exposure images due to the rapidly changing atmosphere. Also, it requires that one should collect the reference data close to the time and direction of the collection of the object of interest for the purpose of maximizing the coherence of the atmospheric turbulence. The disadvantage is that the "image" is the autocorrelation of the true image, restricting its application to very simple images.

2.1.2 Fourier Phase Estimation Techniques

The speckle interferometry technique only estimates the Fourier modulus of an object. To reconstruct an object faithfully, both the Fourier phase and modulus information are required. In the past decades, various instances of speckle imaging techniques have been proposed to perform the phase recovery task (see e.g. [26] and references therein). Among them, two most promising techniques are the *cross spectrum technique* [27, 28] and the *bispectrum technique* [29, 30, 31]. It has been shown that both preserve (in some scrambled way) the original phase information and high frequency content of the object being imaged, and the key task is to how to recover this[14, 32, 33, 24].

2.1.2.1 Cross Spectrum Technique

The cross spectrum is a special kind of *moment* of the Fourier transform of the images. The cross spectrum of the image of an object provides information of the phase spectrum of the object in the form of point-to-point phase differences[14]. Methods based on the cross spectrum is therefore concerned with how to recover the phase spectrum from the phase differences.

By definition, the cross spectrum of a signal, $C(u, \triangle u)$ is given as

$$\begin{aligned} C(u, \triangle u) &= I(u)I^*(u + \triangle u) \\ &= O(u)H(u)O^*(u + \triangle u)H^*(u + \triangle u) \end{aligned} \tag{2.2}$$

where $\triangle u$ is a small, constant offset spatial frequency. Taking the average over the ensemble images on both sides of Eq.2.2, one then obtains

$$< C(u, \triangle u) > \quad = |O(u)||O(u + \triangle u)|e^{j(\phi_o(u) - \phi_o(u + \triangle u))} < H(u)H^*(u + \triangle u) > \tag{2.3}$$

Here the object spectrum is deterministic, and is taken outside the expectation. In Eq.2.3, $< H(u)H^*(u + \triangle u) >$ is the cross spectrum transfer function. It is shown to be real valued for usual seeing conditions, and non-zero at spatial frequencies approaching the diffraction-limited cutoff frequency[14, 24]. This is an enabling factor for the phase recovery in mid and high frequencies.

Hence, the phase of the averaged cross spectrum is only related with the phase and the phase difference of the object, and clearly encodes the object phase spectrum. To reconstruct the phase spectrum of the object using the cross spectrum, two offset vectors in orthogonal directions are needed[14]. Generally, the u_x and u_y directions are used, and the phase difference is formed by the partial derivative approximations. The offset vectors are often chosen to be equal to a single sample spacing. In practical applications, the phase spectrum can be obtained by recursively calculating the values at higher frequencies based on values at lower frequencies.

It should be pointed out that the cross spectrum is a function of the tilt component of the turbulence-induced aberration. That is, turbulence-induced random tilt causes the recorded image to move randomly about the image plane, but does not affect the image in any other way [14]. This results in attenuation of the averaged cross spectrum. To avoid this, the image sequences are shifted to a centroid before the cross spectrum is computed.

The cross spectrum is often noisy because of poor seeing condition. A treatment of the noise effect is to use multiple offset vectors, but this inevitably leads to the creation of a four-dimensional cross spectrum. More recently, some researchers have recognized that the cross spectrum technique is only a subset (or a special case) of the more general bispectrum technique. People have shown that using the general bispectrum technique usually yields better results [34, 27, 35].

2.1.2.2 Bispectrum Technique

The bispectrum provides another means to preserve the phase information of an object from a sequence of short exposure images of it [14, 36, 37, 34]. Moreover, unlike the cross spectrum, the bispectrum of an image is insensitive to random translation of the image centroid. This makes it particularly suited to removing random translational distortions of an image.

The bispectrum is defined as the Fourier transform of the triple correlation of a signal, i.e.,

$$I^{(3)}(u_1, u_2) \qquad = I(u_1)I(u_2)I^*(u_1 + u_2). \tag{2.4}$$

Temporally averaging the bispectrum over the ensemble images, we have

$$\begin{aligned} < I^{(3)}(u_1, u_2) > \qquad &= |O(u_1)||O(u_2)||O(u_1 + u_2)|e^{j(\phi_o(u_1)+\phi_o(u_2)-\phi_o(u_1+u_2))} \\ &\times < H(u_1)H(u_2)H^*(u_1 + u_2) > \end{aligned} \tag{2.5}$$

where $< H(u_1)H(u_2)H^*(u_1 + u_2) >$ is called the *bispectrum transfer function*.

Similarly to the case of averaging cross spectra, the averaged bispectrum is also real-valued and non-zero up to the cut-off frequency [14, 29, 38, 39]. The phase of the object $\phi_{I^{(3)}}$ is only related to the phase of the temporally averaged bispectrum ϕ_o.

From the above definition, we can make use of some useful properties for recovering phase information. For example, if the phase at a lower spatial frequency is given, then the phase ϕ_o at a higher frequency can be estimated recursively using values at lower frequencies. Detailed method descriptions can be found in [40, 32, 41]. The recursive method is direct but it can introduce large errors at higher frequencies due to error accumulation at lower frequencies[42, 43].

An alternative method is to use the least-squares (LS) method, see e.g., [44, 40]. The LS method ensures that the errors of the obtained bispectral phases are not accumulated for the calculation of each new object phase. This method takes advantage of the linear property of the phase relationship and solves by minimizing a cost function, and will be discussed in detail in chapter 3. The following papers also reported results using the LS method [45, 46, 43, 47, 48, 49].

The LS method has, however, a serious drawback, in the sense that it is not immune to 2π phase ambiguities. The obtained phase spectrum may be subject to unknown 2π phase shifts. Glindemann reviewed several methods that may overcome this phase ambiguity problem [50], for instance, by adding multiples of $\pm\pi$ to Eq.4.16[47, 46], or by recovering phase factors $\exp(j\phi_o)$ instead of the original phases ϕ_o. However, often nonlinear optimization is required for solving for $\exp(j\phi_o)$ in these methods, because no linear relationship between $\exp(j\phi_o)$ and $\exp(j\phi_{I^{(3)}})$[41, 45, 49]. Researchers have also tried to compute the phase difference modulo 2π, see e.g. [51].

A practical issue associated with the bispectrum computation (for a two-dimensional image signal) is that it is very computationally demanding, in the sense that both its memory complexity and time complexity are relatively very high. This has made the bispectrum speckle imaging technique not popular for general PC users. To accelerate the computation, some researchers investigated methods either through algorithm optimization see e.g.[52, 53], or through dedicated parallel hardware see e.g.[54, 55]. In this thesis, we will present a new method based on image. In addition, we will give some analysis of possible parallel computing implementations.

As the bispectrum theory and technique play a central role in our work to be presented in this thesis, Chapter 3 will be fully devoted to this subject. The bispectrum technique has been commonly adopted in the astronomical imaging domain for astronomical image restoration. In contrast, little activity was witnessed in other fields outside the domain. In this sense, this thesis makes a valuable contribution to applying the bispectrum technique to the wide-area/near-to-ground imaging, and to the water imaging application. During the course of this thesis, we also make other important or useful contributions, such as the application of the lucky region method and bicoherence based image quality measure, etc., which are introduced below.

2.1.3 Shift-and-Add Method

There is yet another very popular (and well-known) technique, known as shift-and-add method in optical astronomy for removing atmosphere turbulence effect. It is particularly useful for better observation of binary stars in the sky[56].

As its name suggested, this method is very straightforward, and it consists of (1) firstly find the brightest pixel in one image (termed brightest point) as a reference pin-point, and then (2) the ensemble of a set of short exposure images are shifted with respect to the reference point and then added without any other processing. The averaged centralized version of the images is the so-called shift-and-add resultant image[56].

Various variants of this shift-and-add method were proposed in the literature e.g.[57, 56, 58, 59], and a recent work was done by Bagnuolo [60, 61]. Hunt gave a rigorous theoretical study to the shift-and-add method[62]. It is shown that such a simple method may lead to diffraction-limited restoration[63].

A downside of this method is that the result depends crucially on the seeing conditions. It requires that the observed object should be within an isoplanatic angle of the optical system, therefore the point spread function is position invariant which ensures all the points in an image are distorted in the same way.

However, the effect of atmospheric turbulence on near-ground imaging is often anisoplanatic, and the object of interest is often a natural scene rather than bright stars in the dark sky. In our case, we have found that the shift-and-add method failed to produce a sensible restoration.

Fraser et al[11] proposed an effective method based on locally-nonrigid image registration that has been successfully used for turbulent image restoration for wide-field observations. This method is similar in spirit to the shift-and-add method, but with substantial improvement and practical modifications. It works as follows: randomly select one image from the ensemble images or use the temporal average of the image set as a prototype, then apply region-to-region registration to each pixel in each short exposure image; repeat this process at reducing region size and including more spatial frequency components until the difference of successive images is less than a threshold and finally average the registered images to produce a relatively sharp and geometrically correct image of the object.

This method works well for natural scene images. Moreover, after registration and averaging, the geometrically correct version can be considered as an object imaging through an isoplanatic PSF, therefore a conventional blind deconvolution method may be applied to the geometrically correct version to reconstruct a sharper image. This technique shows quite good results. The main disadvantage is that a large computation time is required for the region-to-region registration, which is computationally expensive.

2.1.4 Lucky Imaging Technique

Lucky imaging, also known as *lucky exposures*, is another popular technique developed for astronomical imaging through turbulence. With the lucky imaging technique, short exposure images which are less affected by the atmosphere and therefore having superior quality are chosen; then a single image is computed by using the typical shift-and-add method. In other words, it is simply applying a pre-selection step to determine which frames come into the shift-and-add process. This technique yields a much higher resolution image than otherwise if pre-selection is not employed.

Fried first mentioned a numerical method for computing the probability of obtaining a lucky image in 1978 [64]. He showed that the probability increases with the data set size (i.e., number of frames). From then on, several ideas based on the lucky imaging technique have been studied. In early applications, the astronomical images were assumed to be blurred by the atmosphere turbulence [65], and the FWHM (Full-Width Half-Maximum) of the images was estimated and used for lucky image selection. More recently, some researchers have taken advantage of the fact that the atmosphere does not "blur" astronomical images, but generally produces multiple sharp but shifted copies of the image [66, 67, 68, 69, 70].

A very successful method in astronomy is to use the Strehl ratio of an image of an unresolved reference or guide star in the field of view to determine lucky images [68, 67]. Because a reference star is needed in this method, it is not applicable to the case of general near-ground imaging, such as in this thesis.

A lucky image based method was presented by Weddell and Webb [69] in connection with an adaptive optics system. A machine learning algorithm/classification model was used to predict when lucky images are expected to occur.

Recently, a synthetic imaging technique used to find lucky patches instead of entire lucky images has been proposed by Vorontsov et al, to achieve the object image with quality superior to the diffraction limited image obtained in the absence of turbulence [70]. A local-area image quality metric based on optoelectronic edge detection is used to locate the image regions having good quality. The lucky patches are then fused together to form a final image using a non-linear evolution partial differential equation (PDE) in the image domain.

In this thesis, we use this idea of partitioning an image into lucky regions, termed the lucky region technique. It improves the conditions of algorithms, and improves the probability of obtaining a lucky region rather than an entire lucky image.

2.2 Blind Image Restoration and Sparsity

In this section, we will give a short overview of blind deconvolution techniques for image restoration, and the use of sparsity as a natural image prior to improve the restoration.

2.2.1 Overview of Blind Deconvolution

In mathematics, deconvolution is an algorithm-based process used to reverse the effects of convolution on recorded data. The concept of deconvolution is widely used in the techniques of signal processing and image processing. In optical imaging, the term “deconvolution” is specifically used to refer to the process of reversing the optical distortion that takes place in an optical microscope, telescope, or other imaging instrument, thus creating clearer images. It is usually done in the digital domain by a software algorithm, as part of a suite of image processing techniques. Early Hubble Space Telescope images were distorted by a flawed mirror and could be sharpened by deconvolution.

The usual method is to assume that the optical path through the instrument is optically perfect, convolved with a point spread function (PSF), that is, a mathematical function that describes the distortion in terms of the pathway a theoretical point source of light (or other waves) takes through the instrument.

In practice, finding the true PSF is impossible, and usually an approximation of it is used, theoretically calculated or based on some experimental estimation by using known probes. When the PSF is unknown, it may still be possible to recover a most probable clear image. This procedure is called blind deconvolution.

Blind deconvolution is an established image restoration technique in astronomy, where the point nature of the objects of interest (i.e, the stars) photographed exposes the PSF, thus making it more feasible.

To put it more formally, the goal of blind deconvolution is to recover a clear version of an object given a single (or a set of) blurred image(s), with little knowledge about the true image and the blur kernel (i.e., the PSF)[71]. Mathematically, it is to solve the o in the following problem:

$$i = o * h + n, \tag{2.6}$$

where o is the true image we are seeking, h is the PSF which acts as a low-pass filter and linear degradation on the true image. n is additive noise, it is usually considered as independent of the signal and identically distributed (iid, independent and identically distributed). h may in fact be a non-linear effect in which case Eq.2.6 becomes more complicated.

The study of the feasibility of blind deconvolution dates back to 1970s when Oppenheim et al.[72] and Stockham et al.[73] proposed to estimate a single image by superimposing a set of images in combination with homomorphic filtering. In the 1980s, Lane and Bates theoretically demonstrated blind deconvolution can be performed using only one image. From then on, many methods have been published[74]. Ayers and Dainty first gave a general deconvolution scheme of iterative algorithms estimating both the image and the PSF in their paper of 1988[75]. Their method exploits the Fourier phase of the convolution and uses some general a priori information concerning the object image and the PSF such as there being no negative pixel value allowed in the image domain. More recent algorithms such as maximum likelihood (ML) and maximum a posteriori (MAP) can be considered as an extension of such iterative techniques.

In its most general formulation, image blind deconvolution is an ill-posed (under-constrained) problem: there are more unknowns than measurements, i.e., the original image o and the PSF h are unknown while the observed blurred image i is known. There exist infinitely many solutions to Eq.2.6. Hence, to obtain a reasonable result, algorithms make strong prior assumptions about the blur kernel and the original image.

Image blind deconvolution also suffers from reconstruction artifacts such as "ringing" effects or color speckles which are a result of high frequency content being lost in the degraded image. This phenomenon is commonly found in almost all algorithms, even in the standard non-blind deconvolution algorithms. For example, more iterations in the famous Richardson-Lucy algorithm will result in more "ringing" artifacts. This is because most non-blind deconvolution methods assume the PSF contains no errors, however, even small errors in the PSF or noise in image can lead to significant artifacts[76].

In the past three decades, two kinds of methods have been commonly studied and used in the various approaches to the problem: the maximum likelihood (ML) technique and the maximum a posteriori (MAP) technique.

2.2.1.1 ML Method

In general, the maximum likelihood (ML) technique is to find the estimate $o'(x, y)$ that is most likely to produce the detected image $i(x, y)$. In the literature, this method has been widely used in non-blind deconvolution. Given the detected image and the PSF, and some simple prior knowledge such as the true image f being positive may be imposed when seeking[77]

$$arg\max_{o} P(i|o) \tag{2.7}$$

where $P(\cdot)$ denotes the probability. Assume there exists image dependent Poisson noise, such that the likelihood of $i(x, y)$ is expressed as[77]

$$o' = arg\max_{o'} \sum_{x,y} i \times log(h * o') - h * o' \tag{2.8}$$

A number of approaches have been proposed for solving this problem, for example the famous Richardson-Lucy algorithm[78, 79]. These methods are all essentially iterative. Some researchers utilize the expectation maximization (EM) technique for maximizing the log likelihood[80, 81]. The E and M steps are updated in each iteration based on the estimate of the previous step[82].

One shortcoming of the iterative method is its slow convergence to the maximum of the likelihood function. To speed up the convergence, one solution is to use more efficient techniques such as steepest ascent search or the conjugate gradient method. Also, in order to ensure the image is positive, another constraint (the true image o is expressed as the square of another function) should be added [83]. More recently, new ML methods have been presented for blind deconvolution, for example, Holmes has derived a ML algorithm to solve for both the unblurred image and the PSF in the presence of Poisson statistics[84].

2.2.1.2 MAP Method

Given a detected image i, maximum a posteriori (MAP) technique or Bayesian estimation is to use Bayes' rule and maximize the probability of the true image o and the PSF h given a detected image i

$$P(o,h|i) = \frac{P(i|o,h)P(o)P(h)}{P(i)} \tag{2.9}$$

Taking the logarithm of both sides in Eq.2.9 and discard the term $log(p(i))$ for the reason that it is determined, then the problem now becomes one of minimizing the sum of negative log likelihood:

$$o \quad = arg\min_o[L(i|o,h) + L(o) + L(h)] \tag{2.10}$$

where $L(i|o,h)+L(o)+L(h)$ is the cost function or penalizing function, $L(i|o,h)$ is the data term or likelihood penalty, and $L(o)$ and $L(h)$ are the priori knowledge about the object and the PSF respectively, also called the regularization penalty.

Methods based on the above model have been published [85, 86, 87, 88, 76], and they have led to great progress in blind deconvolution. But the results are still far from perfect due to the limitation of existing algorithms[89]. An alternative strategy has been proposed in [89]: that is, apply MAP to estimate the PSF using the knowledge at hand, then solve for the estimate of the true image using general doconvolution techniques with the computed PSF. In estimation theory, the MAP method will approach the true solution given enough measurements. Therefore, if the image size is large enough (compared to the PSF support), it has increasing probability to solve for a correct PSF using all the information the detected image provides.

In fact, some recent algorithms make use of this specific strategy. For example, Fergus et.al. proposed an algorithm with two steps which are exactly mentioned by Levin to remove camera shake from a single photograph [85]. Another example is the use by Yuan et.al.

[90] of the same strategy for motion blur removal. Results are impressive, moreover, the algorithm proposed by Yuan et.al. greatly reduces the "ringing" artifacts that commonly result from image deconvolution.

2.2.2 Exploit Sparsity in Natural Image Restoration

Due to the ill-posed nature of the blind image restoration problem, the more prior knowledge about the original image and/or the blur kernel, the better we can constrain the problem, and the better restoration result we can obtain. Using natural image prior in the blind deconvolution computation is exactly based on such an idea. In this thesis, we will examine the sparsity prior, which is enjoyed by most natural scenes, and has received increasing attention from recent researchers in the image restoration area.

The image gradient distribution information has long been used in solving image restoration problems. Often, a regularization term $L(o)$ on the image gradients is introduced in Eq.2.10:

$$L(o) = ||\nabla o||^q \tag{2.11}$$

when $q = 1$, it is a Laplacian prior, and when $q = 2$ it means a Gaussian prior. These two priors are used in several methods. However, recent research pointed out that real world natural image gradients are always non-Gaussian, but favours a sparse or heavy-tailed distribution. Moreover, when q falls in the range of $[0.5, 0.8]$ the algorithm gives a more "natural" result [86, 91, 92].

In recent years, such sparsity prior has been applied successfully in various topics of imaging processing [76, 85, 86, 90, 93, 94, 95, 96, 97, 98, 99, 100]. Yuan et al. used the sparse prior to search the best alignment for a blurred/non-blurred image pair, which produces a sparse kernel[90, 97]; methods proposed in [96, 76, 86] employed the sparse statistics for motion deblurring from a single image or an image pair; Tappen et al. and Yang et al. extended the application of sparsity to image super-resolution and image demosaicing[93, 99]. Other applications using sparseness include image inpainting and zooming[94], and camera shake removal[85].

Motivated by the success of these methods in the literature, we study and exploit the use of such sparsity in wide-area turbulent imaging.

However, we cannot directly apply the classic blind deconvolution technique to turbulence distorted images, because the effective PSF varys both spatially and temporally. To overcome this, one could segment an image into a number of smaller subregions where the PSF for each small region can be roughly considered as position-invariant, then perform multiple image blind deconvolution methods to the subregion sequence to obtain a single potential image. Alternatively, one could perform the deconvolution on a single geometrically-correct image of the object, obtained after using the speckle imaging (phase-recovery) techniques. Our method to be presented in Chapter 6 of this thesis follows from the second approach.

Chapter 3

Bispectral Analysis

3.1 Introduction

Due to the nature of atmospheric turbulence, the effective PSF for each image of a short exposure sequence almost always varies from time to time, and the PSF itself of each image is also spatially non-uniform (i.e., inhomogeneous). Classical image deblur techniques (e.g., Wiener filter) cannot be directly applied here, as they often assume a spatially invariant PSF. To overcome the disruption caused by atmospheric turbulence and recover an distortion-free estimation of the true image, novel techniques are needed.

Motivated by the success of applying higher order statistics (HOS) to various signal processing and system theory problems, and inspired by the particular application of speckle imaging technique to astronomical imagery field, we investigate the bispectrum in its ability to correct the effects of atmospheric turbulence in wide-area/near-to-ground imaging.

Literature study shows that higher order statistics is very powerful particularly when Gaussian or zero-mean noise exists, or phase distortion occurs, and when nonlinearities are relevant [101]. We shall see that this is exactly so in the case of imaging through turbulent media.

In this thesis, we make extensive use of third-order statistics, i.e., the 3rd-order moment (a.k.a. triple correlation), for which the counterpart in the frequency domain is called *bispectrum*.

Compared with the conventional (thus lower-order) power spectrum, which encodes only the magnitude but not the phase part of the Fourier transform of the object (signal), the bispectrum retains both the magnitude and the phase information [101]. For a turbulence affected image, the geometrical distortion caused by the turbulence is in fact some unknown and random phase aberrations. Through a standard single frame image recording process, the phase information of the original target image may be lost. However, taking a large number of short exposure images of the same target can somehow compensate for the effect of random phase aberrations, assuming the aberrations are zero-mean or Gaussian distributed. As we will see, using the averaged bispectrum of multiple short exposure images can successfully recover the phase spectrum. Then, in conjunction with the averaged power spectrum, one can improve the overall image quality, and signal-to-noise ratio, of the reconstructed target object substantially.

This chapter will revisit the bispectrum technique, and theoretically demonstrate how it removes the effect of atmospheric turbulence and suppresses additive noise, show the means of reconstruction of the phase spectrum from the averaged bispectrum of the recorded images, and discuss the phase ambiguity and computation problems when that occurs in this case.

3.2 Introduction to Fourier Theory

Before introducing the concept and definition of bispectrum, it is necessary and beneficial to first briefly review the classical Fourier theory. Fourier transform is of significant importance in signal processing, as well as in image processing. Both concepts of bispectrum and bicoherence that are relevant to this thesis, are defined in the Fourier space.

3.2.1 Fourier Transform and Discrete Fourier Transform

Given a continuous function $f(x)$ defined on a domain variable x, its Fourier transform $F(u)$ is defined as

$$F(u) = \int_{-\infty}^{\infty} f(x)e^{-j2\pi ux}dx \tag{3.1}$$

where $j = \sqrt{-1}$. Inversely, given $F(u)$, one can obtain $f(x)$ via the inverse Fourier transform, which is defined as

$$f(x) = \int_{-\infty}^{\infty} F(u)e^{j2\pi ux}du \tag{3.2}$$

The functions $f(x)$ and $F(u)$ comprise a Fourier transform pair, and the variables x and u are called conjugate in this context. These definitions are easily extended to a two-dimensional Fourier transform pair $f(x, y)$ and $F(u, v)$:

$$F(u,v) = \int_{-\infty}^{\infty}\int_{-\infty}^{\infty} f(x,y)e^{-j2\pi(ux+vy)}dxdy \tag{3.3}$$

$$f(x,y) = \int_{-\infty}^{\infty}\int_{-\infty}^{\infty} F(u,v)e^{j2\pi(ux+vy)}dudv \tag{3.4}$$

When f is a discrete and finite function of variable(s) $x = \{0, 1, 2, ..., M-1\}$, $(y =$

$\{0, 1, 2, ..., N-1\}$ for a two-dimensional function), the one-dimensional and two-dimensional Fourier transforms are defined by

$$F(u) = \frac{1}{M} \sum_{x=0}^{M-1} f(x) e^{-j2\pi ux/M} \tag{3.5}$$

$$f(x) = \sum_{u=0}^{M-1} F(u) e^{j2\pi ux/M} \tag{3.6}$$

$$F(u, v) = \frac{1}{MN} \sum_{x=0}^{M-1} \sum_{y=0}^{N-1} f(x, y) e^{-j2\pi(ux/M+vy/N)} \tag{3.7}$$

$$f(x, y) = \sum_{u=0}^{M-1} \sum_{v=0}^{N-1} F(u, v) e^{j2\pi(ux/M+vy/N)} \tag{3.8}$$

where $u = \{0, 1, 2, ..., M-1\}$, and $v = \{0, 1, 2, ..., N-1\}$ are discrete samples of $F(u, v)$, and Eqs.3.5-3.8 describe the DFT (Discrete Fourier Transform). We consider the values of u (and v) to be in the frequency domain or Fourier space, and each term of $F(u)$ (and $F(u, v)$) is a frequency component.

In practice, it is convenient to express $F(u)$ in complex polar form:

$$F(u) = |F(u)| e^{j\phi(u)} \tag{3.9}$$

where $|F(u)|$ is called the *magnitude* of the Fourier transform, and $\phi(u)$ is the phase or phase spectrum.

For a real signal, $f(x)$, one has $F^*(u) = F(-u)$, where F^* represents the complex conjugate of F. Similarly, we can write $F(u, v) = |F(u, v)| e^{j\phi(u,v)}$, and, again, for a real signal, $f(x, y)$, $F^*(u, v) = F(-u, -v)$.

3.2.2 Convolution and Correlation

Convolution and correlation are very important concepts in Fourier theory. For example, the auto-correlation (in space domain) and power spectrum (in Fourier domain) are a pair of conjugate operations. Similar analogy regarding higher-order statistics can frequently be found in this thesis. Let us first review the standard definition of the conventional convolution and correlation operators.

Let $*$ and $\otimes$ denote convolution and correlation, respectively. For two one-dimensional functions $f = f(x)$ and $g = g(x)$, these two operations are defined by

$$f * g = \int_{-\infty}^{\infty} f(x)g(\xi - x)dx \tag{3.10}$$

$$f \otimes g = \int_{-\infty}^{\infty} f(x)g(x + \xi)dx \tag{3.11}$$

Note that $f * g$ and $f \otimes g$ are functions of ξ, and $f * g$ is commutative, i.e., taking either f or g first will not affect the output. Writing the Fourier transform of f and g as $G = G(u)$ and $F = F(u)$ respectively, the convolution theorem and the correlation theorem are then expressed as

$$\int_{-\infty}^{\infty} (f * g)e^{-j2\pi ux}dx = F(u)G(u) \tag{3.12}$$

$$\int_{-\infty}^{\infty} (f \otimes g)e^{-j2\pi ux}dx = F(-u)G(u) \tag{3.13}$$

In two dimensions, the convolution and correlation operations can be defined in the same way as

$$f * g = \int_{-\infty}^{\infty}\int_{-\infty}^{\infty} f(x, y)g(\xi - x, \eta - y)dxdy \tag{3.14}$$

$$f \otimes g = \int_{-\infty}^{\infty}\int_{-\infty}^{\infty} f(x, y)g(x + \xi, y + \eta)dxdy \tag{3.15}$$

here, f and g denotes two-dimensional functions, i.e., $f = f(x, y)$ and $g = g(x, y)$.

3.3 Higher Order Statistics (HOS)

We now give the definitions of higher order statistics (e.g., moments and cumulants) used in this thesis. In particular, bispectrum and triple-correlation will be explained next, which play central roles in our work.

A well-known result in signal processing is that the Power spectrum and the auto-correlation of a signal form a Fourier transform pair. Similarly, the bispectrum and the (auto) triple correlation of a signal also constitute a Fourier transform pair. More detailed development is given below.

3.3.1 Moments and Cumulants

Given a set of n real random variables $\{x_1, x_2, \cdots, x_n\}$, their *joint moments* are defined by [101]

$$\begin{aligned} Mom[x_1, x_2, \cdots, x_n] &\triangleq E\{x_1 x_2 \cdots x_n\} \\ &= (-j)^n \frac{\partial^n \Phi(w_1, w_2, \cdots, w_n)}{\partial w_1 \partial w_2 \cdots \partial w_n}|_{w_1 = w_2 = \cdots = w_n = 0} \end{aligned} \tag{3.16}$$

where $E\{\cdot\}$ is the mathematical expectation operation, and $\Phi(w_1, w_2, \cdots, w_n)$ the joint characteristic function given by

$$\Phi(w_1, w_2, \cdots, w_n) \triangleq E\{e^{j(w_1 x_1 + w_2 x_2 + \cdots + w_n x_n)}\} \tag{3.17}$$

The *joint cumulants* are defined as

$$Cum[x_1, x_2, \cdots, x_n] = (-j)^n \frac{\partial^n \Psi(w_1, w_2, \cdots, w_n)}{\partial w_1 \partial w_2 \cdots \partial w_n}|_{w_1 = w_2 = \cdots = w_n = 0} \tag{3.18}$$

where $\Psi(w_1, w_2, \cdots, w_n)$ is the natural logarithm of $\Phi(w_1, w_2, \cdots, w_n)$

$$\Psi(w_1, w_2, \cdots, w_n) \triangleq ln[\Phi(w_1, w_2, \cdots, w_n)] \tag{3.19}$$

If $X(k), k = 0, \pm 1, \pm 2, \pm 3, \cdots$ is a real stationary random process, then its moments will depend only on the time difference ($t_i = 0, \pm 1, \pm 2, \cdots$):

$$m_n^X(t_1, t_2, \cdots, t_{n-1}) \triangleq E(X(k)X(k+t_1)\cdots X(k+t_{n-1})) \tag{3.20}$$

Similarly, the cumulants of $X(k)$ can be defined as:

$$c_n^X(t_1, t_2, \cdots, t_{n-1}) \triangleq Cum(X(k), X(k+t_1), \cdots, X(k+t_{n-1})) \tag{3.21}$$

The cumulants and the moments relate to each other in some way, for example,

$$\begin{aligned} c_2 &= Cum[x_1, x_1] = Mom[x_1, x_1] - Mom^2[x_1] \\ c_3 &= Cum[x_1, x_1, x_1] = Mom[x_1, x_1, x_1] - 3Mom[x_1, x_1]Mom[x_1] + Mom^3[x_1] \end{aligned} \tag{3.22}$$

The Fourier transforms of cumulants are termed *cumulant spectra*, also known as polyspectra (see [101]). The Fourier transforms of c_2 and c_3 in Eq.3.22 are

$$\begin{aligned} C_2(w) = \textstyle\sum_{t=-\infty}^{\infty} c_2(t)e^{-j(wx)} \\ -\pi < w \leq \pi \end{aligned} \tag{3.23}$$

$$\begin{aligned} C_3(w_1, w_2) = \textstyle\sum_{t_1=-\infty}^{\infty} \sum_{t_2=-\infty}^{\infty} c_3(t_1, t_2)e^{-j(w_1x_1 + w_2x_2)} \\ -\pi < w_1 \leq \pi, -\pi < w_2 \leq \pi, -\pi < w_1 + w_2 \leq \pi \end{aligned} \tag{3.24}$$

$C_2(w)$, is the familiar power spectrum, and Eq.3.24 is the definition of the bispectrum.

3.3.2 Power Spectrum and Bispectrum

The development of cumulants and polyspectra has paralleled the development of traditional correlation. Some techniques and operations may have very different terms in different areas, such as autocorrelation refers to c_2 in HOS (higher order statistics), and triple correlation means c_3. These two terms are of significant importance in our research, so that the alternative definitions are given here. Denote $f^{(2)}$ as the common autocorrelation of a signal $f(x)$, and $f^{(3)}$ for the triple correlation (these notations will be used in the remainder of this chapter and this thesis).

The autocorrelation of a real signal and its Fourier transform $F^{(2)}$ are given by

$$f^{(2)}(\xi) = f * f = \int_{-\infty}^{\infty} f(x)f(x+\xi)dx \tag{3.25}$$

$$\begin{aligned} F^{(2)}(u) &= \int_{-\infty}^{\infty} f^{(2)}(\xi)e^{-2\pi u\xi}d\xi \\ &= F(u)F^*(-u) \\ &= |F(u)|^2 \end{aligned} \tag{3.26}$$

where $F^*(u)$ is the conjugate of $F(u)$. In Eq.3.26, for a real signal, we have $F(u) = F^*(-u)$ and finally have $F^{(2)}(u) = |F(u)|^2$. Note that, in this thesis, we only discuss real signals.

In the same way, the auto triple correlation is defined

$$f^{(3)}(\xi_1, \xi_2) = \int_{-\infty}^{\infty} f(x)f(x+\xi_1)f(x+\xi_2)dx \tag{3.27}$$

and the Bispectrum, the Fourier transform of the triple correlation is written as

$$
\begin{aligned}
F^{(3)}(u_1, u_2) \quad &= \int_{-\infty}^{\infty}\int_{-\infty}^{\infty} f^{(3)}(\xi_1, \xi_2) e^{-2j\pi(u_1\xi_1+u_2\xi_2)} d\xi_1 d\xi_2 \\
&= F(u_1)F(u_2)F^*(u_1+u_2) \\
&= F(u_1)F(u_2)F(-u_1-u_2) \\
&-\pi < u_1 \leq \pi, -\pi < u_2 \leq \pi, -\pi < u_1+u_2 \leq \pi.
\end{aligned} \tag{3.28}
$$

This definition can be expanded to a two-dimensional real signal, for example, an image, $i(x, y)$

$$
\begin{aligned}
I^{(3)}(u_1, u_2; v_1, v_2) &= I(u_1, u_2)I(v_1, v_2)I^*(u_1+v_1, u_2+v_2) \\
&= I(u_1, u_2)I(v_1, v_2)I(-u_1-v_1, -u_2-v_2)
\end{aligned} \tag{3.29}
$$

where I is the Fourier transform of i, and $I^{(3)}$ denotes the bispectrum.

For signals which fluctuate heavily in the process of observation, the signal spectrum provides useful energy information. In speckle image processing, for example, many short exposure images of an object of interest are taken forming a time sequence of images. When atmospheric turbulence exists, the long time average $< F(u) >$ may be heavily low-pass filtered. On the other hand, the long time average $< |F(u)|^2 >$ of the image sequence includes more high frequency information[14]. However, the double spectrum completely suppresses phase information.

In sharp contrast to the power spectrum, phase information of an object is *retained* in the bispectrum, which allows possible phase retrieval in speckle image processing. In the next section, we will discuss this process.

3.3.3 Why Bispectrum in Signal Processing

The bispectrum has of great importance in the analysis of deterministic and stochastic signals in various areas such as: sonar, radar, plasma physics, biomonic retrieval, array processing, etc. One naturally might ask why it is so useful.

In general, there are three major motivations in the use of the bispectrum in signal processing[101, 102]. The bispectrum:

- Suppresses Gaussian noise, and suppresses non-Gaussian noise with symmetric probability density function;
- Retains the phase information of signals;
- Detects nonlinearities in signals.

In theory, as we shall see later, all higher order polyspectra (≥ 3) of a Gaussian noise are identically zero. The bispectrum of a non-Gaussian signal therefore can remove any additive Gaussian noise over the ensemble of measurements to recover a high SNR signal[101, 29]. If non-Gaussian noise exists, the averaged bispectrum also eliminates the noise. A special case (zero-mean noise) will be discussed in the following section.

The bispectrum preserves the true phase character of signals. Rewrite Eq.3.28 as (for real signals)

$$\begin{aligned} F^{(3)}(u_1, u_2) &= |F(u_1)F(u_2)F(-u_1-u_2)|e^{j(\phi(u_1)+\phi(u_2)-\phi(u_1+u_2))} \\ &= |F^{(3)}(u_1, u_2)|e^{j\beta(u_1,u_2)} \end{aligned} \tag{3.30}$$

where ϕ is the Fourier phase of the signal, and β is the bispectrum phase. From Eq.3.30, β can be expressed by the simple addition/subtraction on ϕ at any two indices, u_1, u_2 and their sum $u_1 + u_2$

$$\phi(u_1) + \phi(u_2) - \phi(u_1 + u_2) = \beta(u_1, u_2) \tag{3.31}$$

Eq.3.31 implies that, ϕ can be inversely computed if the value of ϕ at direct component ($\phi(0)$) and the first order components ($\phi(1)$ and $\phi(-1)$) are given, since β is deterministic and can be obtained from the recorded data.

HOS can play a key role in nonlinearity detection in a system or signals[101]. In practical applications, the normalization of the bispectrum, called the bicoherence, is usually used. This will be the focus of Chapter 4.

In this thesis, the bispectrum is applied to wide-area turbulent image reconstruction; Its normalized version, i.e., the *bicoherence*, is used to detect the image phase distortion caused by turbulence.

3.3.4 Properties of the Bispectrum

Four dimensional. One may have noticed that the bispectrum of a two-dimensional signal will be four dimensional, which will need large memory for data storage in a computer. For example, the bispectrum of an image of size of 256×256 pixels is $256 \times 256 \times 256 \times 256$, which equals 4G pixels just to store the bispectrum. This large memory usage makes currently available personal computers unsuitable for the task. If virtual memory is used, it significantly limits computation speed due to page-swapping. This is the main reason that the bispectrum technique is not widely applied in many practical situations, especially for real-time systems.

In general application, this difficulty can be reduced by the basic properties of the bispectrum itself. In fact, the bispectrum is 11/12 redundant[29].

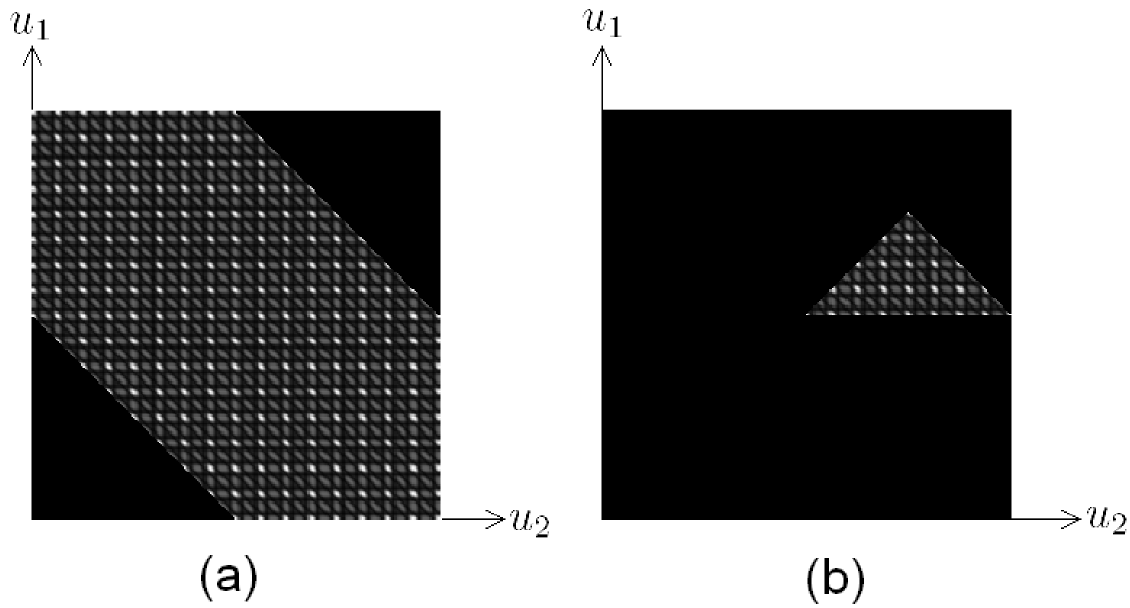

Figure 3.1: The bispectrum of a real signal is 1/12 non-redundant. Instead, to compute the whole section of the bispectrum in (a), it is only necessary to compute one twelfth subsection of it, as in (b).

Symmetry. The bispectrum is symmetric:

$$\begin{aligned} F^{(3)}(u_1, u_2) &= F^{(3)}(u_2, u_1) \\ &= F^{(3)}(-u_1 - u_2, u_1) \end{aligned} \tag{3.32}$$

this results in a bispectrum that is 3/4 redundant. If the signal $f(x)$ is real, the bispectrum is Hermitian

$$F^{(3)}(u_1, u_2) = (F^{(3)}(-u_1, -u_2))^* \tag{3.33}$$

in this case, only 1/12 of $F^{(3)}(u_1, u_2)$ is non-redundant. This property enable to save large computation time and data storage in a computer when we compute the bispectrum of a real signal, especially for two-dimensional signals. Fig.3.1 displays the magnitude pattern in the bispectrum of a one-dimensional signal. One only needs to compute a one twelfth subsection of the whole bispectrum as shown in Fig.3.1 (b).

3.4 Bispectra for Speckle Imaging

This section will provide a theoretical explanation of the use of the bispectrum in speckle imaging. The theory will be demonstrated both in the spatial domain and the Fourier domain (, using the triple correlation and the bispectrum, respectively).

3.4.1 Speckle Masking

Speckle masking is a traditional method to obtain a diffraction-limited image of the object used in astronomy imagery. It is mainly performed in the Fourier domain using the averaged bispectra of speckle interferograms [29, 30, 31, 103]. This subsection develops the theory of speckle masking which also inspires the bispectrum method that we will discuss in the next subsection.

In speckle masking, the images are evaluated in such a way that the phase of the object can be preserved: Let s and $s' = s + \Delta s$ replace ξ_1 and ξ_2 in Eq.3.27, we have

$$\begin{aligned} f^{(3)}(s, s') &= f(s, s + \Delta s) \\ &= \int f(x) f(x+s) f(x+s+\Delta s) dx \\ &= [f(s) \cdot f(s+\Delta s)] * f(s) \\ &= [f(s) \cdot f(s')] * f(s) \end{aligned} \tag{3.34}$$

where $f(s) \cdot f(s+\Delta s)$ is called the mask, and Δs is known as the masking vector.

The theory of speckle masking is illustrated by a simple example in Fig.3.2. Usually, masking vector is well selected to ensure that the mask approximates a δ function. Therefore, one reaches the following results:

$$f(s) \cdot f(s + \Delta s) \approx \delta(s) \tag{3.35}$$

$$f(s) \cdot f(s + \Delta s) * f(s) \approx f(s) \tag{3.36}$$

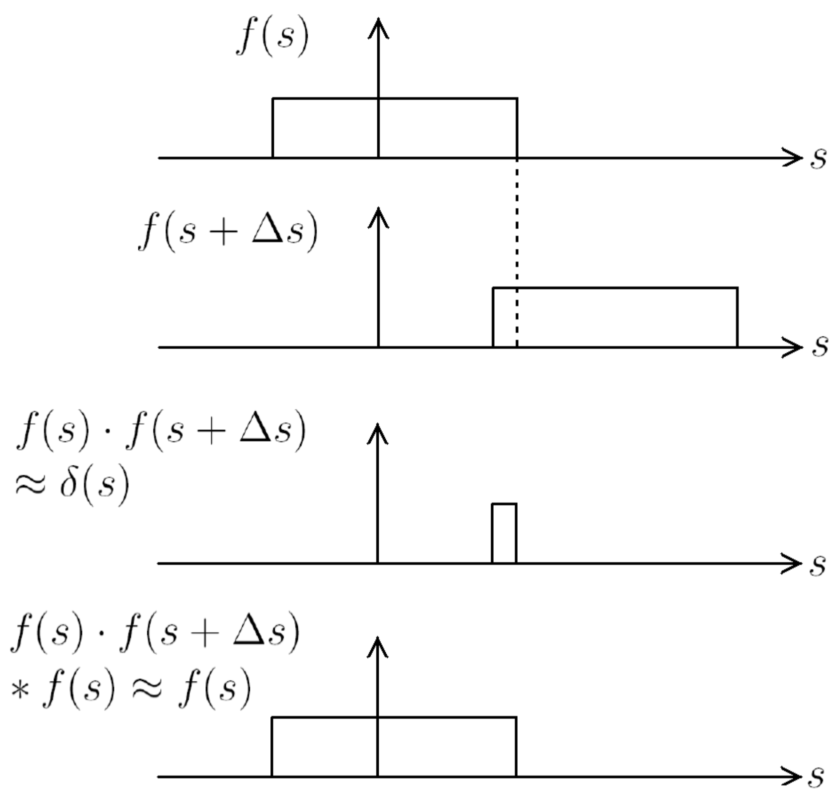

Figure 3.2: Illustration of the speckle masking method. A function is able to be recovered from its triple correlation if an appropriate masking vector Δs is carefully selected.

Equivalently, in the Fourier domain we have $F^3(u, \Delta u) \approx F(u)$. Such that the true image is recovered from its bispectrum, if the masking vector is suitably selected[103].

However, in practical applications, Δs is difficult to determine in such a way that the mask approximates a δ function. Often, it is advisable to test a set of many different masking vectors. This is essentially what the key idea of the *speckle imaging* technique is. The following subsection will give a detailed discussion about this.

3.4.2 Speckle Imaging

Speckle imaging takes a large number of short exposure images of an object, where the exposure time of each frame is short enough to "freeze" the motion and the change of the atmospheric turbulence, such that the PSF for each frame only retains information of the atmospheric turbulence at that very instant, even though it changes from image to image. This gives a short-exposure image sequence, any frame in the sequence is a "snapshot" of the object.

For any one short exposure image, classical imaging model can be applied. Here, for convenience, rewrite the model in the following

$$i(x) = o(x) * h(x) \tag{3.37}$$

where $i(x)$ is a detected image, $o(x)$ is the true object, and $h(x)$ is the PSF. In speckle imaging, $i(x)$ is one of the short exposure frames, and $h(x)$ is the PSF at this frame. This PSF varies from time to time when atmospheric turbulence exists (i.e., time varying). In other words, Eq.3.37 only expresses one $i(x)$ and $h(x)$ pair in a time sequence of short exposure images, but not the whole process.

For a single image, the Fourier transform of Eq.3.37 is $I(u) = O(u)H(u)$, where $I(u)$, $O(u)$, and $H(u)$ denote the Fourier transform of $i(x)$, $o(x)$, and $h(x)$, respectively. From the definition, we have the bispectrum $I^{(3)}(u)$ of the image $i(x)$

$$\begin{aligned} I^{(3)}(u_1, u_2) &= I(u_1)I(u_2)I^*(u_1+u_2) \\ &= O(u_1)O(u_2)O^*(u_1+u_2)H(u_1)H(u_2)H^*(u_1+u_2) \\ &= O^{(3)}(u_1,u_2)H^{(3)}(u_1,u_2) \end{aligned} \tag{3.38}$$

where $O^{(3)}(u_1, u_2)$ is the bispectrum of the object and $H^{(3)}(u_1, u_2)$ is termed the bispectrum transfer function[14]. Consider a sequence of short exposure images, and take the expectation of the bispectrum of the ensemble, we have the time averaged bispectrum as follows

$$\langle I^{(3)}(u_1,u_2)\rangle = \langle O(u_1)O(u_2)O^*(u_1+u_2)H(u_1)H(u_2)H^*(u_1+u_2)\rangle \tag{3.39}$$

.

Here the object spectrum $O(\cdot)$ is deterministic, hence can be taken outside the expectation, and this gives

$$\begin{aligned} \langle I^{(3)}(u_1,u_2)\rangle &= O(u_1)O(u_2)O^*(u_1+u_2)\langle H(u_1)H(u_2)H^*(u_1+u_2)\rangle \\ &= O^{(3)}(u_1,u_2)\langle H^{(3)}(u_1,u_2)\rangle \end{aligned} \tag{3.40}$$

Another expression of Eq.3.40 is

$$\begin{aligned} &|\langle I^{(3)}(u_1,u_2)\rangle| e^{\phi_{I^{(3)}}(u_1,u_2)} \\ &= |O(u_1)O(u_2)O^*(u_1+u_2)| e^{\phi_{O^{(3)}}(u_1,u_2)} |\langle H(u_1)H(u_2)H^*(u_1+u_2)\rangle| e^{\phi_{H^{(3)}}(u_1,u_2)} \end{aligned} \tag{3.41}$$

In the following, we will show that, in the usual condition of atmospheric turbulence, the phase of the average bispectrum $\phi_{I^{(3)}}$ is approximately **only** related to the object phase

ϕ_O. To prove this, we must prove that

$$\langle H(u_1)H(u_2)H^*(u_1+u_2)\rangle = \langle |H(u_1)||H(u_2)||H(u_1+u_2)|e^{j[\phi_H(u_1)+\phi_H(u_2)-\phi_H(u_1+u_2)]}\rangle \quad (3.42)$$

is real and non zero up to the diffraction-limit of the telescope.

3.4.3 Bispectrum Transfer Function

To prove that $\langle H(u_1)H(u_2)H^*(u_1+u_2)\rangle$ does not contribute to the phase of the averaged bispectrum, we begin with the definition of $H(u)$ of an optical instrument. The mathematical expression of $H(u)$ of a space-invariant incoherent image forming system, which is known to be the autocorrelation of the generalized pupil function, $P(\cdot)$, is given by[14]

$$H(u) = \int P(\xi^{'})P^*(\xi^{'}+\xi)d\xi^{'} \quad (3.43)$$

where ξ denotes the coordinate in the telescope pupil, it is related to the spatial frequency by $\xi = \lambda f u$. λ is the wave length and f is the distance from the pupil plane to the image plane. Eq.3.43 is then expressed as

$$\begin{aligned} H(u) &= \int P(\lambda f u')P^*(\lambda f u' + \lambda f u) f\lambda du' \\ &= \int P(u')P^*(u'+u)du' \end{aligned} \quad (3.44)$$

Since the light of an object propagates through the atmosphere before it reaches to the pupil, the pupil function $P(u)$ may be split into a product of two functions: $P(u) = P_0(u)A(u)$, where $P_0(u)$ represents the pupil function, and $A(u)$ represents the effect of the random turbulence and can be assumed to be a time stationary random variable[14, 29].

Note that $A(u)$ will be different for different isoplanatic patches. In this context, we assume the real and the imaginary parts of $A(u)$ are zero-mean Gaussian distributed, such that we have

$$\begin{aligned}\langle H^{(3)}(u_1,u_2)\rangle &= \langle H(u_1)H(u_2)H(-u_1-u_2)\rangle \\ &= \int\int\int P_0(u_1')P_0(u_1'+u_1)P_0(u_2')P_0(u_2'+u_2)P_0(w)P_0(w-u_1-u_2) \\ &\langle A(u_1')A(u_1'+u_1)A(u_2')A(u_2'+u_2)A(w)A(w-u_1-u_2)\rangle du_1'du_2'dw\end{aligned} \tag{3.45}$$

where $w = (-u_1 - u_2)'$. This is the sixth-order moment. To calculate Eq.3.45, the assumption of $A(u)$ (i.e., the real and the imaginary parts of $A(u)$ are zero-mean Gaussian distributed) is used and remove items with zero value, then we have

$$\begin{aligned}\langle A_1A_2A_3A_4A_5A_6\rangle = \quad & \langle A_1A_2\rangle\langle A_3A_4A_5A_6\rangle + \\ & \langle A_1A_2A_3A_4\rangle\langle A_5A_6\rangle + \\ & \langle A_1A_2A_5A_6\rangle\langle A_3A_4\rangle - \\ & 2\langle A_1A_2\rangle\langle A_3A_4\rangle\langle A_5A_6\rangle + \\ & \langle A_1A_4\rangle\langle A_3A_6\rangle\langle A_5A_2\rangle + \\ & \langle A_1A_6\rangle\langle A_3A_2\rangle\langle A_5A_4\rangle,\end{aligned} \tag{3.46}$$

where

$$\begin{aligned}A_1 &= A(u_1') \\ A_2 &= A(u_1'+u_1) \\ A_3 &= A(u_2') \\ A_4 &= A(u_2'+u_2) \\ A_5 &= A(w) \\ A_6 &= A(w-u_1-u_2)\end{aligned} \tag{3.47}$$

Since $A(u)$ is assumed to be a stationary random variable, its autocorrelation $C_A(u)$ may be defined as $C_A(u) = \langle A(u')A^*(u'+u)\rangle$. In practice, for usual seeing conditions, $A(u)$ is very fine structured compared to the pupil function, and can be considered as a δ

function[29]:

$$C_A(u) = K \cdot \delta(u), \tag{3.48}$$

where K is a constant.

Substitute Eq.3.46 and Eq.3.48 into Eq.3.45, we have

$$\begin{aligned}\langle H^{(3)}(u_1, u_2)\rangle \quad &= \langle H(u_1)\rangle\langle H(u_2)H(-u_1-u_2)\rangle + \\ &\langle H(u_1)H(u_2)\rangle\langle H(-u_1-u_2)\rangle + \\ &\langle H(u_2)\rangle\langle H(u_1)H(-u_1-u_2)\rangle - \\ &2\langle H(u_1)\rangle\langle H(u_2)\rangle\langle H(-u_1-u_2)\rangle + \\ &K \cdot T(u_1, u_2)\end{aligned} \tag{3.49}$$

where $T(u_1, u_2)$ is associated with the modulus squares of the pupil function

$$T(u_1, u_2) = \int |P_0(w)|^2 |P_0(w+u_1+u_2)|^2 [|P_0(w+u_1)|^2 + |P_0(w+u_2)|^2]^2 dw \tag{3.50}$$

From Eq.3.50, one would note that $T(u_1, u_2)$ is real and nonzero for all frequency components up to the diffraction limit of the telescope.

The other four terms in Eq.3.49 are also real. This can be proved in the same way as calculating Eq.3.45 and by using a fourth-order moment. Finally, Eq.3.49 can be expressed only in terms of $|P_0(u)|^2$, and has zero phase.

Thus far, we have proved that the phase of the averaged bispectrum of the short exposure images, $\phi_{I^{(3)}}(u_1, u_2)$ is only related to the phase of the object image, ϕ_O, with relation:

$$\phi_{I^{(3)}}(u_1, u_2) = \phi_O(u_1) + \phi_O(u_2) - \phi_O(u_1 + u_2) \tag{3.51}$$

Note that the above discussion is based on astronomical imaging, where the observation angle is isoplanatic (for the definition of isoplanatic, please refer to Chapter 4.2). In wide-area imaging, the result is likely to be anisoplanatic. In this case, $A(u)$ may be the composite of several components each of which is the different turbulence in each isoplanatic patch. Each component of $A(u)$ would also disappear from Eqs.3.46-3.49. But each component is not statistically independent from each other so we need to break one image into isoplanatic regions.

3.4.4 Compensation of the Additive Noise

Additive noise in a true image can be compensated by the averaged bispectrum of the image stream if the noise is signal-independent and zero-mean. Note that it is not necessary for it to be Gaussian. In fact, most real signals contain non-Gaussian additive noise.

Suppose the detected image is

$$i(x) = o(x) + n(x) \tag{3.52}$$

where $o(x)$ is the true image, and $n(x)$ is a signal-independent and zero-mean noise.

To verify this, we put down the ensemble averaged triple correlation of $i(x)$

$$\begin{aligned} \langle i^{(3)}(x,x')\rangle \quad &= o^{(3)}(x,x')+ \\ &\langle n^3(x,x')\rangle+ \\ &\langle n(x)\rangle[o^2(x)+i^2(x')+o^2(x'-x)]+ \\ &[\int o(x)dx][n^2(x)+n^2(x')+n^2(x'-x)] \end{aligned} \tag{3.53}$$

where

$$\begin{aligned} o^2(x) &= \int o(x)o(x+x')dx' \\ n^2(x) &= \langle n(x)n(x+x')\rangle \end{aligned} \tag{3.54}$$

The second to fourth terms in Eq.3.53 are undesired, and they will vanish if the noise has zero mean. The ensemble averaged triple correlation of the noise contaminated signal therefore is theoretically shown to be identical to the triple correlation of the true signal, successfully compensating the signal-independent and zero-mean noise.

3.5 Image Reconstruction Using Bispectrum

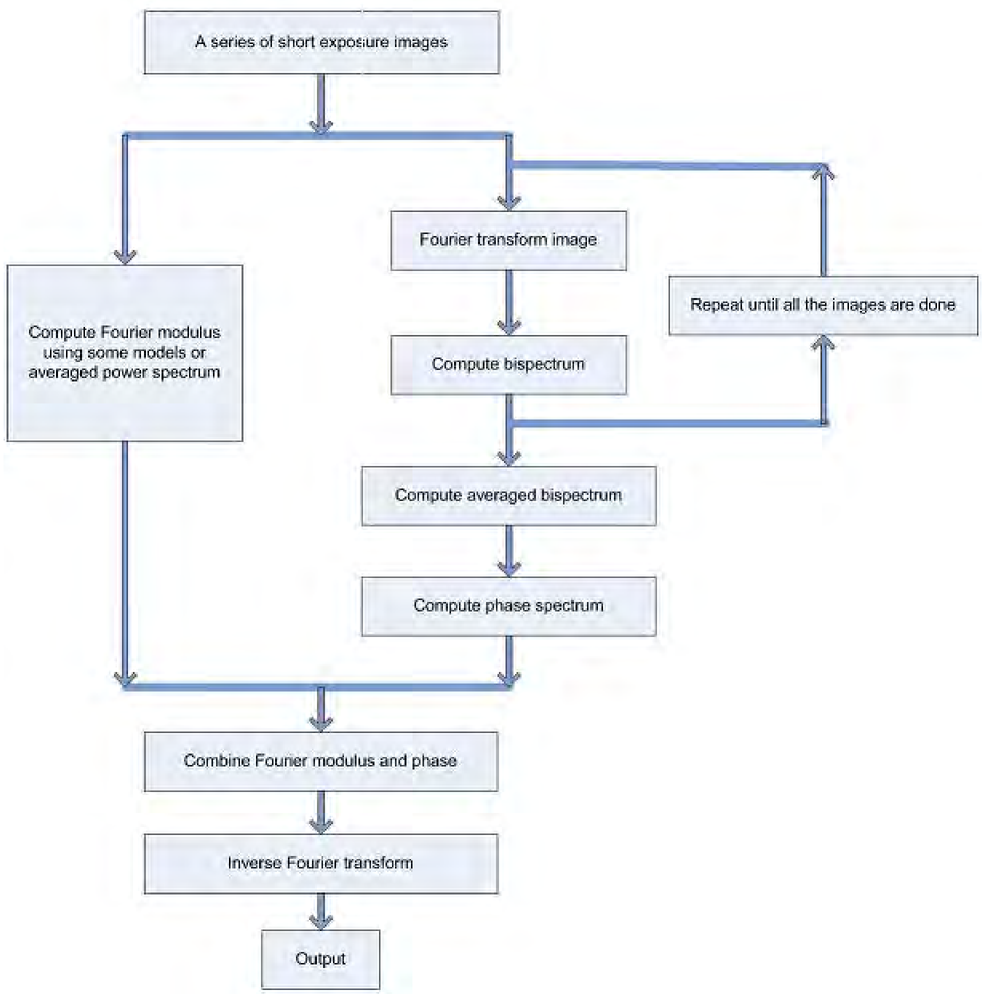

Figure 3.3: Block diagram for image reconstruction from the bispectrum.

Using the bispectrum technique, image reconstruction for images taken through atmospheric turbulence will make use of the Fourier transform. Fig.3.3 is a simple illustration of the process. Input a sequence of short exposure images, compute the Fourier phase and modulus of the potential image, and then output a single diffraction limited estimation of the object. This section will exploit how to estimate the Fourier phase of the object from Eq.3.51.

3.5.1 Recursive Phase Calculation

For simplicity, our discussion below assumes one-dimensional signal only. This discussion, however, can be easily extended to two-dimensional image signals.

Moreover, we only discuss the case of $\phi_{O(u)}$ when $(u > 0)$. This is because, for a real signal (say, $o(x)$), its Fourier transform is Hermitian, i.e., $O(u) = O^*(-u)$, hence we have $\phi_O(u) = -\phi_O(-u)$.

Here, rewrite Eq.3.51 as

$$\phi_O(u_1 + u_2) = \phi_O(u_1) + \phi_O(u_2) - \phi_{I^{(3)}}(u_1, u_2) \tag{3.55}$$

$\phi_O(u)(u \geq 2)$ will be computed recursively based on Eq.3.55, if $\phi_O(0)$ and $\phi_O(1)$ are known. Because $\phi_O(0)$ and $\phi_O(1)$ only affect the restored signal by spatial shift, it can be arbitrarily set to nil. In this context, we set values at frequencies 0 and 1 identical to the phase of the temporally averaged image of the image frame stream.

Table 3.1 illustrates one recursive method for phase computation[40]. Note that every ϕ_O has several different independent representations, the number of which increases as the frequency increases. All these representations contribute to the estimation of the phase at a common frequency. Averaging the different results helps to suppress the noise by improving the SNR (signal-to-noise ratio) of the recovered signals[40].

Actually, there are many different options to compute and average the Fourier phase ϕ based on Eq.(3.55). Fig.3.4 shows three possible paths (Remember that the bispectrum of a one-dimensional signal is two-dimensional). The computing area is limited to one 1/12 slice (for one-dimensional signal) due to the symmetry property.

The way presented in Tab.3.1 favors the path in Fig.3.4 (a). A simplier explanation is described in Tab.3.2. A few of different unions in $\langle u_1, u_2 \rangle$ determine the value of ϕ_O at specified frequency, for example, $\phi_O(4)$, two pairs (i.e., $\langle u_1, u_2 \rangle = \langle 2, 2 \rangle, \langle 3, 1 \rangle$) both contribute to its estimation. The estimated $\phi_O(4)$ is then used to compute ϕ_O at higher spatial frequencies.

Using this path, two options exist for computing the average value of the Fourier phase. One is to calculate all the independent representations based on some specific values of phases at lower frequencies, and then take the average as the final output of the phase. The other is: in one recursive step, average all the calculated representations first, and then use the averaged value to compute the phases at higher frequencies. This method applies in the entire recursion process. The advantage is that the averaging suppresses noise at each step, therefore minimizing the influence of noise and enhancing the accuracy of the estimate of the phases[45].

Another potential path, Fig.3.4 (b), is shown in Tab.3.3.

In this case, all estimates of all phase values are computed first (Note that no averaging in the course of recursion). These initial values are then used for further calculation in the following recursive steps. Subsequently take the average to obtain the Fourier phase.

The third path uses all the bispectrum components, as exhibited in Fig.3.4 (c). The advantage is that all the independent phase estimates and the influence of the noise at each point can be taken into account, so that some weighted factors may be applied to obtain a more accurate average. This is at the cost of computation because the recursion covers all

Table 3.1: Recursive method of phase calculation from bispectrum

$\langle u_1, u_2 \rangle$	$\phi_O(u_1+u_2) = \phi_O(u_1) + \phi_O(u_2) - \phi_{I^{(3)}}(u_1,u_2)$	$\phi_O(\cdot)$
$\langle 1,0 \rangle$	$\phi_O(1) = \phi_O(1) + \phi_O(0) - \phi_{I^{(3)}}(1,0)$	$\backslash$
$\langle 1,1 \rangle$	$\phi_O(2) = \phi_O(1) + \phi_O(1) - \phi_{I^{(3)}}(1,1)$	$\phi_O(2)$
$\langle 2,0 \rangle$	$\phi_O(2) = \phi_O(2) + \phi_O(0) - \phi_{I^{(3)}}(2,0)$	$\backslash$
$\langle 2,1 \rangle$	$\phi_O(3) = \phi_O(2) + \phi_O(1) - \phi_{I^{(3)}}(2,1)$	$\phi_O(3)$
$\langle 2,2 \rangle$	$\phi_O(4) = \phi_O(2) + \phi_O(2) - \phi_{I^{(3)}}(2,2)$	$\phi_O(4)$
$\langle 3,0 \rangle$	$\phi_O(3) = \phi_O(3) + \phi_O(0) - \phi_{I^{(3)}}(3,0)$	$\backslash$
$\langle 3,1 \rangle$	$\phi_O(4) = \phi_O(3) + \phi_O(1) - \phi_{I^{(3)}}(3,1)$	$\phi_O(4)$
$\langle 3,2 \rangle$	$\phi_O(5) = \phi_O(3) + \phi_O(2) - \phi_{I^{(3)}}(3,2)$	$\phi_O(5)$
$\langle 3,3 \rangle$	$\phi_O(6) = \phi_O(3) + \phi_O(3) - \phi_{I^{(3)}}(3,3)$	$\phi_O(6)$
$\langle 4,0 \rangle$	$\phi_O(4) = \phi_O(4) + \phi_O(0) - \phi_{I^{(3)}}(4,0)$	$\backslash$
$\langle 4,1 \rangle$	$\phi_O(5) = \phi_O(4) + \phi_O(1) - \phi_{I^{(3)}}(4,1)$	$\phi_O(5)$
$\langle 4,2 \rangle$	$\phi_O(6) = \phi_O(4) + \phi_O(2) - \phi_{I^{(3)}}(4,2)$	$\phi_O(6)$
$\vdots$	$\vdots$	$\vdots$
$\vdots$	$\vdots$	$\vdots$
$\langle n,0 \rangle$	$\phi_O(n) = \phi_O(n) + \phi_O(0) - \phi_{I^{(3)}}(n,0)$	$\backslash$
$\langle n,1 \rangle$	$\phi_O(n+1) = \phi_O(n) + \phi_O(1) - \phi_{I^{(3)}}(n,1)$	$\phi_O(n+1)$
$\langle n,2 \rangle$	$\phi_O(n+2) = \phi_O(n) + \phi_O(2) - \phi_{I^{(3)}}(n,2)$	$\phi_O(n+2)$
$\vdots$	$\vdots$	$\vdots$
$\langle n,n \rangle$	$\phi_O(n+n) = \phi_O(n) + \phi_O(n) - \phi_{I^{(3)}}(n,n)$	$\phi_O(2n)$
$\vdots$	$\vdots$	$\vdots$

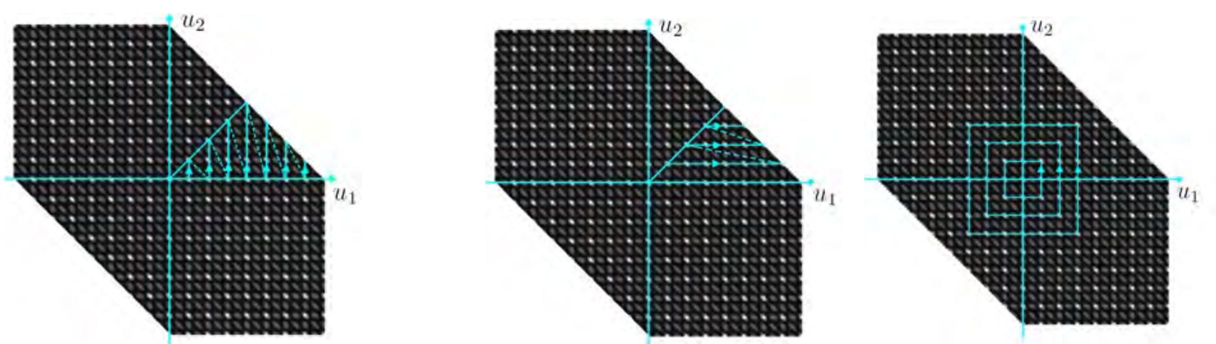

(a) (b) (c)

Figure 3.4: Different potential paths of computing the Fourier phase.

Table 3.2: Illustration of the first path

$\langle u_1, u_2 \rangle$	$\langle 1,1 \rangle$	$\langle 2,1 \rangle$	$\langle 2,2 \rangle$	$\langle 3,1 \rangle$	$\langle 3,2 \rangle$	$\langle 3,3 \rangle$	$\langle 4,1 \rangle$	$\langle 4,2 \rangle$	$\cdots$
$\phi_O(\cdot)$	$\phi_O(2)$	$\phi_O(3)$	$\phi_O(4)$	$\phi_O(4)$	$\phi_O(5)$	$\phi_O(6)$	$\phi_O(5)$	$\phi_O(6)$	$\cdots$

Table 3.3: Illustration of the second path

$\langle u_1, u_2 \rangle$	$\langle 1,1 \rangle$	$\langle 2,1 \rangle$	$\langle 3,1 \rangle$	$\cdots$	$\langle n-1,1 \rangle$	$\langle 2,2 \rangle$	$\langle 3,2 \rangle$	$\cdots$
$\phi_O(\cdot)$	$\phi_O(2)$	$\phi_O(3)$	$\phi_O(4)$	$\cdots$	$\phi_O(n)$	$\phi_O(4)$	$\phi_O(5)$	$\cdots$

the redundant slices, so needs a larger data set or a complex algorithm. In this thesis, the third method is employed.

3.5.2 Least-Squares Phase Recovery

Usually, a recursive method has recovered all the object phases. However, the error in the bispectral phase at low frequencies affects the phase estimation at high frequencies. This is because the phase at high frequency is a cumulated sum of the preceding bispectral phases, the higher the frequency, the larger the possible error [43, 47].

To avoid the error accumulation, a least-squares method can be used. Rewriting Eq.3.51, and for convenience, denote $\phi_{I^{(3)}}$ as $\beta_{I^{(3)}}$

$$\beta_{I^{(3)}}(u_1, u_2) = \phi_O(u_1) + \phi_O(u_2) - \phi_O(u_1 + u_2) \tag{3.56}$$

in matrix form as

$$\mathbf{A}\Phi = \beta, \tag{3.57}$$

where Φ is the vector of the Fourier phase of the object,

$$\Phi = (\phi_1, \phi_2, \cdots, \phi_N)^T \tag{3.58}$$

with T denoting the transpose operation and N being the total number of object phases. β is the vector of the averaged bispectrum phases. In accordance with the properties of the bispectrum and the frequency range, and to avoid redundancy, β is restricted to

$$\beta = (\beta_{1,1}, \beta_{1,2}, \cdots, \beta_{1,N-1}, \beta_{2,1}, \beta_{2,2}, \cdots, \beta_{2,N-2}, \cdots, \beta_{N/2,N/2})^T \tag{3.59}$$

$\mathbf{A}$ is a sparse matrix with $\frac{N^2}{4} \times N$ components. As each bispectral phase at (u_1, u_2) is built up of three object phases at u_1,u_2,and $(u_1 + u_2)$, matrix $\mathbf{A}$ contains only three nonzero elements in each row.

$$\mathbf{A} = \begin{bmatrix} 2 & -1 & & & & \\ 1 & 1 & -1 & & & \\ \vdots & \vdots & \vdots & & & \\ \vdots & \vdots & \vdots & \vdots & & \\ \cdots & \cdots & \cdots & 2 & \cdots & -1 \end{bmatrix}$$

The classical weighted-least-squares solution to Eq.3.57 is the unique vector among all vectors that minimizes the cost function[45, 43, 50, 46]:

$$E = (\beta - \mathbf{A}\Phi)^T \mathbf{W} (\beta - \mathbf{A}\Phi), \tag{3.60}$$

where $\mathbf{W}$ is an $\frac{N^2}{4} \times \frac{N^2}{4}$ diagonal weighted matrix. The minimum can be found by differentiating the above function and setting it to zero. The initial estimate of the object phase can be zero or any random value, but a more correct estimate such as results from recursive method may speed the convergence.

3.5.3 Phase Ambiguity

Solving Eq.3.60 will introduce 2π ambiguities (or phase wrapping) to the object phase. The bispectrum phases are known only up to a modulo of 2π; when multiple estimates of a single object phase are used, the bispectrum phases will not be equal to their principal arguments [45]. As a result, several local minima can occur before a global minimum is found.

Fortunately, by the recursive method such 2π ambiguities can be easily avoided. Instead of directly summing up all the different values of ϕ and then taking the average as the recovered phase value, the exponential factors $e^{i\phi}$ should be computed, summed and averaged, followed by computing the angle of the average exponent to obtain principal phases. In this case, the exponent of a phase is a phasor, and the method is called the phasor approach[104].

To avoid phase ambiguity in solving Eq.3.57, three methods including the *phasor* technique are proposed in the literature. A brief review of them is in order.

1. **Adding multiples of** $\pm\pi$: This method uses bispectrum phases to calculate phase unwrapping, but adds multiples of 2π to the principal bispectrum phase[46, 105, 106]. Let $\beta_{\mathbf{0}}$ be the modulo 2π bispectrum phase vector, k be an integer vector that unwraps the bispectrum phase, then β is

$$\beta = \beta_{\mathbf{0}} + k2\pi, \tag{3.61}$$

and Eq.3.57 is written as

$$\mathbf{A}\Phi = \beta_{\mathbf{0}} + k2\pi, \tag{3.62}$$

To calculate an unwrapping vector k, suppose that a full rank matrix $\mathbf{c}$ exists, which satisfies

$$\mathbf{cA} = 0, \tag{3.63}$$

Combining Eq.3.62 and 3.63, we have

$$\mathbf{c}k = -\mathbf{c}\beta_{\mathbf{0}}/2\pi, \tag{3.64}$$

such that, the object phase can be solved using k which satisfies the above equation. The disadvantage of this approach is that k computed from the noisy bispectrum may be incorrect, the solution calculated by the least-squares method then may not be necessarily optimal.

2. **The phasor method**: This method takes the exponent on both sides of Eq.3.56 and solves for the optimal value by minimizing the error between the two phasors[104, 48, 49]:

$$e^{j\beta_{I^{(3)}}(u_1,u_2)} = e^{j(\phi_O(u_1)+\phi_O(u_2)-\phi_O(u_1+u_2))}, \tag{3.65}$$

The weighted least squares solution to the above equation is given by

$$\Phi = (\mathbf{A}^T\mathbf{W}\mathbf{A})^{-1}\mathbf{A}^T\mathbf{W}\beta \tag{3.66}$$

Solving Eq.3.66, a final solution can be found following [45]

$$\begin{aligned} e^{j\phi(v)} = \textstyle\sum_{u\neq v} \mathbf{W}(u,v)[\frac{B(u,v)}{O(u)O^*(u+v)}] + 4\sum_{u=v} \mathbf{W}(u,v)[\frac{B(u,v)}{O^*(u+v)}]^{1/2} + \\ \textstyle\sum \mathbf{W}(u,v-u)[\frac{B(u,v-u)}{O(u)O(v-u)}]^*, \end{aligned} \tag{3.67}$$

where $\mathbf{W}$ is given by,

$$\mathbf{W}(u,v) = \{ \begin{array}{cc} SNR[B(u)]^2 & u = v \\ 0 & u \neq v \end{array} \tag{3.68}$$

where $SNR[B(u)]$ is the estimate of the bispectrum phasor divided by the standard deviation of the estimate. **W** can also be calculated by taking the square of the modulus of the bispectrum over the variance of the modulus, which is exactly the method proposed by Meng et.al.[41].

3. **Direct modulo** 2π: An alternative is to take Eq.3.60 modulo 2π, the cost function is then expressed as [49]

$$E = (mod_{2\pi})[(\beta - \mathbf{A}\Phi)^T]\mathbf{W}(mod_{2\pi})[(\beta - \mathbf{A}\Phi)], \tag{3.69}$$

the weighting function **W** is now redefined as the reciprocal of the variance of the bispectrum phase.

For interested readers, other existing approaches to unwrapping the modulo 2π bispectrum phases can be found in [45, 41].

In this thesis, we mainly implement and study the performances of the recursive method and the weighted-least-squares method. For both algorithms, the phasor method is adopted to solve the phase problem. The final solution found is very similar to Matson's [45], which is shown in Eq.3.67.

3.5.4 Storage and Computational Complexity

To actually compute a bispectrum of a two-dimensional image of reasonable size on a typical desktop PC may prove to be a practically challenging task.

This is because, for a straightforward implementation of the computation of the bispectrum (based on its definition), the required storage and computational complexity is often higher than the capacity of a typical desktop PC. To show this , let us just give a simple example. For a rather small and monochromatic image of 256×256 pixels, its bispectrum will contain $2^{32} \approx 4G$ complex values, each complex value for example contains 8 bytes. As a result, the bispectrum of an image with size of 256×256 pixels needs 32G bytes for data storage, and for computational efficiency sake, this has better to be the main memory (as opposed to hard-disk) of the PC. Remembering further that, all our computations must be repeated for every frame of the input short exposure sequence, which may possibly contain over one thousand frames.

To overcome these difficulties and improve the speed of a practical turbulence-removal image reconstruction system, we propose to take advantage of the following factors.

First of all, the symmetry property of bispectrum will help save much data storage. As we discussed before, the bispectrum has only 1/12 non-redundancy. Therefore, one only needs to compute one twelfth of the entire spectrum. This storage space may be acceptable for current (very) high-end personal computers.

Secondly, partitioning the image into a number of (overlapping) subregions may improve the condition without much harming the bispectrum and the reconstruction processing. Instead of performing on the orignal full image, the restoration is applied to each subregions separately: compute the bispectrum of each subregion, and perform phase recovery of the subregion using the calculated bispectrum. When all the segmented parts of an image are estimated, put them together (in some systematic way, as we shall see later) to fuse a single, restored estimate of the true image.

Segmentation in this way effectively avoids the difficulties with the storage capability and successfully speeds up the computations. Suppose an image with size of 256×256 pixels is broken into subregions of size of 64×64 pixels, each partial bispectrum contains only $2^{24} \approx 16M$ complex values, and needs 128MB for data storage (again, each complex value containing 8 Bytes). This modest memory requirements are easily available in current computers.

Moreover, in the case of wide field of view imaging, the isoplanatic angle may be much smaller than the field of view, so that the subdivision increases the possibility that the distortion in an image region is uniform or isoplanatic (this will be discussed further in Chapter 4), therefore significantly improving the reconstructed image quality. To cover all the isoplanatic regions and recover a better estimate, the original images are broken into regions with 50% overlapping (both horizontal and vertical). This process is illustrated in Fig.3.5.

Fig.3.6 shows how an image is divided into smaller tiles. The image is broken into 4 regions, each region contains four blocks, i.e, $< 1, 2, 4, 5 >$, $< 2, 3, 5, 6 >$, $< 4, 5, 7, 8 >$, and $< 5, 6, 8, 9 >$. Some blocks are overlapped, for example, block $< 2 >$ and $< 5 >$ are shared by the red and green region, and block $< 4 >$ and $< 5 >$ are both in the red and purple tiles.

To overcome the artifacts from overlapping and adding of the regions, a two-dimensional *Hanning* window is used, which is shown in Fig.3.7. The four quarter slices of the two-dimensional Hanning window add to one.

This method was implemented in MATLAB without code optimization. We tested it on a PC of $3.20GHz$ with $1GB$ of RAM. The computation time is about 150 minutes for a sequence containing 100 frames of image sized at 256×256, and the processes were on subregions of 64×64 pixels each.

3.6 Experiments

One of the premises of employing the bispectrum is that it suppresses additive zero mean noise. In our experiment, we first test this first property using a simulated one-dimensional

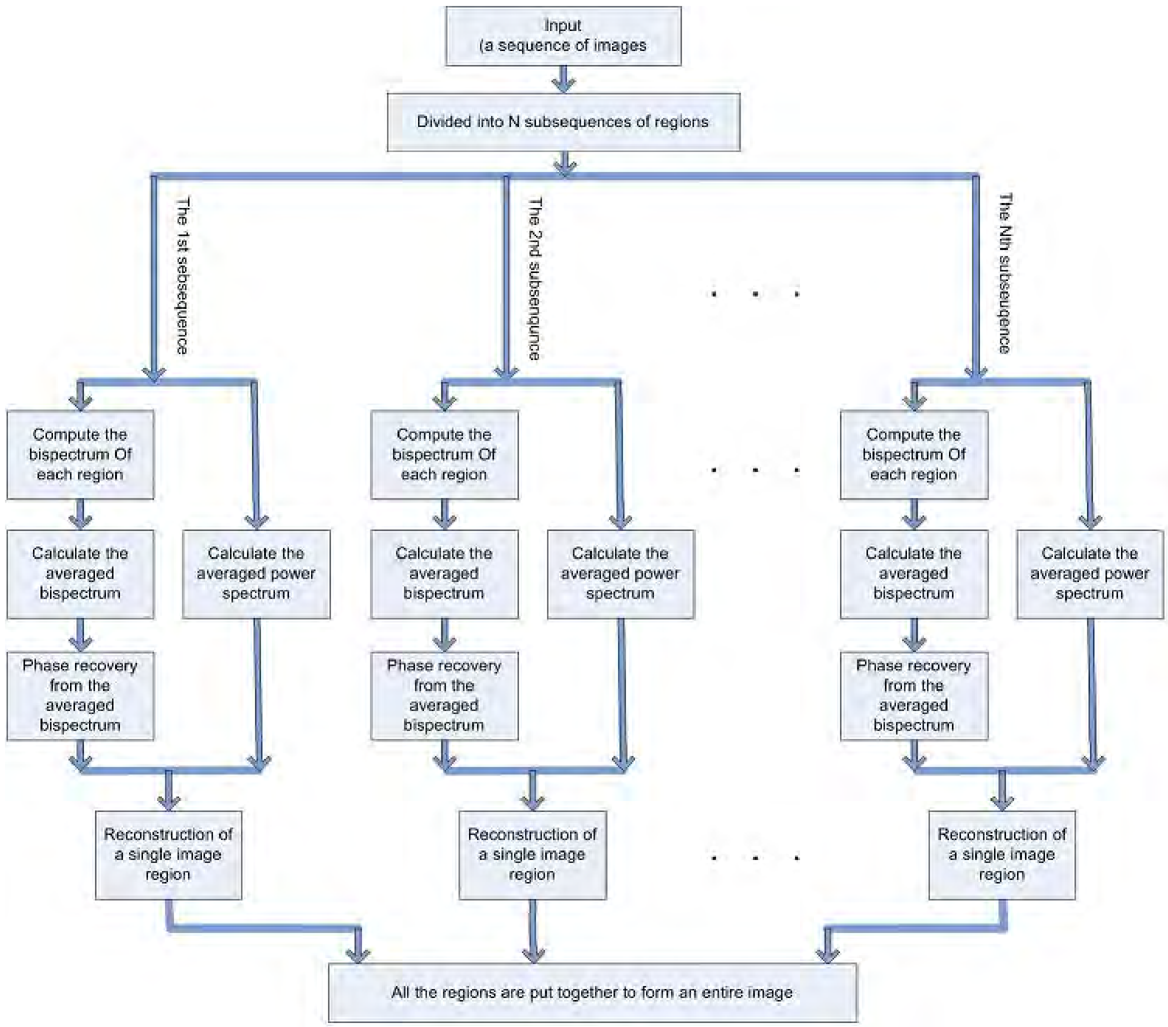

Figure 3.5: The original series of short exposure images are broken into N series of subregions, each data set is used to estimate the phase domain of a particular image tile using bispectrum. The phase spectrum of the entire image estimate is produced by stitching each phase estimate to its correct position.

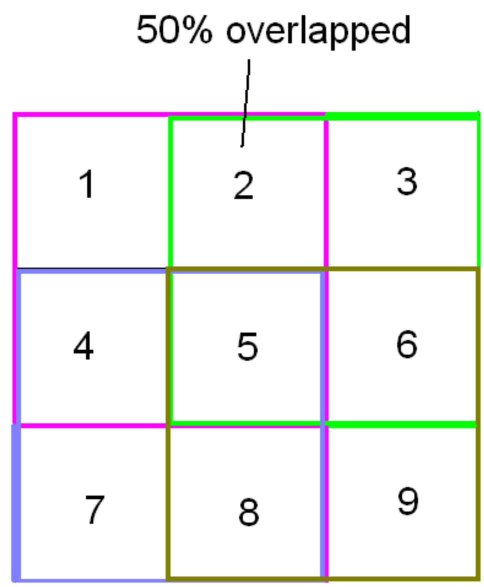

Figure 3.6: Simple illustration of the segmentation of an image, regions are 50% overlapped in both horizontal and vertical directions.

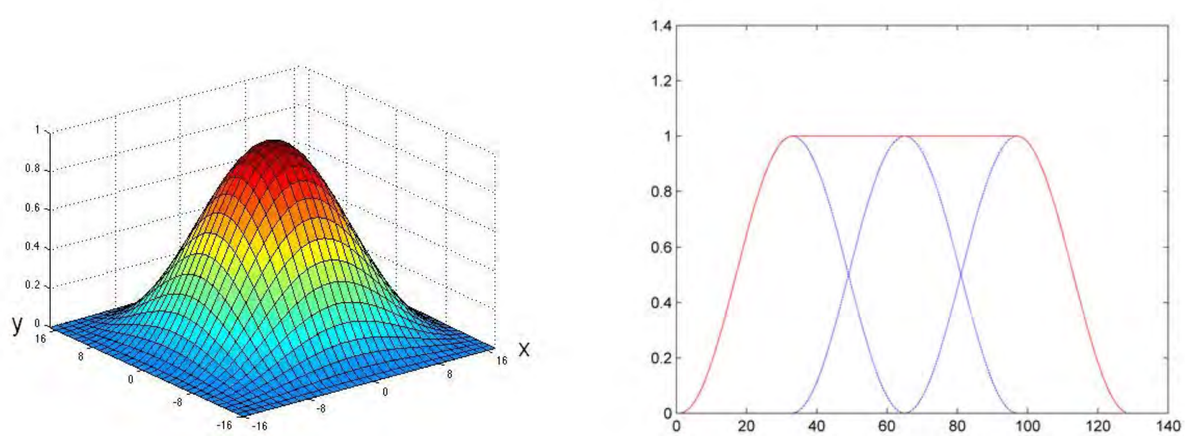

(a) The 2-D hanning window (b) Lineout through the window.

Figure 3.7: The 2-D Hanning window: The four quarter slices add to one, which ensures the combined image is smooth and has no artifacts.

signal with 50 observations. Its length is 256 with values set the following ranges as: $[32:36]=4$, $[80:90]=7$, $[140:150]=10$, zero otherwise, and contaminated with zero-mean Gaussian noise of variance being 1. Fig.3.8 shows the true signal in (a), contaminated observations in (b) and the results by the bispectrum technique using different amount of observations, i.e., 10 frames in (c) and 50 frames in (e). For the sake of comparison, we provide the results by averaging the same observations, i.e., 10 frames in Fig.3.8 (d) and 50 frames in Fig.3.8 (f).

This experiment shows the ability of the bispectrum in removing the additive noise. One would notice that the additive noise is almost compensated for by the average of the bispectrum, even with a small amount of observations (e.g., 10 frames). As expected, the average of the ensemble of the observation (i.e., 50 frames) obtains the best result. This is because the additive noise is zero mean, the simple average of the additive noise on a particular point reaches to zero when the number of observation is large enough. However, this simple average operation cannot produce reasonable results while applied in practice for the reason that real world data suffers more complex degradation beyond the additive noise. This drawback of simple averaging is remedied by the other properties of the bispectrum as we discussed in previous sections, even though a residual of the additive noise exists.

The three-dimensional shape of the triple correlation of the clean and the average triple correlation of 50 observations are also given in Fig.3.9. Both shapes are very similar, which implies that both contain very similar phase information of a signal. Such ensures that the phase of an signal can be estimated correctly. The magnitude of the signal is also computed based on its bispectrum. But, in general, researchers prefer to use the average power spectrum of the observations for its simple computation and reasonable results.

The second experiment is carried out using real world data. The data is obtained with a portable 0.14 m dia f14 Cassegrain telescope and progressive scan CCD camera. A test

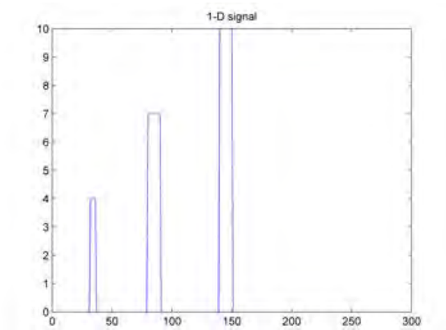

(a) The original signal

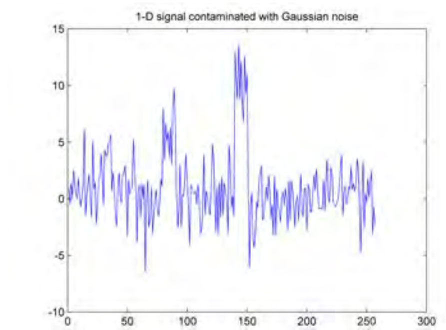

(b) The contaminated signal

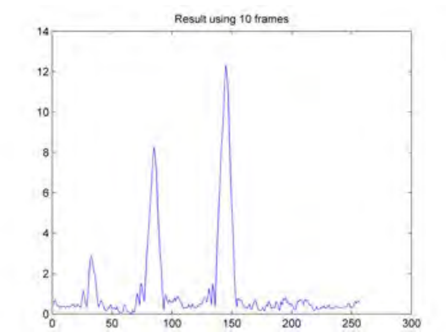

(c) Result using the bispectrum

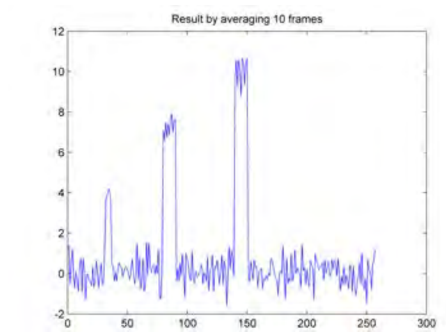

(d) The average of 10 frames

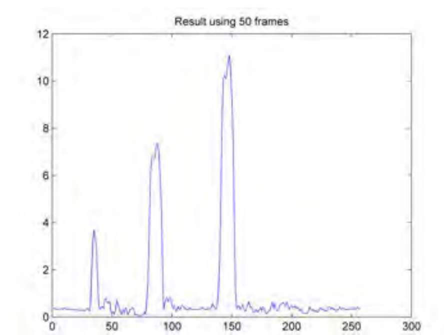

(e) Result using the bispectrum

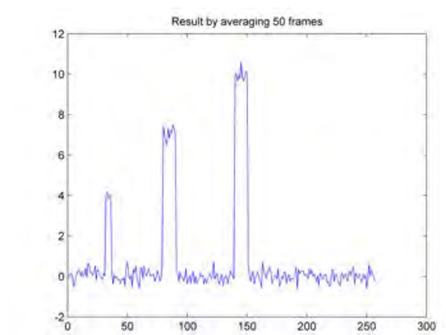

(f) The average of 50 frames

Figure 3.8: Experiment of simulated data. Results show that the additive noise can be suppressed by averaging the bispectrum of the detected data set.

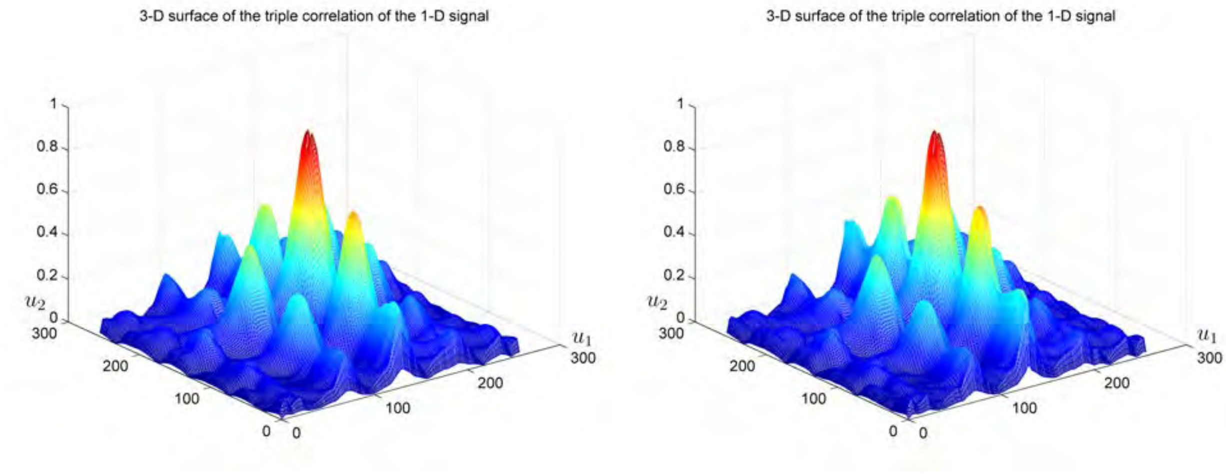

(a) (b)

Figure 3.9: The three-dimensional surface of the triple correlation of one-dimensional signal. (a) The value of the original signal in Fig.3.8 (a); (b) The averaged value of the triple correlation of 100 zero-mean Gaussian noise contaminated detections.

scene (hill and house) to be observed is 10km distant and the exposure time is on order of 5ms. The number of image frames is 75. The image size is 512×512 pixels.

The result is obtained by performing calculation on smaller image blocks. This is because that the data storage of the four-dimensional bispectrum is very demanding and is out of the ability of current available personal computers. The image is divided into several regions small enough to favour the computation ability of a personal computer, estimates of different regions are then put together to form the result. In this context, we ignore the anisoplanatism and isoplanatism in each region and its size is designed to be 32×32 pixels.

Fig.3.10 (a) and (b) show two samples of the short exposure images taken through atmospheric turbulence. One can see that the edges of the house and the windows warp nonuniformly in different regions and that the distortion is different from one image to one image. Fig.3.10(c) is the result produced by recursive bispectrum phase recovery method using 75 frames. The images are divided into subregions with 50% overlap, and the size of

(a) One sample of input.

(b) Another sample of input.

(c) Result by bispectrum using 75 frames.

(d) Temporal average of 75 frames.

Figure 3.10: Experiment with real data. The data is obtained with a portable 0.14 m dia f14 Cassegrain telescope and progressive scan CCD camera. A test scene (hill and house) to be observed is 10km distant and the exposure time is on order of 5ms. The number of image frames is 75. The result image is comprised by the estimates of smaller regions in the entire image due to the difficulty of locating large memory needs and data storage of the bispectrum of the entire image.

subregion is 32×32 pixels. It gives a more geometrically correct estimate than the result by temporally averaging the ensemble images. Note that the edges of the house are in correct position and are sharper than in Fig.3.10(d), and more detail in the scene is visible.

Fig.3.11 provides two results produced by 32×32 pixels and 64×64 pixels subregions, respectively. This experiment verifies that the performance and speed of the algorithm is associated with segmentation of the original images. In this case, the computer we use is $3.20GHz$ and $1GB$ of RAM, about 50 minutes are needed for the process with region size being 32×32 pixels, and 120 minutes for 64×64 pixels.

Moreover, the image quality of the reconstructed result depends on the segmentation size, to some degree. In fact, when choosing the region size, two factors should be considered: the effect of isoplanatic angle, and PSF extent[2]. If the size of each subregion is well chosen so that each region is within the isoplanatic angle, the effect of the turbulence is uniform across the subregion, i.e. the PSF is position independent. Thus, the bispectrum is operated in an isoplanatic region, and produce better result. Further, as the turbulence does not lie outside the isoplanatic angle, the information of the turbulence retained in the subregion and its bispectrum can be fully exploited.

If the region size is too small, the region is clipping the PSF, so that only partial information captured is used for image restoration, the result will be worse than the case that the region size fits the isoplanatic angle well. In other case, when the region size is too large, the region suffers from anisoplanatism which leads to a spatially variant PSF, rendering a worse result.

Fig.3.11 better illustrates this. Fig.3.11 (a) has sharper edges, which indicates that the region is within the isoplanatic patch. However, the region size may have been chosen to be a little too small. As a result, the information of the PSF in an isoplanatic patch is not fully used, which causes the vertical pillar is not as straight as the result in Fig.3.11 (b).

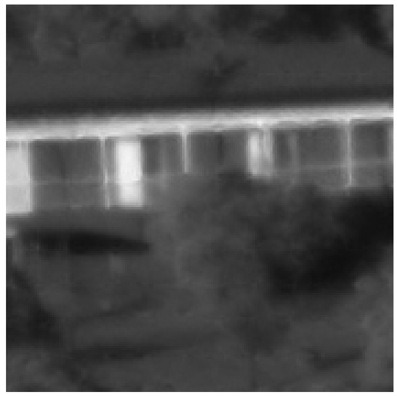

(a) Region size is 32×32. Computation time is 50 minutes.

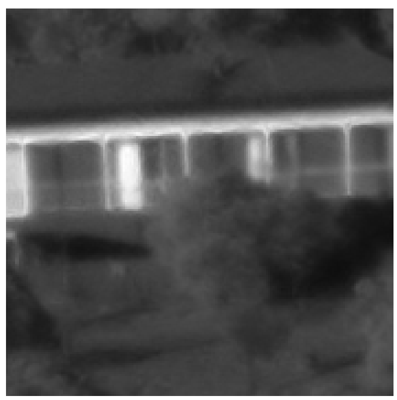

(b) Region size is 64×64. Computation time is 120 minutes.

Figure 3.11: Comparison of results produced by regions of different sizes. The number of image frames is 75, and the processing image size is 256×256. The computation time used in (a) is much smaller than that used in (b).

3.7 Summary

This chapter has analysed the definition and properties of the Fourier pair of bispectrum and triple correlation. The feasibility of applying averaged bispectrum to overcome the effect of atmospheric turbulence on an imaging system was theoretically discussed, and empirically validated.

It also provides methods for phase recovery by solving the averaged bispectrum of the data set. Moreover, the 2π problem and the storage and computation problem are discussed in detail, and solutions are discussed.

Finally, experiments have been carried out using one-dimensional simulated data and two-dimensional real image data. The former experiment shows that bispectrum has the ability of removing the additive noise of a signal, the latter demonstrates that phase spectrum can be well reconstructed by the averaged bispectrum of the observations.

Chapter 4

Lucky Region and Bicoherence

4.1 Introduction

In speckle imaging, there is some possibility, in a sequence of short exposure images, that one particular image called a lucky image will approach diffraction-limited resolution at the moment that the instantaneous effect of atmospheric turbulence is negligible. As the probability of obtaining a lucky image is low in practical application, an alternative is proposed to find smaller well resolved image patches instead of the entire image. We name this technique as the *lucky region* method [107, 108].

The motion of the atmospheric turbulence causes arbitrary nonlinear distortion to the recorded image frames. Further, when a non-linear system alters signals, quadratic phase coupling (QPC) occurs, which is a specific type of nonlinearity [109, 110]. Quadratic phase coupling relates to the image quality, such that nonlinear detection tools can be used as an image quality metric for lucky region selection. The bispectrum, and its normalization is able to detect and characterize this type of distortion. This is a numerical measure, which will give a numerical scale for the ranking of image quality.

The lucky region method can be extended to different applications. Section 4.7 presents two cases: image recovery for atmospheric turbulence and super resolution reconstruction for atmospheric turbulence. Experiments with both simulated and actual turbulence affected images demonstrate that lucky region selection in the preprocessing step can significantly improve the performance of an image reconstruction system.

4.2 Isoplanatism

Before discussing lucky regions in more depth, we first introduce a common measurement called isoplanantism. In the literature, the isoplanatic angle is defined as the largest angle separation between two point sources where the effect of atmospheric turbulence is effectively uniform.

An image region which subtends the isoplanatic angle is termed an isoplanatic patch. An isoplanatic patch is a spatial region where the PSF is constant within the measurement accuracy[111]. According to this definition, within an isoplanatic region, the imaging system can be modeled by the convolution operation as in Eq.1.1 .

The isoplanatic angle is very small for astronomical observations. Under usual seeing conditions, its value lies within tens of μrad ($\approx 2arcsec$). The mathematical expression for the isoplanatic angle is given by[111]

$$\theta_0 = 58.1 \times 10^{-3} \lambda^{6/5} [\int_0^L dz C_n^2(z) z^{5/3}]^{-3/5} \tag{4.1}$$

where $C_n^2(z)$ is the structure constant of the turbulence induced index of refraction fluctuations over the path length, Z, L is the path length through the atmospheric turbulence, and λ is the optical wave length.

The isoplanatic angle defined in Eq.4.1 is a property of the turbulence distribution, and it is often convenient to use another expression in terms of r_0, the Fried parameter of the most dominant phase screen, and $\widetilde{L}$, the mean turbulence height[111].

$$\theta_0 = \frac{0.314 r_0}{\widetilde{L}} \tag{4.2}$$

where $\widetilde{L}$ is defined as

$$\widetilde{L} = [\frac{\int_0^L dz C_n^2(z) z^{5/3}}{\int_0^L dz C_n^2(z) z}]^{3/5} \tag{4.3}$$

and

$$r_0 \propto [\frac{4\pi^2}{C_n^2(z) z}]^{3/5} \tag{4.4}$$

When there is a single dominant layer of turbulence, $\widetilde{L}$ is the height of that layer. In general application, $\widetilde{L}$ can also be considered to be the screen to pupil distance[2].

4.3 Lucky Imaging

Imaging that there is an idealized astrophysical point source of monochromatic radiation. When it reaches the aperture in the absence of atmospheric turbulence, it would be a plane wave. The aperture function therefore should be uniform across the telescope aperture. When atmosphere turbulence exists, it develops inhomogeneities in the refractive index and therefore changes the characteristics of the aperture function in each observing direction[23]. As a result, the PSF is spatially variant. When observing for a long period, the PSF is also time dependent.

The motion caused by atmospheric turbulence can be frozen if we record an image with a short enough exposure time. Often, the instantaneous distortion of the wave front caused by turbulence may be very severe. However, at other moments, the distortion may be

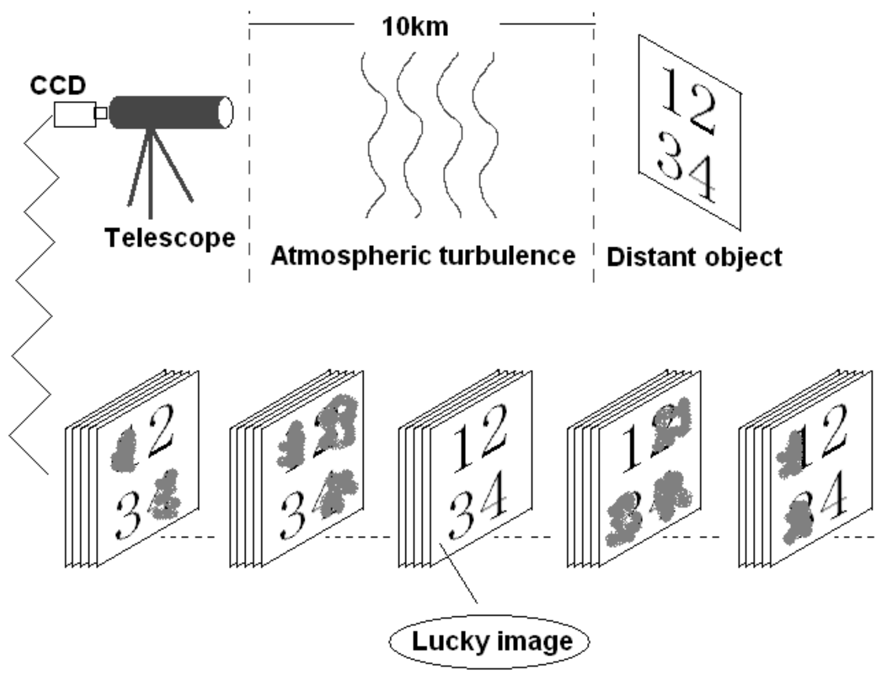

Figure 4.1: Simple illustration of Lucky Imaging.

slight or even negligible, and short exposure images taken at these instants are considered to approach diffraction limited resolution[64]. These images are lucky frames and related techniques are called lucky imaging. The lucky imaging technique first selects observations which are least distorted and have more high frequency information, based on analysis of some image characteristics or statistics. A post processing step is then applied to lucky images to produce a single estimate of the potential image. Fig.4.1 illustrates the process of lucky imaging under atmospheric turbulence.

The chance of obtaining a lucky image, under usual seeing conditions and within the range of the isoplanatic angle, depends on the instrument and the statistics of the turbulence. Fried demonstrated that the occurrence decreases exponentially with the increase in the ratio of the dimension of the telescope aperture D, and the Fried parameter or turbulence-limited coherence diameter r_0, $(D/r_0)^2$ [64]

$$Prob_{lucky\_image} \approx 5.6e^{[-0.1557(D/r_0)^2]} \quad (4.5)$$

Fig.4.2 is a plot of the probability against D/r_0. As demonstrated, the chance of obtaining a lucky image drops significantly with increasing D/r_0, meaning that a very large number of short exposure image must be captured to obtain one near diffraction limited lucky image. For example, to obtain one lucky image with $D/r_0 = 10$, one million short exposure images are needed.

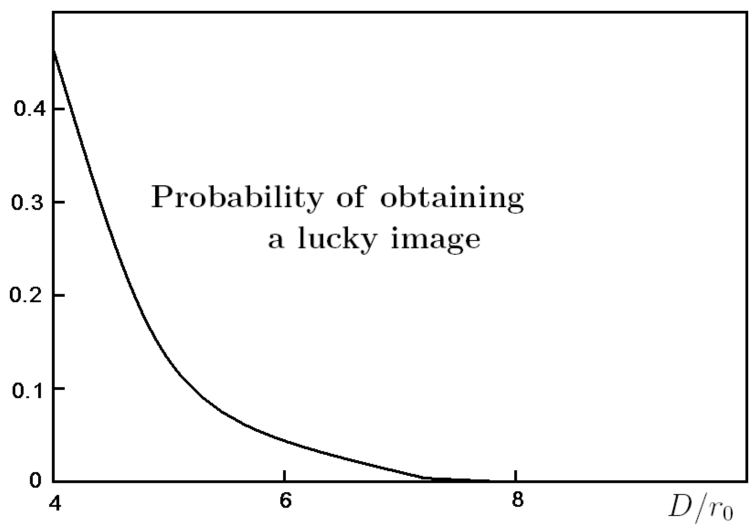

Figure 4.2: Probability of obtaining a lucky image.

One would obtain higher rate of lucky images by sacrificing the resolution of the instrument. For example, replace a larger telescope with a smaller one with only half of the original aperture. Let us imagine that we have $D/r_0 = 10$ using a larger instrument, then drop D/r_0 to 5 using a smaller one. Based on Fried's probability, the chance increases significantly. However, D determines the resolution of the instrument (the larger the aperture the higher the resolution). Therefore an alternative is needed.

4.4 Lucky Region

We notice that in any one short exposure image, rather than being entirely of good quality or entirely poor, and distorted, there will be some superior smaller regions over the image field of view. These regions have better resolution, while the rest of the image area has much poorer resolution. Fried has pointed out in [64] that the probability of obtaining a lucky image can be applied independently to separate isoplanatic patches on the image. We name the technique of predicting and selecting high resolution image regions from a sequence of image frames as *the lucky region technique*, and the image patches with superior quality as *lucky regions*.

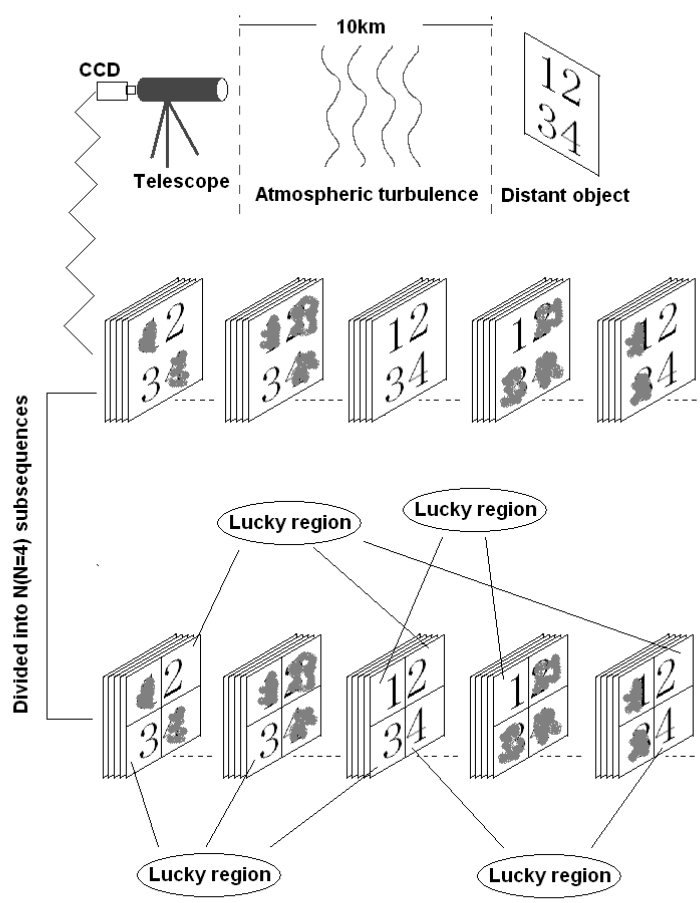

Figure 4.3: Simple illustration of Lucky region.

In practical applications, one would like to segment the raw sequence of frames into a number of sequences of smaller regions. Following this one would determine and rank the distortion within regions in each subsequence using some measures or statistical methods. There are some advantages of image segmentation.

One of the advantages is to have a greater probability of obtaining lucky regions than that of obtaining an entire lucky image under same conditions (i.e., the same distance between the observer and the object, the same observing time, the same atmospheric turbulence and the same D/r_0, etc.). Subdivision implies that there are several smaller components, each of which is the image of a particular part of the scene. These image patches are isolated from each other, and are processed separately.

We demonstrate that the probability of obtaining lucky regions is greater than gaining an entire lucky image in the anisoplanatic case. The probability developed by Fried can be applied independently to separate isoplanatic tiles (or patches)[64]. Denote the probability of lucky region in each image patch is $p_i, (i = 1, 2, 3, \cdots, s)$. If we assume that each image patch is independent from each other, therefore the probability of obtaining an entire lucky image is expressed:

$$Prob_{lucky\_image} = \prod_i p_i \tag{4.6}$$

as $p_i \leq 1$, such that we have $Prob_{lucky\_image} \leq p_i$. Fig.4.3 is a simple illustration of the lucky region technique.

The assumption of taking short exposure images implies that the random wavefront distortion is assumed to remain constant during the exposure. Therefore the exposure needs to be short enough to freeze the wavefront distortion to produce a speckled image, otherwise a blurred, and poorly resolved image (long exposure image) may be captured. Another assumption is that, in the period of observation, there is no change in the strength of turbulence over the propagation path [64], i.e., r_0 is constant. This leads to the fact that the data set should be captured over a reasonable short period of time, but not over a very long period such as over several hours.

Image segmentation can help to reduce the difficulties in post processing for atmospheric turbulence affected images. It especially works under severe turbulent conditions, when the PSF is anisoplanatic. Dividing an image into a number of smaller regions means that the turbulent eddies are also partitioned, each of which only has effects on limited area. Their instantaneous effects on separate image regions can be considered as isoplanatic. Thus a traditional model of image processing like Eq.1.1 can apply to this problem. All discussion throughout this thesis is based on this technique.

4.5 Image Quality Measurement

How can we predict the effect of atmospheric turbulence on wide-area/near-to-ground imaging systems? As we only have a video record of the target, image quality analysis seems to be the only means. In fact, many methods in the literature concentrate on image quality measurement. This section will describes some common (linear) methods.

In general photography, several factors may be associated with image quality, for example, optical artifacts like lens flare and lens distortion, additive noise, exposure accuracy, total response and contrast, etc. Methods predicting image quality in image processing must depend on some sort of image properties.

The simplest method is to use some statistical features on the numerical errors between the distorted image and a reference image such as MSE (mean square error), maximum difference, absolute error, correlation quality, etc[112]. The advantage of these metrics is their simplicity in numerically determining the quality of an image, therefore they can be conveniently adapted by different imaging systems.

MSE is the average of the square of the difference between the true image and the estimate[113]. Let i and i_e denote the ground truth image and the tested image, respectively, then the MSE is given by

$$MSE(i_e) = E[(i_e - i)^2] \tag{4.7}$$

Another method, the correlation quality, calculates the correlation between the tested image and the reference image[114].

$$CQ(i_e) = (\sum_k \sum_l i_e(k,l) i(k,l)) / \sum_k \sum_l i(k,l) \tag{4.8}$$

There is a method which considers the noise in an image: PSNR (pseudo signal-noise-ratio). In this context, “noise” is the RMS (root mean square) difference between a simulated or resultant image and the original image. The PSNR is given by:

$$PSNR = 20 \log(\frac{\sqrt{i^2}}{\sqrt{i^2 - i_e^2}}) \tag{4.9}$$

Image contrast is another common method. Various definitions are used in different situations, but the luminance is commonly applied in the literature:

$$CON = \frac{\text{Luminance difference}}{\text{Average luminance}} \tag{4.10}$$

If the luminance difference is defined by the difference of the luminance of the features and the background luminance, and the average luminance is performed on the background, then it is a Weber contrast. Another definition is called Michelson contrast, which is

$$CON_{Michelson} = \frac{i_{max} - i_{min}}{i_{max} + i_{min}} \tag{4.11}$$

where i_{max} and i_{min} represent the highest and lowest luminance, respectively[115].

Sharpness, as an important property of an image, is an useful measurement of an image quality. There are a number of definitions of sharpness, some needs a reference true image and others do not[116]. The following are two commonly used sharpness metrics

$$S = \int\int [i - i_a]^2 dxdy \tag{4.12}$$

and

$$S = \int\int \frac{\partial i}{\partial x} + \frac{\partial i}{\partial y} dxdy \tag{4.13}$$

where x and y are the image coordinates, and i_a in Eq.4.12 is the mean of gray level of the image i. These formulae have no true image involved, which is more suitable for real-world application such as in wide-area imaging.

An alternative generic measurement of image quality has been proposed by Wang and Bovik to predict image quality using three factors: loss of correlation, luminance distortion, and contrast distortion[117].

$$M = \frac{4\sigma_{i_e i}\overline{i_e}\ \overline{i}}{(\sigma^2_{i_e i_e} + \sigma^2_{ii})[(\overline{i_e})^2 + (\overline{i})^2]} \tag{4.14}$$

where $\overline{i_e}$ and $\sigma^2_{i_e i_e}$, and $\overline{i}$ and σ^2_{ii} are the expectation and the variance of i_e and i, respectively, $\sigma_{i_e i}$ is the covariance of i_e and i. The value of M lies on $[-1, 1]$, when $i_e = i$ or i_e is close to i, M gains the best value 1. M tends to -1 when i_e is very different from i.

Note that the methods developed above produce a single scale value to rank the image quality and therefore can be widely used. However, these conventional methods are designed for linearly produced images so that they cannot be simply applied in our problem due to the nature of atmospheric turbulence. A new, nonlinear algorithm must be proposed. In this thesis, we consider the distortion caused by atmospheric turbulence as a nonlinear process (in particular, a quadratic phase coupling problem). Taking advantage of higher order statistics, we use bicoherence to be a quality indicator.

4.6 Bicoherence

In the past decades, general relations for signals passing through linear systems and methods for the distortion removal have been extensively studied and exploited[101]. However, not much work has been done for the nonlinear case. Instead, each type of nonlinearity has been investigated as a special case[110, 118].

Quadratic phase coupling, one type of nonlinearity, is a strong indicator of a nonlinear process[119]. When a signal passes through a system, two harmonic components interact with each other and cause contribution to the power at their sum and/or difference frequencies. This phenomenon gives rise to certain phase relations, and is called quadratic phase coupling[101, 120, 121].

Such phase relations can be detected and characterized by the bispectrum and its normalization, the bicoherence. The complex-valued bispectrum is often recast into the bicoherence (its normalized magnitude) and the biphase (its phase). Here we redefine the triple correlation and the bispectrum of a signal $f(t)$, which has the form $f(t) = \sum_{k=-\infty}^{\infty} h(k)e(t-k)$, where $h(t)$ is the impulse response which is square summable, and $e(t)$ is a sequence of independent and identically distributed (i.i.d.) random variables with zero means[122]. The triple correlation is then

$$\begin{aligned} f^{(3)}(\tau_1,\tau_2) &= E\{f(t)f(t+\tau_1)f(t+\tau_2)\} \\ &= \mu_{3e}\sum_{k=-\infty}^{\infty} h(k)h(k+\tau_1)h(k+\tau_2) \end{aligned} \tag{4.15}$$

and the bispectrum is

$$\begin{aligned} F^{(3)}(u_1,u_2) &= \sum_{\tau_1=-\infty}^{\infty}\sum_{\tau_2=-\infty}^{\infty} f^{(3)}(\tau_1,\tau_2)e^{-j2\pi(u_1\tau_1+u_2\tau_2)} \\ &= \mu_{3e}H(u_1)H(u_2)H(-u_1-u_2) \end{aligned} \tag{4.16}$$

where E is the expected value, $\mu_{3e} = E\{e^3(t)\}$, and $H(\cdot)$ is the Fourier transform of $h(t)$.

The biphase is often used for phase retrieval, and is defined as the phase of the bispectrum

$$\varphi_{F^{(3)}(u_1,u_2)} = \arctan\frac{Im\{F^{(3)}(u_1,u_2)\}}{Re\{F^{(3)}(u_1,u_2)\}} \tag{4.17}$$

The bicoherence, which is a normalized version of the bispectrum, indicates the phase relationship among sets of frequency components at u_1, u_2, and u_1+u_2. If there is no correlation or coupling in a phase set (u_1,u_2,u_1+u_2), the bicoherence value will be equal or close to zero. This property enables the bicoherence to be adopted to detect the degree of phase coupling in an image, and therefore predict the quality of an image. In this thesis, the bicoherence as an image measurement is studied and exploited.

4.6.1 Definition and Properties of the Bicoherence

Based on Eq.4.16, the standard normalization of bispectrum is defined as

$$\begin{aligned} s(u_1,u_2) &= \frac{F^{(3)}(u_1,u_2)}{\sqrt{F(u_1)F(u_2)F(u_1+u_2)}} \\ &= \gamma_e e^{j(\phi(u_1)+\phi(u_2)+\phi(u_1+u_2))} \end{aligned} \tag{4.18}$$

where $F(\cdot)$ is the Fourier transform of $f(t)$, $\phi(\cdot)$ is the Fourier phase, and γ_e is the skewness of $e(t)$. The magnitude $|s(u_1, u_2)|$ is termed a skewness function, and also called the bicoherence spectrum in signal processing[120, 123].

However, this term may be larger than one. General normalization implies that the bicoherence is always expected to be bounded by one. To do so, an alternative form is defined. In particular, Kim and Powers[124] define the bicoherence as

$$b(u_1, u_2) = \frac{|F^{(3)}(u_1, u_2)|}{\{E[|F(u_1)F(u_2)|^2]E[|F^*(u_1 + u_2)|]^2\}^{1/2}} \tag{4.19}$$

another form of the bicoherence is given by Haubrich[125]

$$b(u_1, u_2) = \frac{|F^{(3)}(u_1, u_2)|}{\{E[|F(u_1)|^2]E[|F(u_2)|^2]E[|F^*(u_1 + u_2)|]^2\}^{1/2}} \tag{4.20}$$

For a broad-band system, a particular Fourier component may be involved in many interacting triads $(u_1, u_2, u_1 + u_2)$, and there is no simple interpretation of the bicoherence value. In practice, for a finite length signal, even a process with truly independent Fourier components (e.g., a Gaussian process) will have a nonzero bispectrum[126]. Therefore one would expect that the bicoherence lies between [0,1].

The bicoherence of a single data record can be estimated by using a Welch segment-averaging approach. Suppose that we have an N-point record, the data is divided into m segments with length n, where $n = N/m$, and here the frequency resolution is $\triangle u = 1/n$. Then rewrite Eq.4.19 and 4.20 as

$$b(u_1, u_2) = \frac{|\sum_{i=1}^{m} F_i(u_1)F_i(u_2)F_i(u_1 + u_2)|}{\{\sum_{i=1}^{m} |F_i(u_1)F_i(u_2)|^2 \sum_{i=1}^{m} |F_i(u_1 + u_2)|^2\}^{1/2}} \tag{4.21}$$

$$b(u_1, u_2) = \frac{|\sum_{i=1}^{m} F_i(u_1)F_i(u_2)F_i(u_1 + u_2)|}{\{\sum_{i=1}^{m} |F_i(u_1)|^2 \sum_{i=1}^{m} |F_i(u_2)|^2 \sum_{i=1}^{m} |F_i(u_1 + u_2)|^2\}^{1/2}} \tag{4.22}$$

The bicoherence has the following properties which enable it to estimate the interaction of a signal with a non-linear disruption such as atmospheric turbulence[101, 127, 128]:

- the bicoherence is two-dimensional for a one-dimensional signal and four-dimensional for a two-dimensional signal;
- $0 < |b(u_1, u_2)| < 1$;
- $|b(u_1, u_2)|$ can measure the degree of nonlinearity in a process under certain assumptions[119].

Such properties highlight the feasibility of the bicoherence as an estimator for nonlinear disruption. Actually, the usage of the bicoherence for nonlinearity detection has been studied in various areas, such as computer vision [129], speech signal processing [130], analysis of plasma turbulence[127] and nonlinear aeroelastic phenomena [128].

Motivated by these successful applications, we studied and developed a method for using the bicoherence to detect and characterize quadratic phase coupling in images taken through atmospheric turbulence. In other words, the bicoherence, in this thesis, acts as an image quality measurement for lucky region selection.

4.6.2 Nonlinearity Detection

How does bicoherence predict a nonlinear process? Let us consider a nonlinear system case in the following [127]

$$\frac{\partial u(x,t)}{\partial x} = f(u(x,t)), \tag{4.23}$$

where $u(x,t)$ and $f(u)$ are continuous nonlinear functions. Analyzing f with a Taylor series we then have

$$f = f_1 + f_2 + f_3 + \cdots \tag{4.24}$$

where $(f_1, f_2, f_3, \cdots,)$ are the linear, quadratic, cubic and higher order functions. Eqs.4.23 and 4.24 can be written as a Volterra series with some mild assumptions[127]

$$\begin{aligned}\frac{\partial u(x,t)}{\partial x} &= \int g(\tau_1)u(x,t-\tau_1)d\tau_1 \\ &+ \int\int g(\tau_1,\tau_2)u(x,t-\tau_1)u(x,t-\tau_2)d\tau_1\tau_2 \\ &+ \int\int\int g(\tau_1,\tau_2,\tau_3)u(x,t-\tau_1)u(x,t-\tau_2)u(x,t-\tau_3)d\tau_1\tau_2\tau_3 \\ &+\cdots\end{aligned} \tag{4.25}$$

Take the discrete Fourier transform $(t \rightarrow w)$ of both sides and let $u_p = u(x, \omega_p)$

$$\frac{\partial u_p}{\partial x} = \Gamma_p u_p + \sum_{m,n} \Gamma_{mn} u_m u_n \delta_{m+n,p} + \sum_{m,n,k} \Gamma_{mnk} u_m u_n u_k \delta_{m+n+k,p} + \cdots \tag{4.26}$$

Each term in Eq.4.26 represents a different physical process. The second and the third terms describe the coupling between different Fourier phases. Γ_{mn} describes three wave interactions (three different Fourier modes are involved, also called quadratic nonlinearity) and Γ_{mnk} describes four wave interactions (termed cubic nonlinearity). The relationship between the frequencies can be expressed

$$\omega_p = \omega_m + \omega_n \tag{4.27}$$

for quadratic nonlinearity, and for cubic nonlinearity it is given by

$$\omega_p = \omega_m + \omega_n + \omega_k \tag{4.28}$$

Multiply both sides of Eq.4.26 by u_p^*, and calculate its expectation, we then have the expression of higher order spectra:

$$\langle \frac{\partial u_p}{\partial x} u_p^* \rangle = \Gamma_p \langle |u_p|^2 \rangle + \sum_{m+n=p} \Gamma_{mn} \langle u_m u_n u_{m+n}^* \rangle + \sum_{m+n+k=p} \Gamma_{mnk} \langle u_m u_n u_k u_{m+n+k}^* \rangle + \cdots \quad (4.29)$$

The first term on the right side of Eq.4.29 is the power spectrum

$$U_{\omega_p}^{(2)} = \langle u_p u_p^* \rangle = \langle |u_p|^2 \rangle \quad (4.30)$$

The second term gives the bispectrum

$$U_{\omega_p}^{(3)} = \langle u_m u_n u_{m+n}^* \rangle \quad (4.31)$$

and the cubic term is called trispectrum

$$U_{\omega_p}^{(4)} = \langle u_m u_n u_k u_{m+n+k}^* \rangle \quad (4.32)$$

Eq.4.31 implies that there exists interaction between phase components u_m,u_n and u_{m+n}, and this relation is retained in the bispectrum. To detect such phase relation (or quadratic phase coupling), generally, the normalized bispectrum or the bicoherence is used[122]. A nonzero bicoherence means that the bifrequency (u_m, u_n) is phase coupled to u_{m+n} to some degree. When the phase coupling vanishes the bicoherence reaches its lowest value. Note that, even for a process with truly independent Fourier phase and zero mean, its bicoherence will not reach zero in practical calculations[126]. Therefore, in the application of image processing, we expect that the bicoherence lies in the middle of the range [0,1].

Fig.4.4 shows the bicoherence of a one-dimensional signal which is a scan line of an image. The light area indicates that the bifrequencies at (u_m, u_n) have a higher degree of phase coupling to u_{m+n}, such as $(10, 40, 50)$, $(30, 22, 52)$, and $(52, 30, 82)$.

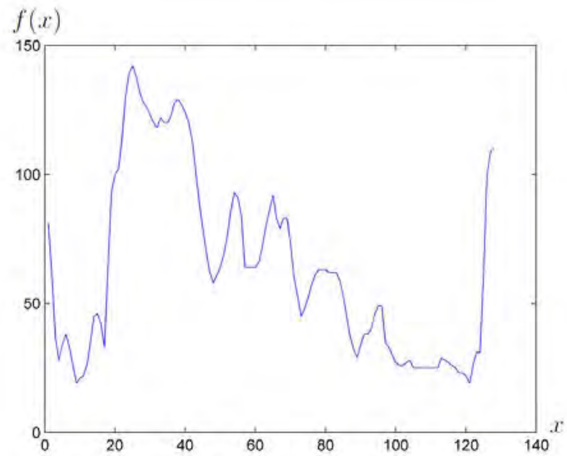

(a)

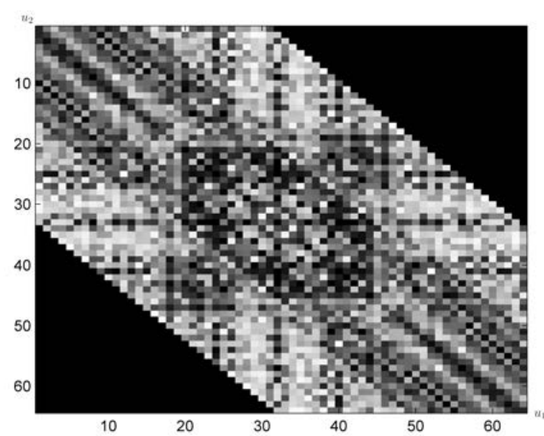

(b)

Figure 4.4: An example signal (a) and its bicoherence. The lighter area indicates a higher value of the bicoherence, thus having a higher degree of quadratic phase coupling.

4.7 Lucky Region Selection

This section explains how to use bicoherence as an image quality indicator for lucky region selection. It is experimentally shown that the bicoherence obtained using one-dimensional scan lines of an image and using the two-dimensional matrix have similar characteristics, such that the former method can be used to avoid heavy-computing in practical applications. Moreover, a discussion about how to set the threshold of lucky regions is given. In our application, these lucky images are less perturbed by the turbulence.

4.7.1 Methods for Computing Bicoherence

From Eq.4.21 and 4.22, we notice that the bicoherence inherits some properties from the bispectrum, such as its dimensions are four for a two-dimensional signal. Therefore the computation of the bicoherence of an image is time consuming and needs a great deal of computer memory.

To improve the conditions, we consider restricting the computation from a two-dimensional matrix to the one-dimensional scan-lines or columns of the matrix. This is reasonable because the phase correlations between spatial frequencies in an image region are similar to those in the one-dimensional scan-lines or columns[129, 131]. Moreover, the statistics of bicoherence shows that the distribution of bicoherence values obtained by a two-dimensional matrix is very similar to the distribution of bicoherence processed using a one-dimensional but longer vector [126].

This characteristics of bicoherence can be demonstrated by experiment. Fig.4.5 shows two curves (the bicoherence value) calculated from the same image by using one-dimensional scan lines (dotted line) and by using two-dimensional matrix (solid line), separately. Both lines have very similar shape though they have a little difference in value range, which

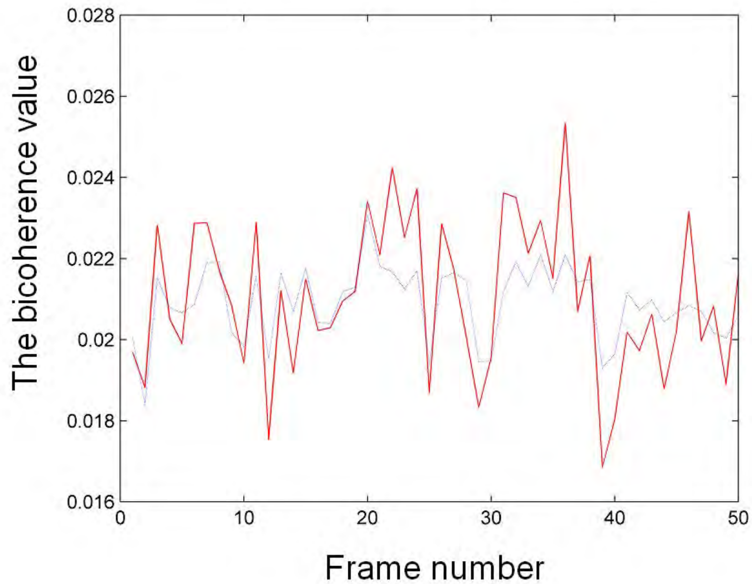

Figure 4.5: The averaged bicoherence (see Eq.4.34 computed using one-dimensional scan lines in the image domain has similar characteristics with that calculated using the two-dimensional formula. The values of the averaged bicoherence of 50 distorted frames are plotted. The red solid line presents the values using two-dimensional image while the blue 'thicker' dotted line is from one-dimensional scan lines in the image domain. Both curves have similar shape, which gives similar estimation of the quality of image blockes, but importantly, the vertical range of both are co-confined.

implies that the bicoherence computed by both means have similar characteristics.

Therefore, in this thesis, the bicoherence calculation is restricted to the scan lines or columns. Here, we rewrite the equation used in estimation of the bicoherence of an image region

$$\begin{aligned} b(u_1, u_2) &= \frac{|\frac{1}{M}[\sum_{s=0}^{M-1} I_s(u_1)I_s(u_2)I_s^*(u_1+u_2)]|}{\sqrt{\frac{1}{M}[\sum_{s=0}^{M-1}|I_s(u_1)I_s(u_2)|^2]\cdot\frac{1}{M}[\sum_{s=0}^{M-1}|I_s^*(u_1+u_2)|^2]}} \\ &= \frac{|[\sum_{s=0}^{M-1} I_s(u_1)I_s(u_2)I_s^*(u_1+u_2)]|}{\sqrt{[\sum_{s=0}^{M-1}|I_s(u_1)I_s(u_2)|^2]\cdot[\sum_{s=0}^{M-1}|I_s^*(u_1+u_2)|^2]}} \end{aligned} \tag{4.33}$$

where $I_s(\cdot)$ is the Fourier transform of the sth scan line/column, u_1 and u_2 are the frequency coordinates. Thus, $b(u_1, u_2)$, is the bispectrum averaged over M scan lines/columns, then normalized by the averaged power of the corresponding frequency components.

Finally, an averaged bicoherence over all frequency components is formed to provide a scalar indicator of the degree of phase coupling. If there is little or no phase coupling between two frequencies, the value of the bicoherence will be close to zero. If the phase relationship between different frequency components partially exists, the value of the bicoherence will lie between zero and one. If the degree of phase coupling is high, then the value of the bicoherence will be close to unity. For this reason, we can expect that the averaged bicoherence of a signal will increase as the degree of quadratic phase coupling grows.

There are three means to compute the averaged bicoherence, one is to compute the average bicoherence over the horizontal lines in an image region

$$b_h = \frac{1}{N_h}\sum_{k=1}^{N_h}[\frac{1}{N_{u_1}N_{u_2}}\sum_{u_1=0}^{N_{u_1}-1}\sum_{u_2=0}^{N_{u_2}-1} b_k^{hor\_line}(u_1,u_2)], \tag{4.34}$$

the second way is to restrict the computation to the vertical columns

$$b_v = \frac{1}{N_v}\sum_{k=1}^{N_v}[\frac{1}{N_{u_1}N_{u_2}}\sum_{u_1=0}^{N_{u_1}-1}\sum_{u_2=0}^{N_{u_2}-1} b_k^{ver\_line}(u_1,u_2)], \tag{4.35}$$

and another alternative is the combination of the former two estimations:

$$b_c = \sqrt{b_h^2 + b_v^2}, \tag{4.36}$$

where N_h and N_v are the number of horizontal and vertical scan lines of an image region, $b_k^{hor\_line}$ and $b_k^{ver\_line}$ are the bicoherence of the kth horizontal and vertical lines, and is calculated by Eq.4.33. N_{u_1} and N_{u_2} represent the number of sampled frequencies u_1 and u_2. Note that b_h, b_v, and b_c are each **a single value** which represents the average of the bicoherence over the frequency domain.

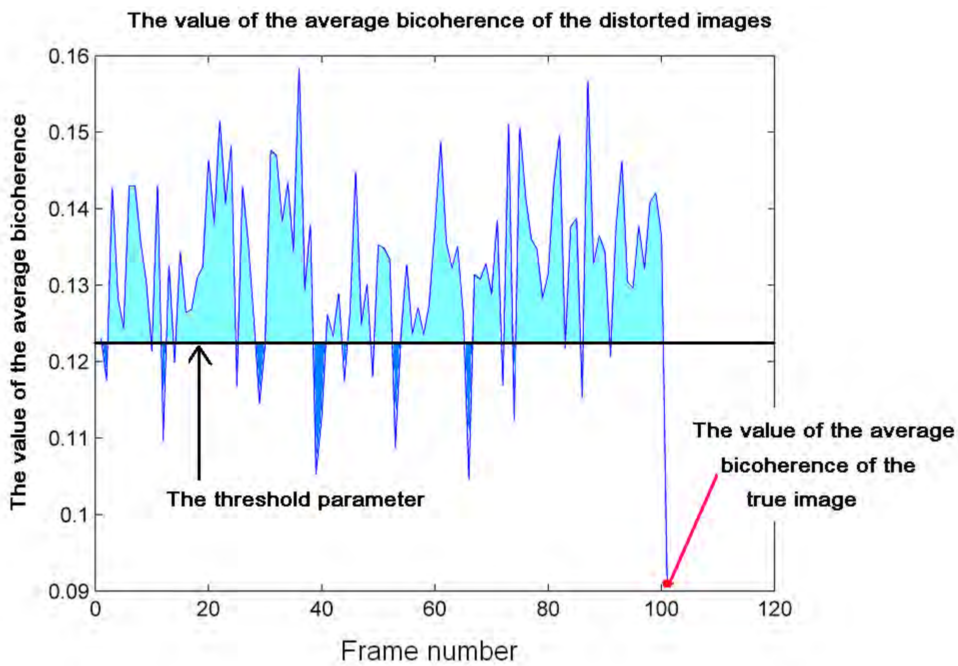

Figure 4.6: Comparison of the value of the bicoherence of a true image and simulated atmospheric turbulence affected images. A low value implies less effect by the turbulence and hence a low level of phase coupling. The original image can be expected to have lowest bicoherence. The threshold that selects lucky frames or regions over more degraded images may be chosen based on the data sequence.

The lucky regions are selected according to the order of the value of the averaged bicoherence of each region in the image region sets. Based on the rate of lucky regions, one can set a threshold parameter for selecting lucky images. Recall that the interaction caused by the turbulence in the imaging path will create coupling in the bispectrum of each region, and hence lower coupling implies lesser effect of the turbulence. Keeping the regions that have lower averaged bicoherence as lucky regions and discarding the other regions, one can select a sequence of lucky regions among the given distorted image set. Observations over many images will populate the missing regions.

Fig.4.6 shows the averaged bicoherence for a sequence of 100 simulated turbulence-affected images using the Lenna test image. Badly affected images have high values of

Table 4.1: Lucky images and non-lucky images and their mean bicoherence values. Lucky images have less averaged bicoherence, are more geometrically correct to the truth image and have more details, only by visual inspection.

lucky images	mean bicoherence	non-lucky images	mean bicoherence
	(true image)0.092		
	0.105		0.151
	0.110		0.158
	0.109		0.157
	0.105		0.151
	0.112		0.151

averaged bicoherence, while low values indicate lucky images.

For the purpose of detailed comparison, images with smallest and largest values are listed in Tab.4.1. The corresponding averaged bicoherence value for each image are also included. Again, one can tell that images having less averaged bicoherence value are superior, more geometrically correct to the truth image and have more details, only by visual inspection.

4.7.2 The Threshold

The number of lucky regions should be set before running the algorithm. The threshold used in this thesis is 20% of the whole set of raw images. This number can be manually set and could be varied to suit the data.

In our experimentation with simulated atmospheric turbulence, different rates with isoplanatic simulated data (Lenna) were tested. Fig.4.7 lists the results using 5%, 20%, 40% and 60% of the whole sequence of raw images. For better comparison, only a part of the image is shown.

As expected, the result becomes better when the number of lucky regions increase (but the number is still relatively small, i.e., the lucky region ratio is less than 20%), then reaches a peak before it begins to get worse when the number continues to increase($>$ 40%). In Fig.4.7, the result with lucky region ratio of 5% and 60% are more blurred and less geometrically accurate (for example, the edges), which is due to there being less information (in 5%) or more ambiguities (in 60%) when using smaller or larger ratios.

The results using 20% and 40% are very similar, which indicates that reasonable optimization may occur between 20% and 40%. By taking the computation time into account, the former should be a better choice.

(a)5%

(b)20%

(c)40%

(d)60%

Figure 4.7: Results from processing lucky regions with different lucky ratios: (a) 5%; (b)20%; (c)40%, and (d)60%. For the purpose of detail comparison, only a part of the image is shown. (a) and (d) are more blurred and less geometrical accurate (the edges), which is the result that less information (in 5%) and more ambiguities (in 60%) using smaller or larger ratios. (b) and (c) are very similar, which indicates that reasonable optimization may occur between 20% and 40%.

So far, new sequences of lucky regions have been produced from old sequences of raw image subregions. These lucky regions are kept by themselves until further processing by the bispectrum or other methods are performed.

4.8 Applications

The lucky region technique can be applied in other areas as a preprocessing technique, when turbulence is involved and the turbulent media has similar statistics to those of atmospheric turbulence exists. In the research of this thesis, we studied two applications: image reconstruction and possible super resolution for wide-area imaging. In the following, effective algorithms are developed, and their performance are tested by both simulated and real-world data.

4.8.1 Image Reconstruction from Atmospheric Turbulence

Given a number of short exposure images taken through atmospheric turbulence, the task of image reconstruction of the potential image is challenging due to the PSF being time varying and position dependent (which is the result of movement of the atmospheric eddies), as discussed in previous chapters. Common methods use information retained in all the raw images and produce a version of the potential image based on this information.

It was believed that each short exposure image is helpful because it contains useful information for the image reconstruction process. The more the short exposure images, the more the information we have, and the better the reconstructed result may be. However, our experimental results show a different case. Fig.4.7 is an example. The quality of the estimation indeed improves with the number of short exposure images when the number is small. When the number of images used for construction reaches a certain threshold, the processing produces a best result. If the number keeps increasing, then the result becomes worse.

Our explanation is that a short exposure image not only contains useful information but also brings harmful uncertainty. The useful information helps the estimation approach the potential image while the uncertainty makes the result worse. When the number of images used for reconstruction is very large, the ambiguities increase, compromising the useful information, leading to a worse result. One would expect to improve the result by using as much helpful information as possible and decreasing harmful ambiguities from the data source.

Lucky region is such a technique to select superior image subregions retaining relatively more useful information and less ambiguities than non-lucky regions. Thus subsequent processing steps on lucky regions will produce a better result.

The simplest method is to temporally average the lucky regions in each sequence, obtaining a single estimation for each image patch, which is followed by combining all the estimations of each image tile to their correct position to form a single sharp image. This method is similar to the average-based method: temporally average the ensemble images[132, 107]. The result produced by this method may be geometrically correct but low-pass filtered, so that the restored image is still blurred with some of its high frequency content being lost.

An alternative is to recover the target image using the bispectrum technique discussed in Chapter 3. Compute the average of the bispectrum of each sequence of lucky regions, the average bispectrum is then used to reconstruct a single image region. Finally, all the regions are repositioned to fuse an estimation of the potential image.

Fig.4.8 and Fig.4.9 list the results obtained using lucky regions. The data is simulated using the lenna image, with 100 successive frames. The data used for experimenting in Fig.4.8 is isoplanatic patches simulated data, and the data in Fig.4.9 is anisoplanatic. The

(a) SNR = 11dB

(b) SNR = 12dB

(c) SNR = 14dB

(d) SNR = 15dB

(e) SNR = 19dB

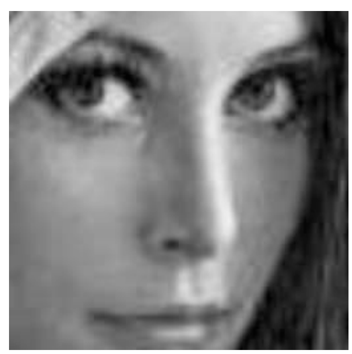

(f) The true image

Figure 4.8: Comparison of results of the isoplanatic simulated data by different methods: (a) an input image, (b) result using the regions that have minimum MSE, (c) result by the average-based method, (d) result by averaging the lucky regions, (e) result by our algorithm, (f) The true image. The result by our algorithm has the best signal-noise-ratio and exhibits the sharpest and closest match to the truth image visually.

isoplanatic distortion of the sequence is computed according to the following. If O is the Fourier transform of an original or true test image, o, then we form a sequence by adding a simulated Kolmogorov phase screen to its phase:

$$I_k(u,v) = O(u,v)e^{j\phi_k(u,v)} \tag{4.37}$$

where I_k is the Fourier transform of the kth simulated image, i_k, in (u,v) spatial frequencies and ϕ_k, is the kth randomly generated Kolmogorov phase screen. The phase screen generator function was kindly provided by the University of Canterbury [133]. The function allows the user to select the ratio D/r_0.

The Lenna sequence used in Fig.4.8 is an isoplanatic sequence formed directly by the application of Eq.4.37, with $D/r_0 = 5$. A set of 200 randomly phase-distorted images was produced. A frame from the simulated sequence is shown in Fig.4.8(a).

In the anisoplanatic case, five different Kolmogorov phase screens with $D/r_0 = 1, 3, 5, 7, 2$ have been used to produce each of a set of simulated isoplanatic turbulence affected images. This method employed the Layered algorithm in [134], using a simulated monochromatic wavelength of 500 nm, simulated layers at distances 5, 45, 55, 70, 105 m from the telescope and simulated sensor used to gather the imagery, ($D = 0.14m$, $f14$, $\Delta_{pixel} = 7\mu m$). In this case, a set of 100 images was produced, using a different randomly generated phase screens for each layer and each image. The resultant images (for example, see Fig.4.9(a)) exhibit space variant warping as expected of anisoplanatic distortion. Because of the monochromatic simulation they also exhibit variations in amplitude or scintillation caused by the diffraction between layers. A broadband simulation would make these scintillations less noticeable.

To estimate the isoplanatic patch angle, θ_0, Eq.4.3 is used. Let us assume that the isoplanatic patch size in the simulation is determined mainly by the $D/r_0 = 7$ ratio at

(a) SNR = 11dB

(b) SNR = 12dB

(c) SNR = 14dB

(d) SNR = 15dB

(e) SNR = 19dB

(f) The true image

Figure 4.9: Comparison of results of anisoplanatic simulated data by different methods: (a) an input image, (b) result using the regions that have minimum MSE, (c) result by the average-based method, (d) result by averaging the lucky regions, (e) result by our algorithm, (f) The true image. Example frames from the simulated sequence also exhibit coarse variation in amplitude or scintillation as a result of the diffraction between turbulent layers and the pupil for a quasi-monochromatic illumination. The result by our algorithm has the best signal-noise-ratio and exhibits the closest match visually to the truth image and appears unaffected by the frame varying scintillation.

$L_{scr} = 70$ m. Then, for a pupil size of 0.14 m, giving $r_0 = 0.14/7 = 0.02$ m, we find $\theta_0 = 8.97 \times 10^{-5}$ rad, or 18.5 arcsec. With a focal length $f = 1.96$ m and CCD pixel size of 7μ m, the isoplanatic patch size is 25×25. This size is quite close to our working region size.

The average bicoherence was calculated for each region of 32×32 pixels, with 50% overlap, in each image. A threshold was chosen in our experiments such that the ratio of lucky regions found to the whole image set was 20%. This ratio is selected based on earlier experiments and discussion, but can be varied to suit the data.

In both experiments, results by other methods are also listed in Fig.4.8 and Fig.4.9. (b) is the result using lucky regions selected by minimum MSE method, and (c) is the temporal average of the total raw images. The comparison demonstrates that bicoherence as an image quality measurement helps to select images with more high frequency information and less distortion, therefore improving the performance of the succeeding image process. Comparing the results by the method of averaging the lucky regions (d) and by the bispectrum method (e), one can notice that the bispectrum technique produce more impressive results which are closer to the true image (f). The PSNR of each result are also shown in figures, verifying our observation.

4.8.2 Super Resolution from Atmospheric Turbulence

This subsection demonstrates the possibility of super resolved image reconstruction for images taken through atmospheric turbulence. Moreover, we combine the lucky region technique and conventional super resolution approaches to solve the problem. Results with real field data are shown.

4.8.2.1 Possibility of Super Resolution

Problems in imaging through turbulent atmosphere are common to earth-based astronomy and to surveillance by telescope. In both cases, the intervening atmospheric turbulence between an object of interest at a large distance from the observing device may result in severe distortion of the image. If a sequence of many images is captured, it is possible to obtain a "diffraction-limited" image of a stationary object or scene by speckle imaging[29, 30].

The diffraction limit is the theoretical image resolution of a telescope, which depends on the diameter of the telescope's objective, its optical quality and the wavelength of the light. Theoretically, the angular resolution of an optical telescope is:

$$res_o = 1.22\frac{\lambda}{D} \tag{4.38}$$

where λ is the wavelength and D is the aperture. The larger the aperture, the better the angular resolution. This theoretical resolution works under conditions that no atmospheric turbulence exists, i.e., there is no medium (e.g., the air) lying between the object and the telescope.

When atmospheric turbulence exists, the telescope resolution will be worse, and Eq.4.38 will not work. Instead, the resolution depends on the Fried parameter instead of the aperture,

$$res_{real} = 1.22\frac{\lambda}{r_0} \tag{4.39}$$

where r_0 is the Fried parameter, representing the diameter of coherent cells in the incident wave at the telescope pupil.

In this context, super resolution means achieving resolution better than the diffraction limit, i.e, the resolution is higher than res_{real}, and in some cases higher than res_o. It has been shown that in restoring images taken through atmospheric turbulence, it is both theoretically and practically possible to achieve such super resolution using a number of short exposure images [135, 136].

It turns out that, in some circumstances, short exposure images can bring a bonus by improving the resolution of a telescope even beyond the theoretical diffraction limit, because the turbulence may warp spatial frequency information outside the diffraction limit into the aperture of a telescope. The warping of higher spatial frequency content into the aperture has been demonstrated in the laboratory [137], shown experimentally in the field[135, 134, 138], proven analytically[139], and shown that if successful restoration is applied, can gain results that would be appropriate for a telescope many times the diameter of the current telescope [139]. In other words, from the view of a long enough observing period, we obtain a relatively larger r_0. So, if a restoration algorithm can collect this higher spatial frequency information from a sequence of images captured through a telescope, a higher resolution result or super resolution may be possible. The observed images are still no more than diffraction limited but their inherent distortion that we must correct carries information normally only found outside the pupil, but here warped in as low frequency content.

4.8.2.2 The Proposed Algorithm

Super resolving atmospheric turbulence affected images is challenging. General super resolution techniques assume that the PSF is position independent, and reasonable result may be obtained using only one or a small number of images [140, 141]. In imaging through turbulence, especially in wide-area/near-to-ground imaging, the PSF is likely to be anisoplanatic (spatially-variant and time-varying) with severe information loss due to the rapid motion and change of the turbulent eddies as we discussed before. To overcome the effect of atmospheric turbulence, and achieve a super resolved result, new techniques using multiple short exposure images are proposed in this thesis.

As a large number of short exposure images is recorded, some having superior quality and the others are worse as we discussed in the previous sections, data classification should be considered before super resolution methods are applied. The algorithm proposed in this thesis uses the lucky region technique for good quality data selection, and a super resolved image is then reconstructed using lucky regions[142, 108].

One would notice that data classification and selection may decrease r_0 as a result of the drop in the number of images used for super resolution reconstruction. However, this is not the fact. Lucky regions are partition of the whole sequence of image frames, and they are superior and more geometrically correct, retaining more useful information than others. This leads to the fact that lucky region selection does boost r_0.

The proposed algorithm is a two-step super resolution method using multiple images: bicoherence is used to select image regions with superior quality in the first step, following which a MAP estimation based on a Universal Hidden Markov Tree (uHMT) model is employed to produce a single super resolved image [108, 143].

We proposed an effective super resolution algorithm, the MAP-uHMT method, which can be applied to this problem[143] in collaboration with Li who was a Ph.D student in our group. Li's algorithm is to solve the following model:

$$g_i = DH_iM_iz + n_i, \quad i = 1, \cdots, K \tag{4.40}$$

where z is an ideal data with high resolution; g_i is the i^{th} observed short exposure image; K is the number of short exposure images; M_i is the region to region warping presented as an affine transform,; H_i is the inherent blur to the image caused by the r0 of the turbulence;

D is a sub-sampling matrix, and n_i represents additive noise of Gaussian distribution with zero mean.

The task is to estimate z using a set of g_i, given Eq.4.40. Using uHMT model in the wavelet domain and the MAP estimator, the problem now is to calculate an optimal solution by minimizing the cost function:

$$L(z) = \sum_{i=1}^{K} \frac{1}{2\lambda_i^2} \parallel g_i - DH_iM_iz \parallel^2 + \phi(z,\theta). \tag{4.41}$$

${\lambda_i}^2$ is the noise variance of n_i in the i^{th} image. The function $\phi(z,\theta)$ is the energy function which is regarded as the energy attributed to z. This term comes from the prior probability.

The problem now is to construct the energy function (or the prior model) $\phi(z,\theta)$. We introduce the wavelet domain uHMT model originally developed for signal denoising and signal estimation[144] to this application. For simplicity, let us assume the marginal probability density functions of the wavelet coefficients are conditionally independent, although the state values between the parent wavelet coefficients and the child wavelet coefficients are dependent. Then a prior model used in [143] is adopted. $L(z)$ can be rewritten as:

$$\begin{aligned} L(z) = \sum_{i=1}^{K} \frac{1}{2\lambda_i^2} \parallel \widetilde{g}_i - \widetilde{D}\widetilde{H_i}\widetilde{M_i}z \parallel^2 \\ + \sum_{\xi=1}^{N^2} \frac{\widetilde{z_\xi}^2}{2(P_{S_\xi}(1)\sigma_\xi(1)^2 + P_{S_\xi}(2)\sigma_\xi(2)^2)}, \end{aligned} \tag{4.42}$$

where $\sigma_\xi(1)$ and $\sigma_\xi(2)$ are denoted as the variances of the ξ^{th} wavelet coefficient given the hidden Markov state [143] as 1 and 2, respectively. $P_{S_\xi}(y)$ represents the probability of the wavelet coefficient $\widetilde{z}_\xi$ belonging to the hidden state y, $y = 1$ or $y = 2$ in this paper. The minimized formulation can be rewritten further as:

$$L(z) = \alpha \sum_{i=1}^{K} \| \widetilde{g}_i - \widetilde{D}\widetilde{H}_i\widetilde{M}_i z \|^2 + z^T Q z \tag{4.43}$$

where Q is a diagonal matrix ($N^2 \times N^2$) consisting of $q_{(\xi,\xi)}$:

$$q_{(\xi,\xi)} = \frac{1}{2(P_{S_\xi}(1)\sigma_\xi(1)^2 + P_{S_\xi}(2)\sigma_\xi(2)^2)}. \tag{4.44}$$

In Equation (4.43), α is a parameter to describe the variance of the noise as well as the error caused by the incorrect warping and blur matrices (for simplicity, we assume λ_i is the same value for all raw images). α also balances the contribution of the high frequency information from other raw images and the prior model. The estimation of the wavelet coefficients of the original image is found by using the SD (steepest descent) method to minimize Equation (4.43) as

$$z^{r+1} = z^r + ad, \tag{4.45}$$

where d is the descent gradient, r is the r^{th} internal iteration seeking to minimize $L(z)$, and a is the step size. So d is written as:

$$d = -[\alpha \sum_{i=1}^{K} \widetilde{M}_i^T \widetilde{H}_i^T \widetilde{D}^T (\widetilde{D}\widetilde{H}_i\widetilde{M}_i z - \widetilde{g}_i) + Qz], \tag{4.46}$$

and the step size a is given by:

$$a = \frac{d^T d}{d^T(\alpha \sum_{i=1}^{K} \widetilde{M}_i^T \widetilde{H}_i^T \widetilde{D}^T \widetilde{D}\widetilde{H}_i\widetilde{M}_i)d + d^T Q d}. \tag{4.47}$$

Because the prior model is achieved by using the previous pseudo super resolved result, Q needs to be updated $Q^l \rightarrow Q^{l+1}$ using Equation (4.44), where l denotes the l^{th} outer iteration, updating the prior.

The algorithm methods are described well in Li's paper[143]. We adopt this and assign the parameters below to our use.

4.8.2.3 Results

Experimental data is obtained with a portable 0.14 m dia f14 Cassegrain telescope and progressive scan CCD camera. A test scene to be observed is 10km distant and the exposure time is on order of 5ms. The number of image frames is 75. The initial image size is 128×128, and 10 lucky region images are selected (regions with the smaller averaged bicoherence value).

First, some selected superior image regions are listed in Tab.4.2. These lucky regions are used for in subsequent step. In the table, some non-lucky regions and their bicoherence value are also listed (on the right-hand side). One could note that the lucky regions are sharper, have more details even though they might be geometrically warped, and the non-lucky regions are much more severely distorted.

Then super resolution reconstruction is carried out based on the selected regions. We choose the expansion factor, $c = 2$, to achieve an expanded image region with 256x256 pixels. The blur kernel is guessed as Gaussian with size 9×9, and the standard deviation is 2. $\alpha = 0.1$, Daubechies-8 wavelet in the orthogonal wavelet transform is used to fully decompose the images [143]. Moreover, Q is normalized between $[0, 1]$, and all intensities of the images are normalized between $[0, 1]$. Super resolution means that the resulting, enlarged image, contains detail not present by other means, and has been found to occur after 3 outer iterations and 10 internal iterations.

For the sake of comparison, we experimented with another set of images of a same object

Table 4.2: Samples of input and their bicoherence values

lucky regions	mean bicoherence	non-lucky regions	mean bicoherence
	0.3187	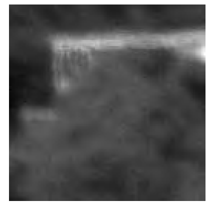	0.4029
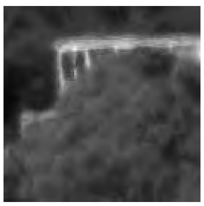	0.3025	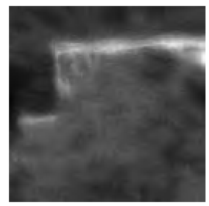	0.4134
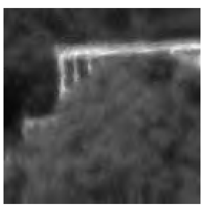	0.3123	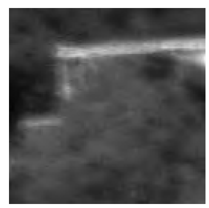	0.3965
	0.2957	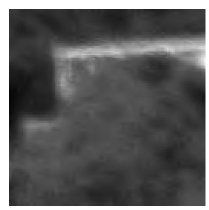	0.4004
	0.3137	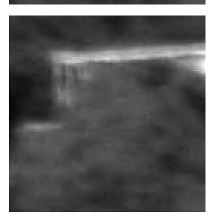	0.3876
	0.3088	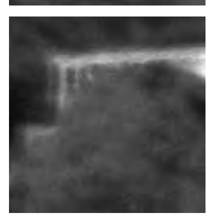	0.3937
	0.2932	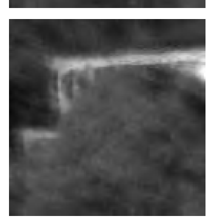	0.4079

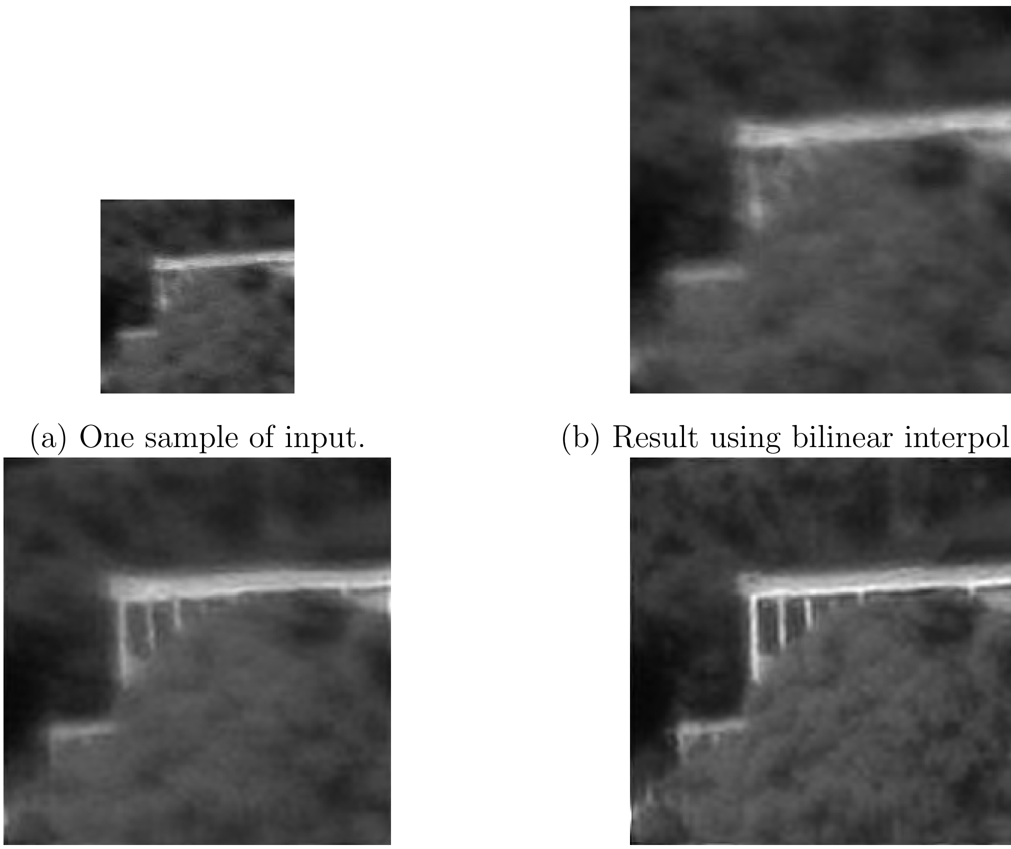

(a) One sample of input.

(b) Result using bilinear interpolation.

(c) Result by randomly selected 10 images.

(d) Result based on lucky regions.

Figure 4.10: Experiment of real data. Result using lucky regions is significantly improved compared to the raw image and the result using randomly selected 10 images. It is more detailed, less blurred and more geometrically correct.

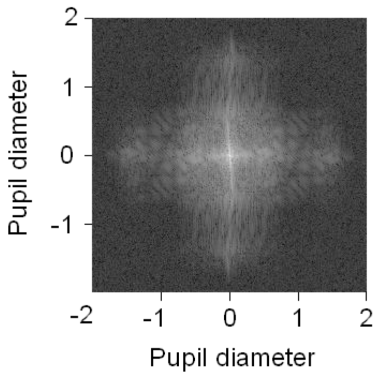

(a).

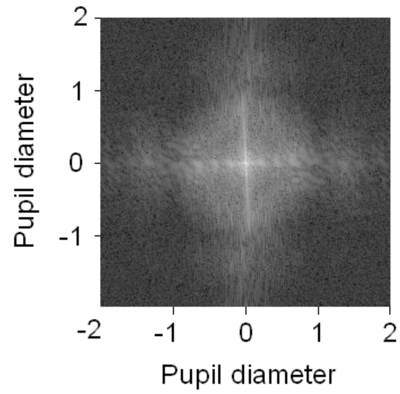

(b)

Figure 4.11: Comparison of power spectrum of results obtained using different images. (a) the power spectrum of the result by randomly selected 10 images, in Fig.4.10 (c); (b) the power spectrum of the result by lucky regions, in Fig.4.10 (d).

which are randomly selected from raw data using the same parameters. Results are shown in Fig.4.10. The result using lucky regions (Fig.4.10 (d)) is significantly improved compared to the raw image and the result by randomly selecting 10 images (Fig.4.10 (c)). The result using lucky regions is more detailed, less blurred and more geometrically correct (see the foliage structure and man-made structure in the results). The log of power spectrum of (c) and (d) are computed and shown in Fig.4.11 (normalised to their DC values). Note that Fig.4.11 (b) contains more high frequency content than Fig.4.11 (a). By selecting the center of the power spectrum and rotating the results in Fig.4.11, degree by degree, then a circular averaged log of power spectrum is computed for each result. A cross section of the averaged log power spectrum (the middle line in this case) is plotted in Fig.4.12. One can see that Fig.4.12 (b) has higher values (especially, in higher frequencies), which means that it includes more high spatial frequency content.

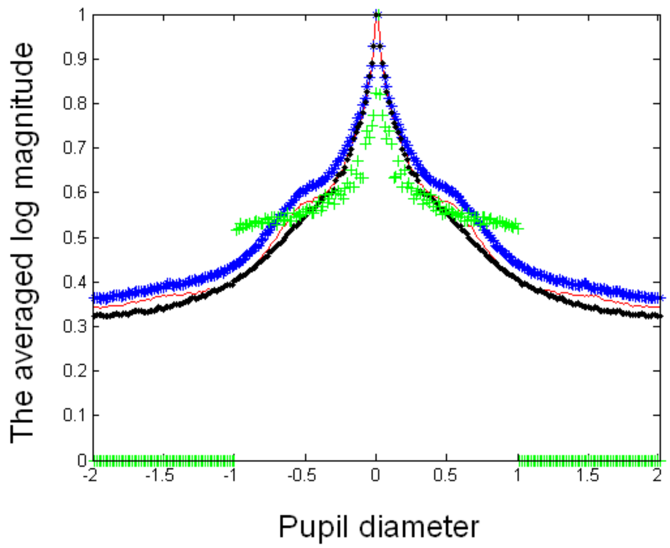

Figure 4.12: Plots of the averaged log power spectrum of images in Fig.4.10 (Normalised to their DC values). The red solid line is calculated with Fig.4.10 (c); and the blur '*' line is with Fig.4.10 (d). Also, the averaged log magnitude of Fig.4.10 (a) is shown, the green '+' line, and Fig.4.10. (b) in black '.' line. Fig.4.10 (d) has higher values in higher frequencies, which means that it includes more high spatial frequency content than Fig.4.10 (c), and both have more high frequency content than the original.

4.9 Summary

In this chapter, a new technique, classed as the lucky region technique is developed. The bicoherence, as a numerical algorithm for lucky region selection is described, and its ability for nonlinearity detection in signals is studied.

Two applications of lucky region technique and the bicoherence as an image measure are given: image restoration and super resolution reconstruction for wide-area/near-to-ground imaging, which demonstrate the robustness of this algorithm and the possibility of extended application in different areas. While presence of higher frequency content by itself cannot indicate good performance, visual inspection of the final results indicates that the information in these frequencies is physically reasonable.

Chapter 5

Imaging Through Turbulent Water Surface

5.1 Introduction

In this chapter, we study the problem of water imaging: image recovery from a set of images distorted by moving water waves. It is common experience that an air-water surface that is in wavy motion distorts images of objects or scenes, depending on whether the object is under the water, and viewed through its wavy surface, or above the water, and viewed by reflection across its wavy surface. In both cases, the object or scene may be distorted geometrically due to the uneven refraction or reflection of the light. Fig.5.1 and 5.2 show examples of each effect.

This chapter addresses the problem of how to suppress or remove the distortions caused by the surface of a body of wavy water, by observing a long sequence of short exposure distorted images[145, 146, 147]. We aim to develop an effective technique to recover the original geometrically-correct result, as if the image was captured with a perfectly still water

Figure 5.1: Samples of water imaging looking down.

Figure 5.2: Samples of water imaging reflection. Note that the images are upside down.

surface. During this process, a new algorithm based on speckle imaging techniques (which combining both the bispectrum technique and the lucky region technique) is proposed.

The bispectrum technique is often used in the astro-photography area for removing atmospheric turbulence effects. We however notice an analogy in the water imaging area. By carefully analyzing the characteristics of water imaging, we derive the condition in which the bispectrum technique can be applied properly. We have implemented and tested the idea on both synthetic and real images, with convincing success. Our approach can be viewed as a novel extension and successful application of the bispectrum technique to water imaging, and represents a practical step forward.

A rippled water surface is not stationary, but wavy and dynamic. If the object or scene to be recovered is pseudo-stationary, and the only dynamics are due to the wavy water surface, then it can be assumed that a time sequence of images is more likely than a single image to result in successful recovery. The proposed technique is therefore based on the analysis of a sequence of the distorted image frames. Moreover, each frame must be captured with a short enough exposure time, so as to freeze the motion of the wavy surface and hence the distortion (this is very similar to speckle imaging in wide-area/near-to-ground imaging). A similar requirement is found in the restoration of atmospherically distorted images in astronomy.

Experiments in both cases, reflection from a wavy water surface and looking through a wavy water surface, show very promising results, which demonstrates that bispectral analysis has great potential in this new application to water image recovery. Some obvious applications include ocean optics (e.g., through-the-water imaging for modern submarines), sea-bed surveys (e.g., the Great Barrier Reef on the coast of Australia) and computer vision (recovering the shape of a distorted deformable object).

5.2 Problem Analysis

To simplify our analysis, we assume that the water body is sufficiently large, and distribution of waves on the water surface are statistically stationary. These assumptions are not restrictive, but rather realistic in practice for relevant applications such as a submarine in a big lake or in the ocean.

We firstly consider the looking-through-the-water-surface case. Suppose a camera is placed *above* the water, looking vertically downward at an object or scene below the water surface. We will consider a true image to be one that is obtained if the water surface is quite flat, and normal to the viewing axis.

Consider any point on the object seen through the moving water surface. If the water surface is flat, even momentarily, the image of this point is in its true position in the camera plane. When a wave passes through the local view point, the water surface becomes slanted (oblique), and the imaged point will change its position due to Snell's law of refraction. In other words, there is a non-zero displacement vector which causes the imaged point to deviate from its true position. However, the displacement vector will return repeatedly to zero as the waves pass through. If the water surface is large, according to the Cox-Munk Law[148], the distribution of the normal of the water surface is approximately Gaussian. The distribution is very much a bell-shaped, zero-centred, unimodal and smooth curve.

Secondly, we consider the alternative scenario where the object or scene is above the water and is viewed obliquely by reflection of optic rays on the rippled surface. In this scenario, the water surface behaves like a mirror with dynamically changing surface shapes.

In this chapter, we study both cases: looking-through-the-water-surface imaging and water-reflection imaging, and solve the image reconstruction problem in each case using the bispectrum technique in much the same way as Chapter 3. In the following subsections, we will describe these two cases in a little more detail.

5.2.1 Case-1: Looking Through the Water Surface

Fig.5.3 demonstrates the refraction law applied to a wavy water surface. Assume that light passes straight up from the planar ground under the water, there will be no refraction for points immediately below if the water surface is still. Under these conditions, the observer will see the object in its true position at b. However, when a wave passes through the imaging path the normal to the water surface N is tilted. This means that the observer will appear to see the object at a instead of at b. When recording through a wavy water surface, an object will appear to be distorted and move around its true position over time. Knowing the surface angles, the refractive index of air and of water, the apparent displacements within an image can be calculated.

These movements are Gaussian distributed centered around the true position in accordance with the Cox-Munk law [148]. The law points out that, given a large surface area and stationary waves, the distribution of the normals of the water surface is approximately Gaussian. Based on the law, Efros et al. have experimentally proved that the image points are distributed approximately as a Gaussian[149]. Therefore the properties of a Gaussian random process can be utilized when processing the images.

5.2.2 Case-2: Water Reflection

Fig.5.4 illustrates the image reconstruction of water reflection imaging. Consider a receiver (for example, a camera) observing a distant source obliquely, where the source is above the water surface such as the calendar in Fig.5.4 (a). The camera records the observations of the reflection of the calendar. When the water is still and the water surface is flat, the

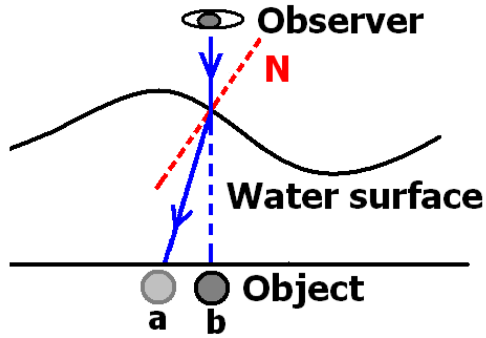

Figure 5.3: Illustration of imaging through the water surface and the refraction law: when the water surface is flat, and perpendicular to line of sight, an observer sees an object in its true position b; when a surface wave exists, due to the effect of refraction, an observer sees the object in position a which can be calculated by Snell's law.

surface is considered as a mirror. Images obtained under these conditions are of the object reflection only, and are considered the true image.

When the water surface is moving, the point b appears to move around its true position. Again, the distribution of the movements is (approximately) Gaussian. The images obtained as shown in Fig.5.4 (c) are upside down due to the mirror effect, besides suffering from distortion due to the effect of the moving water surface.

5.3 Related Works

This section considers some contributions of researchers in various fields and some existed algorithms for water imaging (most for underwater imaging), readers who have more interest in the application of the bispectrum method to this problem may go forward to the next section.

As the distortions in the images are due to the distorted wavefront (of light) caused by the uneven water surface, a natural idea is to use a system to measure and correct the wavefront, as in adaptive optics, or AO[14]. AO is used extensively in astronomical imaging

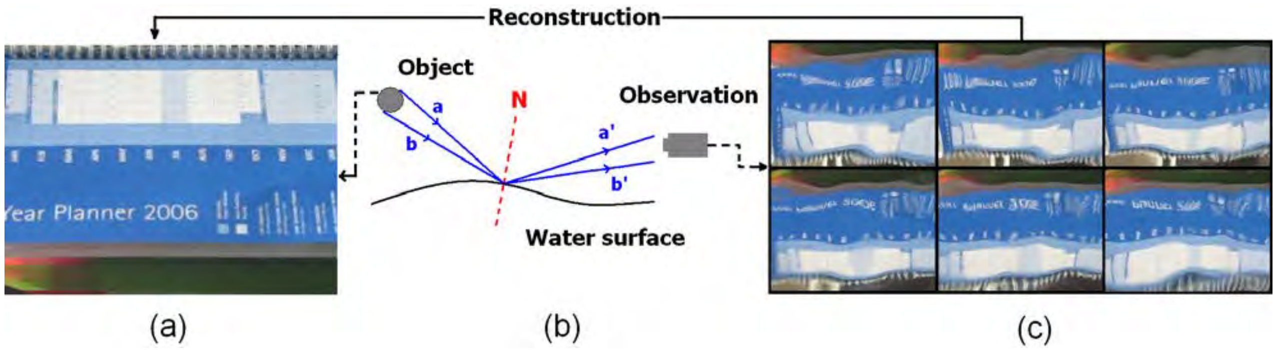

Figure 5.4: The image reconstruction of water reflection. (a) the original object; (b)the geometry for water wave reflection, the temporal distribution of the normal of the surface N is Gaussian; (c) a sample sequence of frames from a video stream. The images are upside down and distorted.

to overcome the effect of the atmospheric turbulence, but has not been widely employed to wide-field imaging. The anisoplanatism of the water surface effects would have similar complexity here as they do with atmospheric turbulence.

Holohan and Dainty discuss the possibility of using AO in through-the-water imaging[150]. The problem is different from the surface distortion we are examining because it covers imaging through water "when it is inhomogeneous due to random temperature and salinity variations" and "when turbulence may be a major factor in loss of resolution of imaging systems"[150]. Images obtained under these conditions suffer low-frequency, low-order aberrations and could be corrected by an AO system. It should be possible to adapt such a system to correct for surface wave distortion, but AO systems are normally very expensive and, to our knowledge, little success was observed for through-the-water imaging using AO.

Shefer et al. [132] describe a simpler approach to reconstruct a submerged object by simply taking the time-average of a large number of continuously distorted video frames. This method, called average based method in this thesis, is based on the assumption that each point in the object viewed through a dynamic water surface moves around a point which is its true position when the water surface is flat and still. This implies that the integral of the movement is zero or close to zero when time tends to infinity. Therefore, the average of the captured images is geometrically correct. However, as it does nothing to recover high frequency information, the reconstructed image is still a low-pass filtered version of the true image and the fine detail is lost.

Researchers from computer vision field, such as Murase, attempt to reconstruct a three-dimensional structure of the water waves using physical characteristics such as optical flow estimation and statistical motion features of the target[151]. This algorithm assumes that the temporal average slant of the water waves surface is zero or close to zero and the distance between the water surface and the object is known a priori. Optical flow and the surface normal of each point are first computed from a sequence of raw images, from which the three-dimensional shape of the water surface is estimated by the surface normal.

Efros et al. recently proposed a graph-embedding technique (used in the machine learning area) to recover an underwater image[149]. Their method, though, was motivated from very different perspectives, in spirit similar to the lucky imaging technique that we are also going to use in this chapter. Their method points out that when observing for a long time and considering a particular point in an object, one can find that the point is exactly in its correct position whenever the water surface imaging that point happens to be locally flat. A shortest path algorithm is used to select the image having the shortest overall path to all the other images. The local distance is computed transitively by normalized cross correlation (NCC).

Donate et al. introduce a similar but more robust approach to form an estimate of the target by finding local regions that best present a true view of the region being analyzed [152, 153]. This method attempts to separate image blocks into high and low distortion groups (corresponding to the movements with high and low energy) using the K-means algorithm. Then NCC is used to select an image region which is closest to all other regions.

These two methods produce much sharper and more detailed images of the target than does the average based method [107].

Some researchers focus on the estimation of the water surface as well as the image reconstruction of the object. For example, Milder et al. use such a technique to recover the above-water-surface scene. The radial slope along extinction boundaries is measured and recursively improved by minimizing the quadratic measurement error to estimate the water surface [154]. Then inverse-ray-tracing is used to reconstruct the target image from the water surface estimation based on a refraction law.

This thesis presents a new algorithm to estimate the real image distorted by moving water waves. It works equally well for both problems of through-the-water-surface imaging and water-reflection imaging. The reconstruction problem of water imaging is regarded as a "phase tracking" task, in which a lucky region selection followed by bispectral analysis is employed to recover an undistorted image.

5.4 The Proposed Algorithm

This section describes step by step our algorithm which inputs a water-distorted video sequence and outputs a single geometrically-correct, superior image.

Consider observing a particular point imaged through a water surface under wave conditions. Most of the time, the point is scaled or distorted, or moves away from its geometrically correct position as the waves pass through. This results in a randomly distorted and spread image at that spatial location.

However, at some moments, the effect of the water surface turbulence may be slight or even negligible, and a snapshot of that region at that instant approaches its ground truth. If we can recognize when this occurs and select such regions from a sequence of video frames, then use these less distorted observations in subsequent post-processing, we can improve the final image reconstruction. This preprocess step constitutes lucky region selection, which is discussed in Chapter 4.

The following sketches our algorithm, which consists of four major steps:

1. Preprocessing. Divide each of the input raw images into M small image patches or regions of equal size; each patch overlaps its four neighbouring patches. In other words, the original frame sequence are divided into M subsequences of image regions.

2. Lucky region selection step. Detect the quality of each region in each subsequence based on an image quality measurement, and discard any severely distorted image patches from the region series.

3. Image recovery using bispectral analysis. Apply bispectrum-based speckle imaging technique to the lucky regions and estimate a single region in each image region subsequence. M single and separate image regions will be obtained in total.

4. Image fusion. Put the recovered image region together to form an overlapping mosaic to reconstruct and output an undistorted image.

The techniques used above has been explained in previous chapters: Segmentation and the lucky region technique in Chapter 4 and the bispectral analysis in Chapter 3. Here, in the step of lucky region selection, we developed another image quality measure besides the bicoherence method.

This method is derived from the image quality index proposed by Wang[117], which has been discussed in the previous section. The advantage of this method is its short computation time, which is shorter than the method based on bicoherence. The disadvantage is that a true image is needed. This is impractical when the true image is always unknown in real world applications.

For convenience, we rewrite the metric here[117]:

$$M = \frac{4\sigma_{i_c i_t}\overline{i_c}\ \overline{i_t}}{(\sigma^2_{i_c i_c} + \sigma^2_{i_t i_t})[(\overline{i_c})^2 + (\overline{i_t})^2]} \tag{5.1}$$

where i_c is the clean image and i_t is the test image, $\overline{i_c}$ and $\sigma^2_{i_c i_c}$, and $\overline{i_t}$ and $\sigma^2_{i_t i_t}$ are the expectation and the variance of i_c and i_t, respectively, $\sigma_{i_c i_t}$ is the covariance of i_c and i_t. The value of M lies on $[-1, 1]$, when $i_c = i_t$ or i_t is close to i_c, M gains the best value 1. M tends to -1 when i_t is very different with i_c.

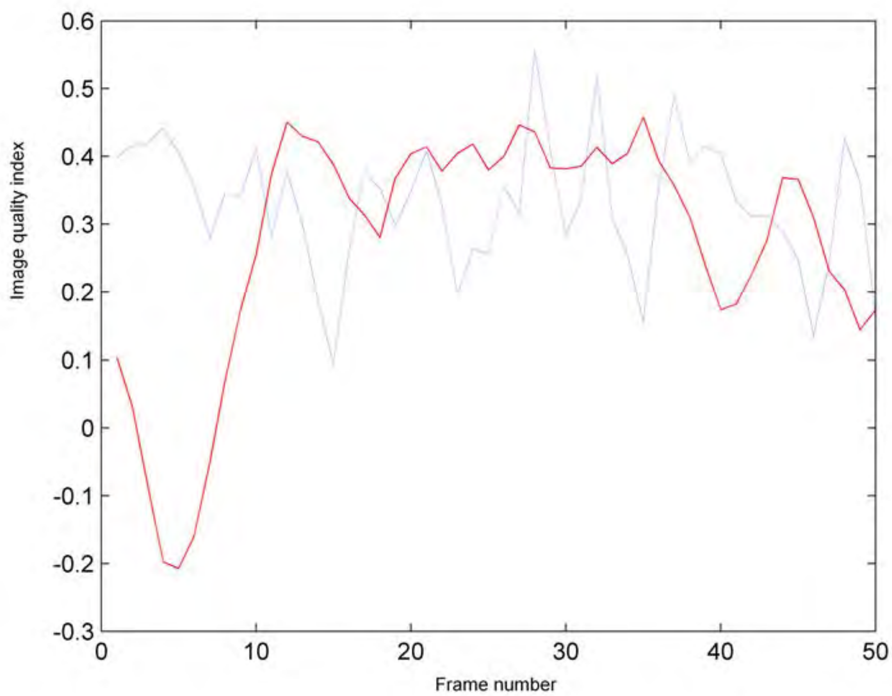

Figure 5.5: Comparison between the bicoherence method and Wang's method. The curves show the consistency between the two methods, while the dashed blue line represents the value of the bicoherence of 50 images, the red line sketches the value calculated by Wang's method. Note that when the red line goes up to a peak the blue line always goes down to a local minimum.

Note that, in the problem discussed in here, the clean image is unknown and is what we are trying to find. However, we have a sequence of raw images. In [11], Fraser et al.

assumed that the temporal mean of a full set of affected images is geometrically correct, although it may be uniformly blurred. In our algorithm, we substitute the mean image for i_c.

Both the bicoherence method and Wang's method work well in this context. Fig.5.5 shows the consistency between the two methods, while the dashed blue line representing the value of the bicoherence of 50 images the red line sketches the value calculated by Wang's method. Note that when the red line goes up to a peak the blue line always goes down to a local minimum.

The difference between the two methods is that the the bicoherence method detects the degree of nonlinearity of a signal, so that the smaller the value, the better the image quality; the Wang's method is to detect the likelihood between the tested image and the true image, so that the higher the value, the better the image quality. Readers may choose other methods to suit their cases when applying this technique, if necessary.

5.5 Experiments

The performance of our method is tested against both simulated and natural data, which will be explained in the following subsections.

5.5.1 Simulated Data

To facilitate our experiments, we first generate some simulated water wave distorted image sequences. The distortion is made so as to perfectly satisfy the above Gaussian distribution. This purpose is mainly to validate our algorithm to be described later.

In this section, we briefly introduce the model originally proposed by Murase [151] to simulate water waves. This model assumes that the object or scene to be viewed in the water is static and flat, and that the average slant of the moving water surface at any point is zero when observed for a very long time. These assumptions fit our problem.

According to Murase's model, the displacement at each point in the image away from its true position (due to the moving wave) is given by

$$\begin{cases} d_x &= hp(1-1/n)+N \\ d_y &= hq(1-1/n)+N \end{cases} \tag{5.2}$$

where h is the distance between the water surface and the planar object of interest under the water, n is the refractive index of water which is 1.33, and N is white Gaussian noise. The variables p and q are the superposed patterns of two water waves having different speeds and lengths, which can be expressed by the wave number u_i and v_i, the angular frequency w_i and the amplitude a_i as follows:

$$\begin{cases} p &= -\sum a_i u_i cos(u_i x + v_i y - w_i t) \\ q &= -\sum a_i v_i cos(u_i x + v_i y - w_i t) \end{cases} \tag{5.3}$$

By adjusting h, u_i and v_i, we can obtain different types of waves and therefore simulate smooth and deep water waves.

Using Eq.5.2 we produced two sequences of short exposure images. In the first sequence, a text plate is used as the ground truth image and a set of 100 images is generated with parameters $\langle a = 8, h = 5\rangle$ and the number of waves across the image is 5. The size of each image tile is 32×32 with 50% overlap. The threshold of lucky images is 20% using the bicoherence method. Fig.5.6 shows the result of our algorithm. Also, one sample of the distorted images, the true image and the result from the average-based method (simply averaging the set of short exposure images) are shown. The estimate by our algorithm

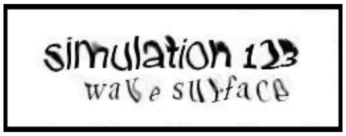

(a) one sample image

(b) result by average based method

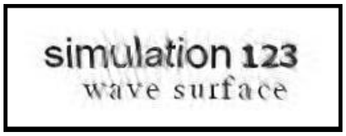

(c) result by our algorithm

(d) the ground truth image

Figure 5.6: Simulation results. The result in (c) is produced by our algorithm using the bicoherence for lucky region selection and the bispectrum for image restoration.

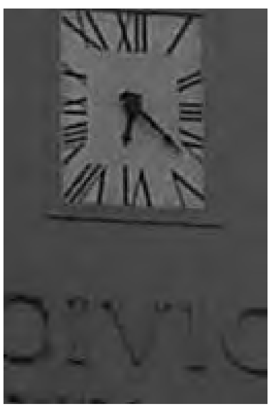

(a) the ground truth image

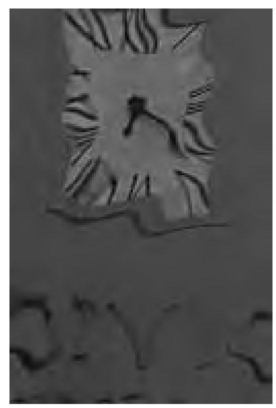

(b) one sample image

(c) result by our algorithm

(d) result by average based method

Figure 5.7: Simulation results. The result in (c) is produced by our algorithm using Wang's method for lucky region selection and the bispectrum for image restoration.

(a) the ground truth image

(b) one sample image

(c) result by our algorithm

(d) result by average based method

Figure 5.8: Simulation results. The result in (c) is produced by our algorithm using the bicoherence method for lucky region selection and the bispectrum for image restoration.

using the bicoherence for selection of lucky regions and the bispectrum for restoration is much sharper, and the text on the image is easily recognized.

We also produced two simulated sequences using a clock image and a chair image as ground truth image, respectively. For the clock image, we have the parameter settings as: 500 short exposure images are generated, the number of waves is 3, and $\langle a = 10, h = 4\rangle$. For the chair case, 300 images are produced with wave number being 4, and $\langle a = 12, h = 7\rangle$. The size of each image tile is 64×64 with 50% overlap. The rate of lucky image is 20%. Results are shown in Fig.5.7 and 5.8 which demonstrate that our algorithm works for different conditions of water surface.

Note that we apply bicoherence to select lucky regions and then produce the result in Fig.5.8 (c), and the Wang's method is used in Fig.5.7 (c). Both methods work well with our data. The bicoherence tends to choose those regions containing correct phase information

(a) one sample image (b) by average based method (c) by our algorithm

Figure 5.9: Results of image reconstruction for through-the-water imaging.

and Wang's method prefers regions having maximum likelihood with the reference image region.

5.5.2 Natural Image Data

In experiments with an actual wavy water surface, image sequences are captured by video camera fixed above the surface. Waves are generated by wind produced by a fan, while an object is dropped into the water to create additional waves. The water is clear and no account has been taken of any attenuation by a turbid medium.

Looking-through-the-water-surface imaging: For this experiment, a still object is laid on the planar ground under the water. The size of each image in the stream is 256×192. In total 120 images are used and the size of image tiles is 64×64. Fig.5.9 compares our result with one of the raw images and with a result from the average-based method. Note that the R, G, and B channels in the colour image are processed separately and are combined to reproduce a colour image.

Water-reflection imaging: An object is viewed by reflection over the water surface. A video camera faces the water surface to capture upside down images of the object. In this experiment, we captured two sets of data under different conditions. In one case, the waves are quite strong, while in the other case, the waves are relatively smooth. We tested

(a) one sample image

(b) by average based method

(c) by our algorithm

(d) one sample image

(e) by average based method

(f) by our algorithm

Figure 5.10: Results of water-reflection image recovery. ***(a)-(c)*** under rough conditions; ***(d)-(f)*** under mild conditions.

both cases with our algorithm, and our results are much better than those estimated by the average based method. Fig.5.10 shows the results. The upper row are the images under the rough conditions and the lower row are for mild conditions.

5.6 Discussion

The implementation of our algorithm is in MATLAB. The code does not have any particular optimization. It runs on a personal computer with $3.20GHz$ and $1GB$ of RAM. The computation time is about 25 minutes for a sequence of 100 frames with size of 256×256, the size of each image region is 64×64 and the rate of lucky region is 20%. The calculation of the estimated phases takes the most time of the computation. The computation time will also increases significantly when the size of the image blocks increases. The speed can be improved by optimizing the code with $C/C++$, or by using hardware such as a GPU.

The size of the image regions should be manually set before running the algorithm. From our experiment results, we found that the region size is associated with wave length,

(a) Region size is 32x32 (b) Region size is 64x64

Figure 5.11: Comparison of different results using different regions size. (a) Region size is 32x32; (b) Region size is 64x64. From vision inspection, result in (b) is better, clearer, and sharper.

similar in concept to the isoplanatic patch in imaging through the atmosphere; the closer to wave length the region size, the better the estimate of the object. Both simulation and real world data demonstrates the fact.

In the first experiment with simulated data, the image size is 128x64 pixels. Different region sizes (64×64, 32×32, and 16×16) are tested, and the best result is obtained with 32×32 region size. This data is close to the wave length which is 25.6 pixels (the number of simulated waves is 5 in x direction).

For the natural case of looking through water surface, 64×64 is the best choice. Fig.5.11 shows two results from regions with 64×64 and 32×32 pixels, respectively. From vision inspection, the result using 64×64 is clearer, sharper, and contains finer details of the object. This is reasonable because the data is taken under very smoothly moving water surface, therefore the wave length should be relatively large compared to the the size of the entire image, and 32×32 may lead to a worse result.

The performance of our algorithm is inspected with numerical measurements, here, we choose the bicoherence method and Wang's method. Both methods calculate a numerical value, which is used to predict the quality of the restored image. When using the bicoherence method, the lower the value, the better the image. On the contrary, in the case of Wang's method, the higher the value the better the image.

Table 5.1: Comparison between our method and Wang's method with natural data. **R** denotes the result by our method, and **S** represents one of the raw image. The numerical values show the image quality results for the images in the first column. When using Wang's method, the result by the average based method is used as a reference image. No reference image is needed with the bicoherence method.

Image	the bicoherence method (low values – good)	Wang's method (high values – good)
R 	0.0067	0.9696
S 	0.0098	0.8936
R 	0.0131	0.7843
S 	0.0230	0.4401

Table 5.2: Comparison between our method and Wang's method with simulated data. **T** means the ground truth image, **R** denotes the result by our method, and **A** is the result by the average-based method. The numerical values show the image quality results for the images in the first column. In this case, when using Wang's method, the true image is a reference image. Again, no reference image is needed with the bicoherence method. As expected, the true image has the lowest bicoherence and the result by our algorithm is superior than that by the average-based method.

Image	the bicoherence method (low values – good)	Wang's method (high values – good)
T 	0.0033	1
R 	0.0054	0.8352
A 	0.0060	0.8794
T 	0.0038	1
R 	0.0041	0.9282
A 	0.0044	0.9492

The results are listed in Tab.5.1 and 5.2, respectively. Tab.5.1 is with natural data. It compares the quality of the result by our algorithm with one of the recorded images in both cases we have studied, which is to show how our algorithm improves the image quality. As expected, the results produced by our algorithm have lower value with the bicoherence method and higher value with Wang's method. Note that, when applying Wang's method with natural data, the result by the average-based method (temporally averaging a sequence of images) is used as a reference image.

The second comparison is in Tab.5.2, which aims to compare the result by our algorithm with the result by the average based method and the true image. In this case, the ground truth image is known, so that it is used as a reference image when using Wang's method and has the highest value 1. Wang's method shows that the result by the average based method has a higher value while the bicoherence method has a low result.

This comparison has another meaning: it verifies that our method (i.e., the bicoherence method) for lucky region selection is effective. As expected, the true image has the lowest value and the result by our algorithm is superior to that by the average based method.

5.7 Summary

This chapter studies two problems of water imaging, both involving a disturbed, time-varying (wavy) water surface. On the one hand, imaging occurs through the air-water surface, involving refraction effects at the surface. In the other case, image formation is by reflection of an object or scene across the water surface.

A novel and original attempt have been taken to recover an image of the target with a sequence of images in both cases which should also extend to imaging from under-water to observe objects above the water surface. Taking the similarity of water imaging and astronomical imaging into account, two techniques originally introduced in astronomical imaging, the lucky region technique (the extension of the lucky imaging to lucky region), and the bispectrum technique (for image recovery), have been combined to form a new algorithm to solve the water imaging problem.

This technique performs very well in both the simulated and real-world experiments. It also can be potentially applied to other imaging situations having similar distortions to those of imaging through atmospheric turbulence[107].

Chapter 6

Image Restoration using Sparsity

6.1 Introduction

In previous chapters we have studied the theory and methods for removing (or reducing) image degradations and distortion caused by turbulent media. The central method we have investigated is the one based on bispectrum speckle processing.

Roughly speaking, this bispectrum method basically performs some sort of "temporal averaging" operation, in the sense that local spatially variant geometric distortions are corrected by "averaging out" random distortions across time. This essentially amount to removing the random phase abberations caused by random atmospheric turbulence.

However, phase distortion is only one side of the story. During this course of bispectrum-based speckle processing, there are also magnitude distortions besides the phase ones. More specifically, when applying the bispectrum technique (in order to remove phase distortion), Fourier modulus methods such as the averaged power spectrum are employed (for example, the method developed in Chapter 3) which inevitably add some "smoothing" (i.e., out-of-focus type) effect to the resultant image. Such a *smoothed* image is in fact a low-pass filtered (LPF) version of the true clear image. Furthermore, it is not hard to see that, the LPF is of zero-phase (i.e., no phase distortion) and homogeneous (i.e. spatial invariant), because the output after the bispectrum processing stage is a single geometrically correct image[11].

This chapter is concerned with how to further remove the residual blur introduced by the unknown LPF, and to correctly boost high frequency content to obtain a better version of the true image. This is a typical "blind deconvolution" problem. It is worth noting that, the reason that classical blind deconvolution technique can be employed in wide-area turbulent imaging is that the remaining PSF of the LPF has been made position-invariant thank to our speckle preprocessing or other turbulence removal techniques [12].

Yet another novelty of the work in this chapter is that, for the first time, we introduce the use of natural image prior to the problem of image restoration in the context of imaging through turbulence. This can be viewed as a general principle and strategy to improve the performance of general turbulent image restoration algorithms (see Fig.6.1).

Most other algorithms often stop after removing the phase distortion caused by turbulent media. In contrast, our strategy is to do one step further, and solves a classical single-frame image restoration problem, by taking into account the universal and inherent characteristic (i.e., statistical priors) of real-world natural scenes (and of the unknown blur kernel–the LPF) [155, 156].

6.2 Priors for the Unknown Blur Kernel

The geometrically correct image after the bispectrum processing has a spatial-invariant but unknown blur. Magnitude information is lost due to the "temporal averaging" effect of this blur kernel. One could then recover a non-blurred version by using any "totally-blind"

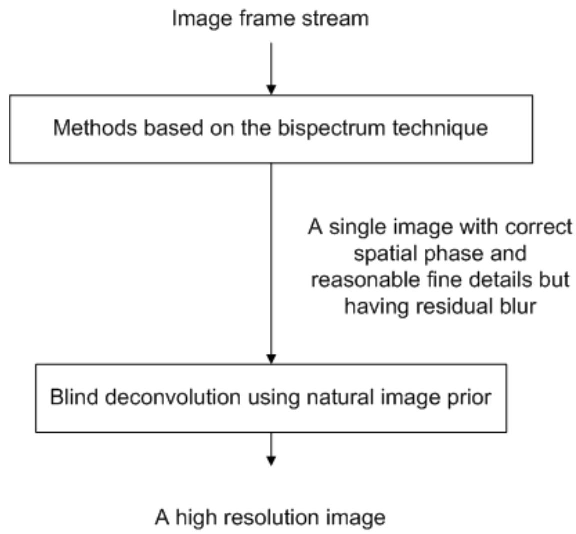

Figure 6.1: A simple illustration of our new strategy to improve the quality of images taken through atmospheric turbulence.

blind-deconvolution algorithms such as the blind - Lucy-Richardson method. However, a better way is to examine if there is any prior information about the blur kernel that can be utilized to better regularize the otherwise ill-posed blind deconvolution problem; this is the main idea of our work.

Fortunately, for our particular problem of "imaging through turbulence" using bipsectrum processing, we do have found that there are some available special structures that can be taken advantage of. Let us now explain this.

After the phase recovery stage by the bispectrum technique, we can assume that the obtained blurred image suffers from no geometric distortion at all. In other words, the unknown blur kernel must be spatially homogenous, small in size (relative to the size of original image) and have zero phase-shift. Moreover, when the sequence is long enough, we can safely assume that the effective blur kernel is in fact isotropic (i.e., circularly symmetric). All these reasonable assumptions will be used to reduce the otherwise huge search space during the blind deconvolution computation.

We also have other two trivial priors on the blur kernel, which are: (1) non-negative and (2) sum to one. These will help the computational procedure as well.

6.3 Priors of Natural Images

Besides these priors for the blur kernel, in this thesis, we also emphasize the use of a different type of prior, the natural image prior of the target image to be recovered.

One main theme of the thesis is to apply turbulent imaging restoration technique, traditionally aimed at astronomical image processing, to wide-area/near-go-ground (or underwater) target observation. In contrast to astronomical observation where the target image is often tiny or possibly multiple point sources, in our case the target is often extended, and of considerable size. Moreover , it is often a natural scene. For example, in the long-range surveillance application, the objects of interest are often buildings, trees, humans or vehicles etc.

This prior knowledge of the target suggests that: if a blind deconvolution algorithm could somehow expliot/utilize such specialities, then the restored target will have a conceivably better result. This is the main point of this chapter.

There is a vast literature on the topic of blind deconvolution. To give a general treatment of this long-standing topic is out of the scope of the thesis. Instead, we only give some basic experimental investigation, and the main purpose is to demonstrate the usefulness of the concept of applying a natural image prior to the particular application of turbulent image processing. We show this by some preliminary experiments.

6.4 Natural Image Prior

Natural images are often sparse. This is one of the most prominent priors that possess by natural images. To make this point clear, we will begin with some formal definition and discussion of sparse signal.

6.4.1 Sparse Signal

Suppose a vector $\mathbf{v} \in R^N$, is said to be *sparse* if $\mathbf{v} = \{v_1, \cdots, v_n\}$ satisfies

$$v_i \neq 0, \text{for } i \in M, M \ll N \tag{6.1}$$

$\mathbf{v}$ is also called an M-sparse vector. This definition can be directly extended to a two-dimensional discrete signal, for example, an image $i(x_i, y_j) \in R^2(i = \{1, \cdots, M\}, j = \{1, \cdots, N\})$. $i(x, y)$ is sparse if

$$i(x_i, y_j) \neq 0, \text{for } i \in K, K \ll M, \text{and } j \in L, L \ll N \tag{6.2}$$

This implies that most pixels of $i(x, y)$ are zero or close to zero such that only a few have relatively impressive spikes.

6.4.2 Direct Sparse Natural Images

Direct-sparse images (which means most pixels of the image take values of zero) can be found in some special occasions. For example, the astronomical images which record the observations of stars and galaxies. The background of such types of images is considered as black (or set to be zero), and the non-zero pixels (high lights) correspond to the stars or galaxies. Fig.6.2 (downloaded from `http://www.buytelescopes.com/viewphoto.aspx?pid=17570\&p=11273`) is a galaxies picture captured by a STL-11000M Class 2 CCD camera. It exhibits only a small number of bright stars (impulses) compared to the entire size of the image.

Figure 6.2: A galaxies picture of which the background is black with a small amount of impulses compared to the size of the image.

6.4.3 Gradient-sparse Natural Images

Apparently, most natural images (images of real-world scenes and objects) seem to be not sparse. However, by taking the derivatives (gradient) and studying the statistics of natural scene images, researchers have found that the gradients of most real world images are sparse or "heavy tailed", even though the images are not sparse. This can be understood by that, except at edges of objects, this type of images has very smooth color changes in most areas which leads to zero or close to zero gradient values in these areas. This results in the sparsity of the image gradients.

Tab.6.1 lists some natural images and the logarithm of the distribution of their derivatives in the x and y directions. The curves drop smoothly from zero gradient forming a heavy tailed distribution that indicates that the values of the gradients are zero or close to zero outside a band limit.

In this context, the image gradient favors the definition of sparse signal. Theories of sparse signal (e.g. compressed sensing theory) and techniques of sparse signal recovery may be applied to our problem, where the objects are natural, and extended.

6.4.4 Statistical Model

In blind deconvolution, the task of finding the potential image, o, is usually formulated by researchers to be a minimization problem using a Bayesian framework: Given the observed blurred image i, find the most likely estimate of the potential sharp image o and the blur kernel h.

Again, the simple model of the imaging system is employed:

$$i = o * h + n, \tag{6.3}$$

where i is the recorded image, o is the true image, h is the PSF, $*$ is the convolution operator, and $n \sim \aleph(0, \sigma^2)$ is a term used to account for various forms of additive noise.

A simple approach to this problem is to use MAP (*maximum a posteriori*) estimation to seek a pair (o, h) to maximizing

$$p(o, h|i) = \frac{p(i|o, h)p(o)p(h)}{p(i)} \tag{6.4}$$

Table 6.1: Sparsity of gradient of natural images.

Natural image	Gradients density in x	Gradients density in y
	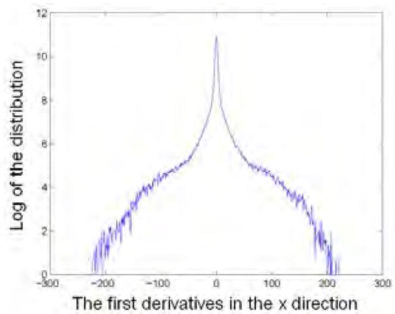	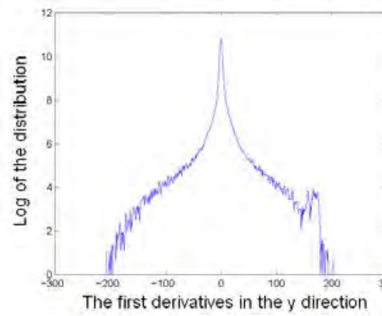
	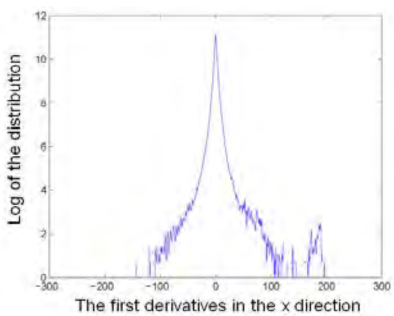	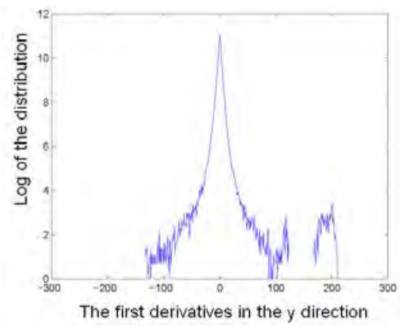
	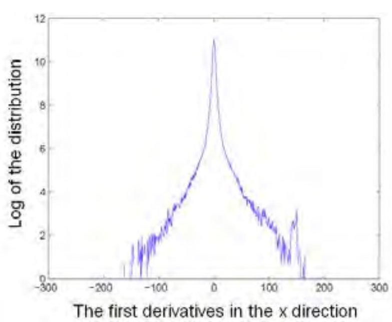	
	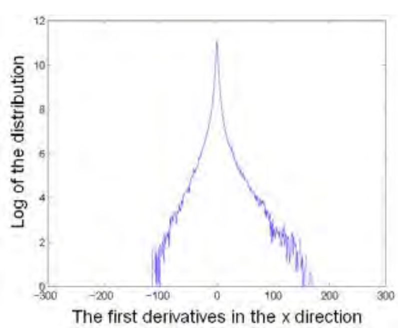	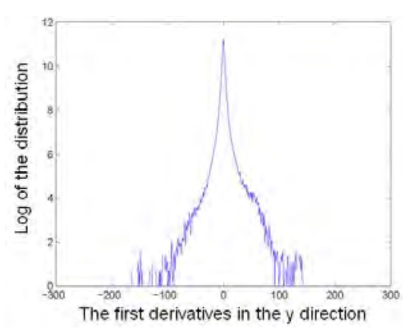

where $p(\cdot)$ is the probability distribution. Take away $p(i)$ from the equation ($p(i)$ is constant) and take the negative log likelihood, the problem is then recast to defining and minimizing the likelihood terms in the following:

$$arg\max_{o,h} p(o,h|i) = arg\min_{o,h}\{L(i|o,h) + L(o) + L(h)\} \tag{6.5}$$

where $L(\cdot) = -log(\cdot)$, is the negative log likelihood term. Based on Eq.6.3, the data fitting term is

$$L(i|o,h) = \lambda|o \otimes h|^2 \tag{6.6}$$

where $\lambda = 1/\sigma^2$.

$L(o)$ depends on the image prior, which is to determine a best fitting result from the infinite resolution pairs (o,h) (to Eq.6.3). A common measure of $L(o)$ is the prior on image gradients

$$L(o) = \lambda|\nabla o|^{\alpha} \tag{6.7}$$

where ∇o indicates the spatial gradients of image o, and α is a regularization parameter. The value of α states the assumption on the sharp image is smooth or not, for example, a Gaussian prior $\alpha = 2$ means that the image is smooth or piecewise smooth, and λ controls the weight of the smoothness penalty. Another choice is a Laplacian prior $\alpha = 1$.

While most natural image gradients are non-Gaussian, some researchers [76, 85, 86, 90, 93, 94] try a hyper-Laplacian distribution on image gradients with $\alpha < 1$. This prior favors natural images with gradients being sparse or heavily-tailed and zero-peaked. Motivated by their results, we study, in this chapter, the problem of how to obtain a high resolution result by making special use of the sparsity of natural images.

6.5 An Overview of Compressed Sensing Theory

Compressed Sensing is a new signal processing topic that exploits the sparsity of coefficients of natural signals for the solution of under-determined inverse problems. It provides an alternative to the Nyquist-Shannon sampling theory. The Nyquist theory states that "an analogue signal that has been sampled can be perfectly reconstructed from the samples if the sampling rate exceeds $2B$ samples per second, where B is the highest frequency in the original signal"[157].

Compressed sensing theory states that a signal can be recovered from highly incomplete information, in the case that the signal is sparse. It is "a technique for acquiring and reconstructing a signal utilizing the prior knowledge that it is sparse or compressible" [158].

If $\mathbf{s} \in R^N$ is a sparse vector (i.e., only some entries of $\mathbf{s}$ are nonzero), to recover $\mathbf{s}$ from a small number of measurements, $\mathbf{c}$ (for now, assume that no noise is added to the measurements),

$$\mathbf{c} = \mathbf{A}\mathbf{s} \in R^M, M \ll N \tag{6.8}$$

where $\mathbf{A}$ is a matrix representing the sensing mechanism. one would be required to solve

$$\min ||\mathbf{s}||_{\ell_0} \text{ subject to } \mathbf{A}\mathbf{s} = \mathbf{c} \tag{6.9}$$

where ℓ_0 indicates the ℓ_0-norm of $\mathbf{s}$, which is the support of $\mathbf{s}$ or the number of nonzero terms in $\mathbf{s}$. This is a combinatorial optimization problem and is known to be NP-complete. However, it has been shown in [159, 160, 161, 162] that under certain conditions, the solution to this problem is the same as the solution to the corresponding ℓ_1 minimization problem:

$$\min ||\mathbf{s}||_{\ell_1} \text{ subject to } \mathbf{As} = \mathbf{c} \tag{6.10}$$

where $||\mathbf{s}||_{\ell_1} = \sum_1^K |s_i|$ is the ℓ_1-norm of $\mathbf{s}$.

This is a convex optimization problem that can be solved (rather) efficiently by *linear programming* (LP). For example, interior point methods can solve an LP in polynomial time.

In practice, most real-world signals are often corrupted by some sort of noise. According to the definition of sparse signal, the measurements then become

$$\mathbf{c} = \mathbf{As} \in R^K + n, K \ll N \tag{6.11}$$

where n is the noise, for most occasions, it is a white Gaussian noise with variance σ^2. A similar result for this noisy case is given[163]:

$$\min ||\mathbf{s}||_{\ell_1} \text{ subject to } ||\mathbf{As} - \mathbf{c}||_{\ell_2} \leq \eta \tag{6.12}$$

where η is an upper bound of $||n||_{\ell_2}$.

If the signal $\mathbf{s}$ is two-dimensional and discrete (for example, an image), an alternative recovery model is that the gradient is sparse. In this case, the total variation (TV) of the signal is used for image recovery.

$$\min TV(\mathbf{s}) \text{ subject to } ||\mathbf{As} - \mathbf{c}||_{\ell_2} \leq \eta \tag{6.13}$$

Here the TV of $\mathbf{s}$ is defined as the sum of the magnitude of the gradient at each point.

In this thesis, we use the results of compressed sensing to develop a novel algorithm for image blind deconvolution. To solve the optimization problem in Eqs.6.10 and 6.12, a lot of optimization techniques have been proposed. Here, the MATLAB code of ℓ_1-magic is used[161].

6.6 Solve for (o, h)

As we discussed in previous sections, the first derivative of a real-world image, ∇o, is sparse. Based on the compressed sensing theory, in the absence of noise, ∇o can be exactly recovered from a small number of linear measurements given that the linear transform matrix is known. This section investigates how to make use of the ℓ_1-norm minimization for the recovery of ∇o with the unknown h. Also, for the completeness of the algorithm, a Poisson image reconstruction method presented in [164, 165] is described to estimate an image from its gradient image.

6.6.1 Deduction

Our algorithm begins from the definition of an image gradient and its basic property. Given an image $i(x, y)$, its derivative is defined by

$$\nabla i = \begin{pmatrix} \nabla i_x \\ \nabla i_y \end{pmatrix} = \begin{pmatrix} \frac{\partial i(x,y)}{\partial x} \\ \frac{\partial i(x,y)}{\partial y} \end{pmatrix} \tag{6.14}$$

where ∇i denotes the gradient of image i, ∇i_x and ∇i_y represent the gradient on x and y directions, respectively. For a particular pixel in a discrete image, the approximation of the derivative can be simply calculated by the filters: $\begin{bmatrix} -1 & 1 \end{bmatrix}$ for x direction and $\begin{bmatrix} -1 & 1 \end{bmatrix}^T$ for y direction. Let g denote $\begin{bmatrix} -1 & 1 \end{bmatrix}$, we have another expression for the derivatives using convolution operator

$$\begin{aligned} \nabla i_x &= i * g \\ \nabla i_y &= i * g^T \end{aligned} \tag{6.15}$$

According to Eqs.6.3 and 6.15, ∇_i then is expressed as

$$\begin{aligned} \nabla i_x &= i * g \\ &= o * h * g \\ &= o * g * h \\ &= \nabla o_x * h \end{aligned} \tag{6.16}$$

and

$$\nabla i_y = o * g^T * h = \nabla o_y * h \tag{6.17}$$

In other words, $\nabla i = \nabla o * h$. This two-dimensional convolution operation can be transformed to matrix-vector form such as the form $\mathbf{c} = \mathbf{As}$ (please refer to Section 6.7). As discussed, natural image gradient is sparse distributed, so that ∇o can be exactly recovered from its measurements ∇i according to compressed sensing theory, if h is known.

In fact, we know nothing about the PSF, h, except for some simple prior and assumptions. Here, we suppose that the kernel h also has sparse density, which means that the gradient of h, ∇h has zero values in most supporting area and only have massive values in the rest. In the same way as deducing ∇o, we have $\nabla i = o * \nabla h$. Again, ∇h can be exactly recovered from ∇i if o is known.

6.6.2 The Algorithm

In this subsection, we sketch out our algorithm for the removal of the remaining blur in the image. This method includes two important steps which are performed iteratively until a reasonable result is obtained: given ∇i and an estimate of h, calculate an estimate of ∇o; given ∇i and an estimate of o, calculate an estimate of ∇h. In the first step, the ℓ_1-norm minimization is used for image recovery, and in the second step, the TV minimization is applied.

Tab.6.2 is the sketch of our algorithm. Note that an estimate of the true image or the PSF should be made before running the algorithm. A nil initiation will not hurt the algorithm, but a useful estimate will speed up the convergence of the minimization. When the estimate gradient of the true image or the PSF is obtained, a reverse processing should be applied to the gradients to recover the signals (i.e., o and h), so that they can be used in the following iteration. This reverse processing is via Poisson image reconstruction method, which will be described in the next subsection.

6.6.3 From Gradients to Image

In our algorithm, we use the method based on *Poisson image reconstruction* algorithm presented in [164, 165] to form the density image after the estimate image gradient is calculated. For the completeness of this thesis, we give a brief description of this method.

Let g denote the intensity image reconstructed from ∇o, a direct method is to minimize $||\nabla g - \nabla o||$, so that $\nabla o \approx \nabla g$ [166]. By introducing a Laplacian and a divergence operator, g can be obtained by solving the Poisson differential equation[167, 168].

$$\nabla^2 g = \nabla(\nabla o) \tag{6.20}$$

Table 6.2: The sketch of the new algorithm.

1. Compute ∇i; set $k = 0$, the number of iterations k_{max}, and the initial estimation of $o_{k=0}$; set ϵ and η
2. Repeat while $k < k_{max}$
   - Estimate ∇h_{k+1} by optimizing:

     $$\min TV(\nabla h_{k+1}) \text{ s.t. } ||o_k * \nabla h - \nabla i||_{\ell_2} \leq \eta \tag{6.18}$$

     Form h_{k+1} from ∇h_{k+1};
   - Estimate ∇o_{k+1} by optimizing:

     $$\min ||\nabla o_{k+1}||_{\ell_1} \text{ s.t. } ||h_{k+1} * \nabla o_{k+1} - \nabla i||_{\ell_2} \leq \epsilon \tag{6.19}$$

     Form o_{k+1} from ∇o_{k+1};
   - k=k+1

Since both the Laplacian ∇^2 and ∇ are linear operators, approximating them using standard finite differences yields a large system of linear equations.

Several methods have been proposed to solve Eq.6.20. For example, a full multigrid method in [169] is presented to solve the Laplacian equation with Gaussian-Seidel smoothing iterations, and a more efficient approach is to use a rapid Poisson solver, which uses a sine transform based on the method in [167] to invert the Laplacian operator. In our algorithm, we employ the method proposed by Weiss[164]. The method is based on the assumption that the derivative filter is sparse. Then a maximum-likelihood estimator is derived to recover the original image under this assumption.

6.7 Results

We test our algorithm using two different data sources: image frames taken through atmospheric turbulence and images taken through moving water surface. In the former case, both simulated and real-world data are tested.

The first test image sequence is the anisoplanatic distorted Lenna sequence used in Chapter 4. Here, we reiterate how the sequence is simulated: five different Kolmogorov phase screens with $D/r_0 = 1, 3, 5, 7, 2$ are used to produce a set of simulated turbulence affected images. This method employed the Layered algorithm in [134], using a simulated monochromatic wavelength of 500 nm, simulated layers at distances 5, 45, 55, 70, 105 m from the telescope and simulated sensor used to gather the imagery, ($D = 0.14m$, $f14$, $\Delta_{pixel} = 7\mu m$). In this case, a set of 100 images was produced, using a different randomly generated phase screens for each layer and each image.

The input of our blind deconvolution method is the result of the bispectrum technique, and the output is compared with the input (i.e., the estimate by the bispectrum technique), the ground truth image and one of the distorted images in Fig.6.3. Since we have a ground truth image, a numeric measurement (i.e., SNR) is used to determine the image quality. Fig.6.3 (c) is a restoration using bispectrum technique, which is the input to our blind deconvolution. The end result is shown in Fig.6.3 (d), which has the highest SNR with respect to the true image. Visually, this can be seen to be correct especially in the feathered region of the hat.

The second experiment is a real-world data, which is also obtained with a portable 0.14 m dia f14 Cassegrain telescope and progressive scan CCD camera. A test scene to be observed is about 10km distant and the exposure time is on order of 5ms.

Fig.6.4 shows the result (b) obtained only by the bispectrum method and another result (c) with removal of residual blur by our blind deconvolution method using (b). Also, one sample of short exposure images has been shown. Visually, (c) gives a much sharper version of the potential image and has more detail, which indicates that the blind deconvolution significantly boosts the high frequency content in (b), even though it produces some artifacts such as the "ringing" effect.

The final experimental data are from the image sequence which is taken in the case of "looking through-the-water imaging", which has been discussed in Chapter 5. The results are shown in Fig.6.5. Again, since we have no true image, we cannot use any numeric measure for comparison. From visual inspection, one can tell that (c), the result by the blind deconvolution method. It is sharper, for example, the English letters in the image is easier to read.

Our experiments seem show the proposed iterative algorithm does converge empirically, though so far we have no theoretical convergence proof, and this can be an important future work.

(a) The true image

(b) SNR = 11dB

(c) SNR = 19dB

(d) SNR = 23dB

Figure 6.3: Comparison of results. The result by our blind deconvolution method (d) is compared visually with the estimate by the bispectrum technique (c), the ground truth image (a) and one of the distorted images (b). Note that (d) has the highest SNR with respect to the true image, and the result from (c) is the input to (d).

(a) A sample input frame

(b) Result by the bispectrum technique

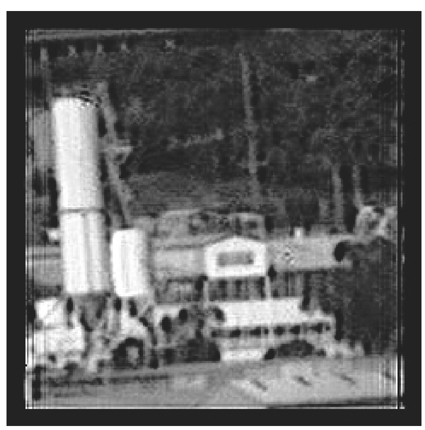

(c) Remove the residual blur by the BD method

Figure 6.4: Comparisons of results. (a) A sample of input frame; (b) the result obtained only by the bispectrum technique; (c) the result which is further processed by blind deconvolution.

(a) A sample input frame

(b) Result by the bispectrum technique

(c) Remove the residual blur by the BD method

Figure 6.5: Comparisons of results. (a) A sample of input frame; (b) the result obtained only by the bispectrum technique; (c) the result which is further processed by blind deconvolution.

6.8 Summary

In this chapter, we have investigated some characteristics of the estimated image obtained by methods developed in previous chapters. We pointed out that this estimated image is geometrically correct (i.e., has no region to region phase corruption) after the the phase correction by the bispectrum technique. However, it has remaining blur due to the "temporal averaging" in the computation of the Fourier modulus. In other words, the estimated image is still blurred by a spatial-invariant LPF.

An improvement is proposed: based on the result of previous methods, a further processing step (i.e., a blind deconvolution method) is applied to the result. This step aims to remove the residual blur remaining in the previous result and boost the high frequency information in the spatial image.

A novel blind deconvolution method is studied, which makes use of the natural image prior (i.e., the gradients of a natural image are sparsely distributed). To solve for an estimated image gradient, compressed sensing theory is employed, in particular, the ℓ_1-norm minimization is used. The performance of the new algorithm is demonstrated by data recorded in two cases: images taken through atmospheric turbulence and images taken through moving water waves.

Chapter 7

Closing Remarks

7.1 Summary

This thesis has investigated methods for recovering a single, superior quality and high resolution still image from a sequence of short exposure images taken through turbulent media, by extracting information contained in the sequence. The observation of the object of interest in wide field-of-view suffers from the rapidly changing turbulence which severely distorts the image sequences, with the effective PSFs of the recorded images to be both spatial and time variant. To overcome the distortions, images with short enough exposure time are taken to freeze the turbulence effect, and the information of the instantaneous turbulence retained in them are used to reconstruct a single estimate of the true image.

There are three main technique components in this thesis: (1) the bispectrum technique for image restoration; (2) the lucky region method for reconstruction and super-resolution, and (3) use of a natural image prior, i.e., sparsity, for blind deconvolution.

In addition, a novel application and adaptation of the above methods to solve imaging through and across a turbulent water surface has been studied, and very promising results are obtained.

The Bispectrum Technique An efficient technique has been investigated for extracting the Fourier phase information of the object of interest from a turbulent short exposure image sequence. This technique makes use of the averaged bispectrum of a set of short exposure images. Its performance has been demonstrated empirically, and the factors affecting the performance have been analyzed and verified experimentally.

The theoretical foundation of why and how the bispectrum technique works in wide-area/near-to-ground imaging has been explained. The averaged bispectrum of an image set contains the full Fourier phase information of the object, though in some scrambled version. We show how to unscramble it and recover the correct phase information. The averaging operation also effectively suppresses the inevitable additive zero-mean Gaussian noise.

The difficulties in using the bispectrum in practice are caused by the phase ambiguity, and by the large demands in storage and computational time. These issues have been discussed in detail, and we have provided a few practical solutions.

Partitioning the image into subregions is used to address the huge memory needs for the computation. Also, the feasibility of using parallel computing has been discussed, in which by careful coding, realtime implementation is possible.

Our extensive experiments have validated the bispectrum-based phase-recovery algorithm developed in this thesis. However, by carefully examining the remaining (residual) blur, we explain why the result (after this phase recovery stage) is still subject to high frequency content loss, leading to a result that is not exactly diffraction-limited resolution but having perceivable remaining uniform blur.

We have shown in the preceding chapter how this can be remedied by applying a further blind deconvolution technique using a natural image prior to the current result (which is another contribution of this thesis).

The Lucky Region Method In astronomical imagery it has been shown that, one can find a lucky image with negligible distortion or even approaching diffraction limited resolution among a large number of short exposure images. The method of finding lucky images and using them to reconstruct a single superior image is termed the lucky imaging technique. This method implies making use of possibly useful information and getting rid of harmful ambiguities retained in short exposure images.

Under typical seeing conditions, the probability of obtaining a lucky image exponentially decreases quickly as $(D/r_0)^2$ increases. When D/r_0 increases to 10, then 1 million short exposure images are needed to obtain one lucky image. Conditions will be poorer for anisoplanatic images.

This condition is improved by a simple yet effective modification, called the lucky region method, proposed in this thesis. This method partitions an image into a number of subregions (accordingly, for a sequence of images, a number of sequences of subregions are produced), and selects lucky regions for subsequent processing rather than entire lucky images. We theoretically show that the probability of obtaining a lucky region is significantly improved by this method.

Bicoherence as an image quality indicator was introduced and shown to be effective for lucky region selection, which detects and ranks the degree of quadratic phase coupling among different Fourier phase components in an image, and lucky regions are chosen according to the ranking. It has been shown that the application of this method in the bispectrum technique helps to produce better results.

This technique has been successfully applied in two applications: image restoration, and image super-resolution, for wide-area imaging. Experiments have convincingly indicated that results are superior to those using the whole set of image data.

Natural Image Prior Used for Blind Deconvolution We have shown that, while the resultant images obtained after the bispectrum-based speckle processing are geometrically correct, there is however residual blur caused by the "averaging operation" used in the computation of averaged bi-spectrum. To remove the residual blur and enhance the otherwise lost high frequency information, a post-processing stage, based on blind deconvolution, is recommended and investigated.

In order to better regularize the ill-posed image blind deconvolution problem, we have paid special attention to any available prior knowledge peculiar to our wide-area/near-to-ground application that may be taken advantage of. In particular, the objects of interest in our case are often from a natural scene, and often extended, i.e. with considerable size. To (statistically) specify this (seemingly too generic or weak) knowledge of the object, we use a general natural image prior that is based on the fact that natural signals often have sparse gradients.

Recently, sparse signal processing has received considerable attention from several research communities, under a common and newly emerging theoretical framework known as compressive sensing.

Based on techniques in compressive sensing (in particular, the ℓ_1-norm minimization), this thesis made an initial and preliminary attempt to develop a new blind deconvolution method. It is basically an iterative method, where the estimation of image gradients and the estimation of PSF gradients are employed in an iterative fashion.

The performance of this method has been tested empirically and the results compared with those of the methods introduced in earlier chapters, both with atmospheric turbulence affected data and moving water surface affected data. The SNR is improved in simulated experiments. In real-world experiments, the resultant images are sharper.

Water Imaging This thesis has also studied another important image restoration problem, i.e., imaging through or across a turbulent water surface.

We notice (through theoretical analysis and experimental observation and validation) that the condition for water imaging possesses the same or similar statistical characteristics to atmospheric turbulence.

We have studied two typical scenarios of water imaging. The first scenario is imaging through a moving water surface (an object lies stationary on the ground under the water, and a detector hangs stationary above the water surface and records images through the water surface). The second scenario is imaging by the reflection from the moving water waves (an object hangs still above the water surface, and a detector hangs stationary on the other side and records images reflected by water surface). For both scenarios we have proposed an efficient method for removing the distortion due to the moving water surface.

Similar to the case of imaging through atmospheric turbulence, when the water wave length is shorter than the object of interest, images taken in this case have an anisoplanatic PSF. To improve the conditions, segmentation and the lucky region technique have been applied, followed by the bispectrum for image region reconstruction.

This application has been tested with real data in both cases. Impressive results have been obtained, which indicates that the research in this thesis can be simply extended to diverse areas where the statistical characteristics of the distorting medium are similar to those of atmospheric turbulence.

To our knowledge, this work represents an original contribution of the thesis to this special water imaging problem.

7.2 Future Work

This final section discusses some possible avenues for future research in wide-area/near-to-ground imaging and extended applications of the techniques described in this thesis.

Sparsity used in the bispectrum technique A natural image prior, sparsity, helps to boost high frequency content in the classical blind deconvolution, which is performed on a single image. Intuitively, we feel that this prior can be applied to image restoration using multiple images, and even to be an internal part of the bispectrum technique.

Since the phase of the object relates to the phase of the averaged bispectrum by linear operations, not by other ways, in the bispectrum based method, it is possible to embed the prior in the restoration process. But how to involve the prior when computing the Fourier phase and magnitude of the object from the averaged bispectrum, we do not yet have a clear idea. This will be a possible next step of our future research.

Application to wide-area moving targets Speckle imaging and techniques described in this thesis are proposed for image reconstruction for static objects in wide-area imaging. These methods have been proved successful to obtain diffraction limited resolution or high resolution images. In other cases, when the object of interest has some sort of relative motion to background, the frames not only suffer from a position dependent and time variable PSF due to the effect of atmospheric turbulence, but the position of the object changes from frame to frame, making image reconstruction of the object more difficult.

The research in this thesis may be able to deal with the task with some modifications to the algorithms. Indeed, Carrano et al. have presented a simple modification to the bispectrum technique for the task. Their approach, applies the bispectrum method, tracks and extracts out the target with maximum background elimination. In this way, the motion of the object to background is removed and the object is treated as a static object when performing the general bispectrum method to the extracted images[5].

Future research may follow this idea: a preprocessing step to produce images with apparently stationary objects, followed by speckle imaging techniques such as the bispectrum to enhance the imagery. Practical applications might include recognition of motor cars on a highway, aircraft from high altitude, and animal observations and tracking outdoors.

Appendix A

Parallel Implementation–Some Future Thoughts

Parallel computing is another solution for large data processing problems which can be divided into smaller ones. Smaller instruction sets and data sets are sent to different computers or processors, the results from them are then sent back to the main memory for further processing. Here, we give some future thoughts and theoretical analysis on the feasibility of parallel implementation for large scale image bispectrum computation.

Traditionally, the implementation of the strategy demonstrated in Fig.3.6 on a personal computer must be serial. This means that the algorithm is constructed and implemented as a serial stream of instructions, and only one executes at a time. In this context, before the program start to process the 2nd series of data, it has to wait until the 1st subsequence of data has been fully processed.

Since the process of the subsequences of data is isolated, i.e., the calculation of one data set is independent on the others, the computation of the bispectrum and phase recovery from the calculated bispectrum can be implemented in parallel. Thus different data

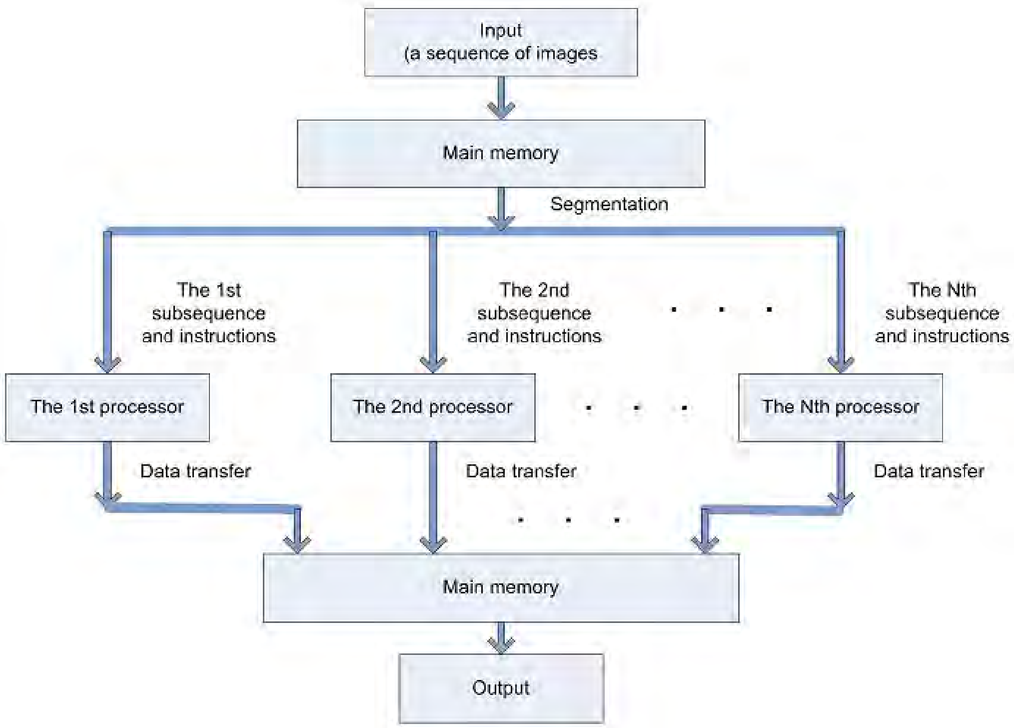

Figure A.1: The ith ($i = \{1, 2, \cdots, N\}$) subsequences are sent to different processors to process, the results are then transferred back to the main memory for further process.

sets with corresponding instructions can be sent to different computers (or processors) for processing, as in Fig.3.8.

Suppose there are N processing notes connected to a host computer; the program divides the input data into N subregions, distributes them among the processing notes with processing instructions, then waits for the results to be returned. Once all subregion results are returned, the host collates them.

With proper and careful development of the code, parallel computing can significantly accelerate the speed of the algorithm. Realtime image restoration using the bispectrum may be realized through parallel computing, proper strategy and code optimization. This would be of great benefit to the AO techniques, which need realtime reaction to the captured signals.

The three methods can work with and benefit each other with carefully designing the algorithms. The first two are able to be completed only using a personal computer. Only calculating the non-redundant slice of the bispectrum improves the conditions of the algorithm. However, the computing period is still too long for real-time implementation. This difficulty can be overcome by the third method which divides the task into a number of smaller tasks and each subtask is solved by a separate processor.

To our knowledge, only a few other methods have been proposed for the problem. Tyler et al designed a "part-bispectrum" approach to estimate the phase in parts rather then to estimate an entire phase spectrum[54]. Their methods named "parallel part-bispectrum algorithm" can be extended to run on parallel machines . Some methods speed up the computations by designing a fast algorithms by using the selected and useful frequency components[52, 43]. These methods are different from ours, which recovers a number of subregions using parallel strategy, but is not about computing the bispectrum part by part.

As there are various available computing architectures for parallel computation, and possibly more are emerging, we have deliberately not specified which particular type of parallel architecture we are referring to. For the near future, we were planning to implement and test our algorithms on a multi-core machine, and a GPU system—nowadays these two are the most affordable parallel super-computers for a typical PC user.

Appendix B

Two-dimensional Discrete Convolution

When using compressed sensing theory and ℓ_1-norm minimization, no convolution operation is permitted. However, in image processing, and in the imaging model we use, two-dimensional discrete convolution is a basic operation. Fortunately, convolution is a linear operation and can be transformed to matrix-vector form, which favours the forms in Eq.6.10. This section presents two methods to convert classical discrete convolution to matrix-vector form: one is general and usually mentioned in literature and the other is new, simple and only proposed in this thesis.

B.1 General Matrix Construction

Let us repeat the definition of convolution of Eq.(3.10),

$$f * g = \int_{-\infty}^{\infty} f(x) g(\xi - x) dx \tag{B.1}$$

If f and g are two-dimensional, and discrete: $f = f(m,n)$, for $(0 \leq m \leq N_1 - 1, 0 \leq n \leq N_2 - 1)$ and $g = g(m,n)$, for $(0 \leq m \leq M_1 - 1, 0 \leq n \leq M_2 - 1)$, the two-dimensional convolution is

$$\begin{aligned} f * g &= f(m,n) * g(m,n) \\ &= \textstyle\sum_{k=0}^{N_1-1} \sum_{l=0}^{N_2-1} f(k,l) g(m-k, n-l) \\ &= \textstyle\sum_{k=0}^{M_1-1} \sum_{l=0}^{M_2-1} g(k,l) f(m-k, n-l) \end{aligned} \tag{B.2}$$

for $(m = 0, 1, \cdots, M_1 + N_1 - 2; n = 0, 1, \cdots, M_2 + N_2 - 2)$. In practical application, another expression for the discrete convolution operation is often used:

$$f * g = M_g \vec{f} \tag{B.3}$$

where $\vec{f}$ is a vector built by the rows of f. Denote the ith row in f as f_i,

$$\vec{f} = (f_0, f_1, \cdots, f_{N_1})^T \tag{B.4}$$

M_g is a matrix defined by

$$\mathbf{M_g} = \begin{pmatrix} M_{(g_1,N_2)} & & & \\ M_{(g_2,N_2)} & M_{(g_1,N_2)} & & \\ \vdots & \vdots & \ddots & \\ \vdots & \vdots & & M_{(g_1,N_2)} \\ M_{(g_{M_1},N_2)} & \vdots & & \vdots \\ & M_{(g_{M_1},N_2)} & \ddots & \vdots \\ & & & M_{(g_{M_1},N_2)} \end{pmatrix}$$

where M_{g_i,N_2} is a matrix constituted for the convolution of f and $\vec{g_i}, i = 1, 2, ..., M_1$:

$$f * \vec{g_i} = M_{g_i} \vec{f} \tag{B.5}$$

where $\vec{g_i} = g_i^T = (g_{i,0}, g_{i,1}, \cdots, g_{i,M_2})^T$, $M_{(g_i,N_2)}$ is given

$$\mathbf{M_{g_i}} = \begin{pmatrix} g_{i,0} & & & \\ g_{i,1} & g_{i,0} & & \\ \vdots & \vdots & \ddots & \\ \vdots & \vdots & & g_{i,0} \\ g_{i,M_2-1} & \vdots & & \vdots \\ & g_{i,M_2-1} & \ddots & \vdots \\ & & & g_{i,M_2-1} \end{pmatrix}$$

This type of expression converts the convolution operation to linear algebra operations, reducing the implementation complexity when considering the inverse problem of convolution. However, M_g is too large to be stored and computed in Matlab for an image with common size of, say, 512×512 pixels.

In fact, M_g constructed in this way has many redundant entries which are zero valued and will slow down the speed of the computation. In other words, M_g can be made more tidy and easy to use. To do so, this thesis develops a simple but more efficient method, which is described in the next subsection.

B.2 New Matrix Construction

This thesis proposes a simple M_g construction method. The created M_g has no redundancy and is much less demanding in storage and computation. It is an M_1M_2xN_1N_2 matrix, which is defined as

$$M_g = (M_{0,0}, M_{0,1}, \cdots, M_{0,M_2}, M_{1,0}, M_{1,1}, \cdots, M_{1,M_2}, \cdots, \cdots, M_{M_1,0}, M_{M_1,1}, \cdots, M_{M_1,M_2})^T \tag{B.6}$$

where $M_{k,l}(0 \leq k \leq M_1 - 1, 0 \leq l \leq M_2 - 1)$ are vectors with size $1\text{x}N_1N_2$ entries, which are formed by an area in g. The center of the area is at (k, l) and the size is $N_1\text{x}N_2$.

$$\vec{M_{k,l}} = ((g_{k-\frac{N_1}{2},l-\frac{N_2}{2}}, g_{k-\frac{N_1}{2},l-\frac{N_2}{2}+1}, \cdots, g_{k-\frac{N_1}{2},l+\frac{N_2}{2}}, \cdots, g_{k+\frac{N_1}{2},l-\frac{N_2}{2}}, g_{k+\frac{N_1}{2},l-\frac{N_2}{2}+1}, \cdots, g_{k+\frac{N_1}{2},l+\frac{N_2}{2}}) \tag{B.7}$$

Here is an example,

$$\mathbf{g} = \begin{pmatrix} 1 & 2 & 5 & 7 \\ 27 & 9 & 2 & 23 \\ 11 & 3 & 6 & 7 \\ 6 & 8 & 9 & 12 \end{pmatrix}$$

$$\mathbf{f} = \begin{pmatrix} 2 & -1 & 5 \\ 1 & 2 & 3 \\ -2 & 7 & 3 \end{pmatrix}$$

From Eqs.B.4 and B.6, we calculate vector $\vec{f}$ and matrix M_g, where $\vec{f} = f'^T$

$$\mathbf{f}' = \begin{pmatrix} 2 & -1 & 5 & 1 & 2 & 3 & -2 & 7 & 3 \end{pmatrix}$$

and

$$\mathbf{M_g} = \begin{pmatrix} 0 & 0 & 0 & 0 & 1 & 2 & 0 & 27 & 9 \\ 0 & 0 & 0 & 1 & 2 & 5 & 27 & 9 & 2 \\ 0 & 0 & 0 & 2 & 5 & 7 & 9 & 2 & 23 \\ 0 & 0 & 0 & 5 & 7 & 0 & 2 & 23 & 0 \\ 0 & 1 & 2 & 0 & 27 & 9 & 0 & 11 & 3 \\ 1 & 2 & 5 & 27 & 9 & 2 & 11 & 3 & 6 \\ 2 & 5 & 7 & 9 & 2 & 23 & 3 & 6 & 7 \\ 5 & 7 & 0 & 2 & 23 & 0 & 6 & 7 & 0 \\ 0 & 27 & 9 & 0 & 11 & 3 & 0 & 6 & 8 \\ 27 & 9 & 2 & 11 & 3 & 6 & 6 & 8 & 9 \\ 9 & 2 & 23 & 3 & 6 & 7 & 8 & 9 & 12 \\ 2 & 23 & 0 & 6 & 7 & 0 & 9 & 12 & 0 \\ 0 & 11 & 3 & 0 & 6 & 8 & 0 & 0 & 0 \\ 11 & 3 & 6 & 6 & 8 & 9 & 0 & 0 & 0 \\ 3 & 6 & 7 & 8 & 9 & 12 & 0 & 0 & 0 \\ 6 & 7 & 0 & 9 & 12 & 0 & 0 & 0 & 0 \end{pmatrix}$$

This new method produces the same convolution result as when using the “filter2” function in MATLAB. The construction of M_g is easier to understand and the storage of M_g declines significantly (no redundant entries). It can be freely used in any MATLAB code.

References

[1] C. Carrano. Speckle imaging over horizontal paths. *SPIE Proceedings, Conference on Advanced Wavefront Control*, 4825:65–75, 2002.

[2] C. Carrano. Anisoplanatic performance of horizontal-path speckle imaging. *SPIE Proceedings, Conference on Advanced Wavefront Control*, 5162:14–26, 2003.

[3] C. J. Carrano. Progress in horizontal and slant-path imaging using speckle imaging. *Proceedings of the SPIE: LASE*, 5001:56–64, 2003.

[4] C. J. Carrano and J. M. Brase. Horizontal and slant path surveillance with speckle imaging. *Proceedings of AMOS, Technical Conference Proceedings*, 2002.

[5] C. J. Carrano and J. M. Brase. Adapting high-resolution speckle imaging to moving targets and platforms. *Proceedings of the SPIE: ISR*, 5409:96–105, 2004.

[6] J. N. Cederquist, J. R. Fienup, J. C. Marron, and R. G. Paxman. Phase retrieval for experimental far-field speckle data. *Optics Letters*, 13:619–621, 1988.

[7] L.P. Yaroslavsky, B. Fishbain, I. Ideses, D. Slasky, and Z. Hadas. Simple methods for real time stabilization of turbulent video. *Proceedings of ICO, Topical Meeting on Optoinformatics*, 2006.

[8] B. Fishbain, L. P. Yaroslavsky, I. A. Ideses, A. Shtern, and O. Ben-Zvi. Real-time stabilization of long-range observation system turbulent video. *proc. of Real-Time Image Processing/Electronic Imaging 2007, SPIE*, 6496, 2007.

[9] B. Fishbain, I.A. Idess, Sh. Gepstein, and L.P. Yaroslavsky. Turbulent video enhancement: Image stabilization and super-resolution. *Proc of IEEE, Optical Engineering and Science*, 2007.

[10] B. Fishbain, I.A. Idess, Sh. Gepstein, and L.P. Yaroslavsky. Superresolution in turbulent videos: making profit from damage. *Optics Letters*, 32:3038–3040, 2007.

[11] D. Fraser, G. Thorpe, and A. Lambert. Atmospheric turbulence visualization with wide-area motion-blur restoration. *J.Opt.Soc.Am.A.*, 16:1751–1758, July 1999.

[12] D. Fraser, A. Lambert, M.R.S. Jahromi, M. Tahtali, and D.Clyde. Anisoplanatic image restoration at ADFA. *Proc. Digital Image Computing: Techniques and Applications*, pages 19–28, Dec 2003.

[13] A. Lambert, D. Fraser, D. Bowman, S. Brandon, and J. Davies. Turbulence profiling for long range surveillance imaging. *Proceedings of the SPIE*, 7076:70760D–70760D–10, 2008.

[14] M. Roggemann and B. Welch. *Imaging Through turbulence*. CRC Press LLC, 1996.

[15] A. Labeyrie. High resolution techniques in optical astronomy. *Progress in optics, Physics Reports (North Holland),*, XIV:49–87, 1976.

[16] S.P. Worden. Astronomical image reconstruction in astronomy. *Vistas Astronomy*, 20:301–307, 1977.

[17] A. Labeyrie. Stellar interferometry methods. *Ann. Rev. Astronomy Astrophys.*, 16:77–102, 1978.

[18] R.J.T. Bates. Astronomical speckle imaging. *Physics Rep.*, 90:203–297, 1982.

[19] J.C. Dainty. Stellar speckle interferometry. *Laser Speckle and Related Phenomena*, Ed., Springer-Verlag, Berlin:255–320, 1984.

[20] J.A. McAlister. High angular resolution mesurements of stellar properties. *ANN. Rev. Astronomy Astrophys.*, 23:59–88, 1985.

[21] J.W. Goodman. *Statistical Optics*. John Wiley and Sons, New York, 1987.

[22] F. Roddier. Interferometric imaging in optical astronomy. *Physics Rep.*, 170:98–166, 1987.

[23] E. Horch. Speckle imaging in astronomy. *International Journal of Imaging Systems and Technology*, 6:401–417, 1995.

[24] C. Aime. Teaching astronomical speckle techniques. *European Journal of Physics*, 22:169–184, 2001.

[25] S.K. Saha. Modern optical astronomy: technology and impact of interferometry. *Reviews of Modern Physics*, 74:551–594, 2002.

[26] J.C. Dainty and J. R. Fienup. Phase retrieval and image reconstruction for astronomy. *Image Recovery*, pages 231–275, 1987.

[27] K.T. Knox and B.J.Thompson. Recovery of images from atmospherically degraded short-exposure images. *Astrophys.J.*, 193:L45–L48, 1974.

[28] K.T. Knox. Image retrieval from astronomical speckle patterns. *JOSA.A*, 66:1236–1239, 1976.

[29] A. W. Lohmann, G. P. Weigelt, and B. Wirnitzer. Speckle masking in astronomy: triple correlation theory and applications. *Appl. Opt.*, 22:4028–4037, July 1983.

[30] G. P. Weigelt. Modified speckle interferometry: speckle masking. *Opt. Commum.*, 21:55–59, 1976.

[31] G. P. Weigelt and B. Wirnitzer. Image reconstruction by the speckle-masking method. *Opt. Lett.*, 22:4028–4037, 1983.

[32] G.R. Ayers, M.J. Northcott, and J.c. Dainty. Knox-thompson and triple-correlation imaging through atmospheric turbulence. *JOSA.A*, 5:963–985, 1988.

[33] G. C. Dente. Speckle imaging and hidden phase. *Applied Optics*, 39:1480–1485, 2000.

[34] P. Negrete-Regagnon. Practical aspects of image recovery by means of the bispectrum. *JOSA.A*, 13:1557–1576, 1996.

[35] J.W. Beletic. Speckle imaging of complicated objects. *Ph.D. Thesis,Harvard Univ., Cambridge, MA.*, 1989.

[36] J.C. Dainty. Bispectrum imaging through turbulence. *IEEE workshop on Higher-Order Spectral Analysis*, pages 130–134, 1989.

[37] F. Roddier. Triple correlation as a phase closure technique. *Optics Communications*, 60:145–148, 1986.

[38] D.J. Cho, E.A.Watson, and G.M. Morris. Application of bispectral speckle imaging to near-diffraction-limited imaging in the presence of unknown aberrations. *Applied Optics*, 34:854–864, 1995.

[39] R. Barakat and S. Ebstein. Bispectral diffration imagery. i. the bispectral optical transfer function. *JOSA.A*, 4:1756–1763, 1987.

[40] H. Bartle, A. Lohmann, and B. Wirnitzer. Phase and amplitude recovery from bispectra. *J.Opt.Soc.Am*, 23:3121–3129, Sept. 1984.

[41] J. Meng, J.M. Aitken, E.K. Hege, and J.S. Morgan. Triple-correlation subplane reconstruction of photon-address stellar images. *JOSAA*, 7:1243–1250, 1990.

[42] A.T. Erdem and M. I. Sezan. Least-squares reconstruction of an image from its noisy observations using the bispectrum. *IEEE Sixth SP Workshop on Statistical Signal and Array Processing*, pages 156–159, 1992.

[43] H. Takajo and T. Takahashi. Least-squares phase recovery from the bispectrum phase: an algorithm for a two-dimensional object. *JOSA.A*, 8:1038–1047, 1991.

[44] T. Matsuoka and T.J. Ulrych. Phase estimation using the bispectrum. *Proc. of the IEEE*, 72:1403–1411, 1984.

[45] C. Matson. Weighted-least-squares phase reconstruction from the bispectrum. *J.Opt.Soc.Am.A*, 8:1905–1913, 1991.

[46] J.C. Marron, P.P. Sanchez, and R.C. Sullivan. Unwrapping algorithm for least-squares phase recovery from the modulo 2π bispectrum phase. *JOSA.A*, 7:14–20, 1990.

[47] H. Takajo and T. Takahashi. Lease-squares phase recovery from the bispectrum phase: an algorithm for a two-dimensional object. *JOSA.A*, 8:1038–1047, 1991.

[48] A. Lannes. Backprojection mechanism in phase-closure imaging. bispctral analysisi of the phase-restoration process. *Exp. Astron*, 1:47–76, 1989.

[49] P. W Gorham, A. M. Ghez, S. R. Kulkarni, T. Nakajima, G. Neugebauer, J. B. Oke, and T. A. Prince. Diffraction-limited imaging. iii. 30 m as closure phase imaging of six binary stars with the hale 5 m telescope. *Astron. J*, 98:1783–1799, 1989.

[50] A. Glindemann, R.G. Lane, and J.C. Dainty. Least-squares reconstruction of the object phase from the bispectrum. *Diginal Signal Processing*, pages 59–65, 1991.

[51] C.A. Haniff. Lease-squares fourier phase estimation from the modulo 2π bispectrum phase. *JOSA.A*, 8:134–140, 1991.

[52] S.A. Dianat and M.R. Raghuveer. Fast algorithms for bispectral reconstruction of two-dimensional signals. *IEEE International Conference on Acoustics, Speech, and Signal Processing*, 5:2377–2379, 1990.

[53] G. Sundaramoorthy, M.R. Raghuveer, and S.A. Dianat. Robust object reconstruction from noisy observations. *Proceeding of SPIE: Visual Communication and Image Processing*, 1199:104–114, 1989.

[54] D.W. Tyler and K.J. Schulze. Fast phase spectrum estimation using the parallel part-bispectrum algorithm. *The Astronomical Society of the Pacific*, 116:65–76, 2004.

[55] K.J. Schulze, D.W. Tyler, and Stribing C.B. Near real-time speckle imaging for optimization of observing parameters. *Proceedings of SPIE*, 3349:165–172, 1998.

[56] R.J.T. Bates and F.W. Cady. Towards true imaging by wideband speckle interferometry. *Opt. Commun.*, 32:365–369, 1980.

[57] C.R. Lynds, S.P. Worden, and J.W. Harvey. Digital image reconstruction applied to alpha orionis. *Astrophys.J.*, 207:174, 1976.

[58] F.W. Cady and R.J.T. Bates. Speckle processing gives diffraction-limited true images from severly aberrated instrument. *Optics Letters*, 5:438–440, 1980.

[59] S.P. Worden, C.R. Lynds, and J.W. Harvey. Reconstructed images of alpha orionis using stellar speckle interferometry. *JOSA*, 66:1243–1246, 1976.

[60] W.G. Bagnuolo. Image restoration by the shift-and-add algorithm. *Optics Letters*, 10:200–202, 1985.

[61] W.G. Bagnuolo. The application of bates' algorithm to binary stars. *Mon.Not.R.Astron.Soc.*, 200:1113, 1982.

[62] B. R. Hunt, W. R. Fright, and R H T Bates. Analysis of the shift-and-add method for imaging through turbulent media. *JOSA.A*, 73:456–465, 1983.

[63] J.C. Christou, E.K. Hege, J.D. Freeman, and E. Ribak. Slef-calibrating shift-and-add technique for speckle imaging. *JOSA.A*, 3:204–209, 1986.

[64] D. Fried. Probability of getting a lucky short-exposure image through turbulence. *J.Opt.Soc.Am.A.*, 68:1651–1658, 1978.

[65] J.L. Nieto and E. Thouvenot. Recentring and selection of short-exposure images with photon-counting detectors. *Astronomy and Astrophysics*, 241:663–672, 1991.

[66] Wikipedia the free encyclopedia. Lucky imaging. *http://en.wikipedia.org/wiki/Lucky_imaging.*

[67] N. Law, C. Mackay, and J. Baldwin. Lucky imaging: high angular resolution imaging in the visible from the ground. *Astronomy & Astrophysics*, 446:739–745, 2006.

[68] R. Tubbs. Lucky exposures: Diffraction limited astronomical imaging through the atmosphere. *PhD Thesis, Cambridge University*, 2003.

[69] S. Weddell and R. Webb. Data preprocessing on sequential data for improved astronomical imaging. *Proceedings of IEEE, Image and Vision Computing*, 2005.

[70] M. Vorontsov and G. Carhart. Anisoplanatic imaging through turbulent media: image recovery by local information fusion from a set of short-exposure images. *J.Opt.Soc.Am.A.*, 18:1312–1324, June 2001.

[71] D. Kundur and D. Hatzinakos. Blind image deconvolution. *IEEE Signal Processing Magazine*, 13:6163, 1996.

[72] A.V. Oppenheim, T.W. Schafer, and T.G. Stockham. Non-linear filtering of multiplied and convolved processing. *Proc. IEEE*, 56:1264–1291, 1968.

[73] T.G. Stockham, T.M. Cannon, and R.B. Ingebretsen. Blind deconvolution through digital signal processing. *Proc. IEEE*, 63:678–692, 1968.

[74] R.G. Lane and R.H.T. Bates. Automatic multidimensional deconvolution. *JOSA.A*, 4:180–188, 1987.

[75] G.R. Ayers and J.C. Dainty. Iterative blind deconvolution method and its applications. *Optics Letters*, 13:547–549, 1988.

[76] Q. Shan, W. Xiong, and J. Jia. Rotational motion deblurring of a rigid object from a single image. *ICCV*, pages 1–8, 2007.

[77] R.G. Lane. Methods for maximum-likelihood deconvolution. *JOSA.A*, 13:1992–1998, 1996.

[78] W.H. Richardson. Bayesian-based iterative method of image restoration. *JOSA.A*, 62:55–59, 1972.

[79] L.B. Lucy. An iterative technique for the rectification of observed images. *The Astronomical Jounal*, 79:745–754, 1974.

[80] T.J. Holmes. Expectation-maximization restoration of band-limited, truncated point-process intensities with application in microscopy. *JOSA.A*, 6:1006–1014, 1989.

[81] T.J. Schulz. Multiframe blind deconvolution of astronomical images. *JOSA.A*, 10:1964–1073, 1993.

[82] A.P. Dempster, N.M. Laird, and D.B. Rubin. Maximum likelihood from incomplete data via the em algorithm. *Journal of the Royal Statistical Society, Series B*, 39:1–38, 1977.

[83] E. Thiebaut and J.M. Conan. Strict a prior constraints for maximum-likelihood blind deconvolution. *JOSA.A*, 12:485–492, 1995.

[84] T.J. Holmes. Blind deconvolution of quantum-limited incoherent imagery: maximum-likelihood approach. *JOSA.A*, 9:1052–1061, 1992.

[85] R. Fergus, B. Singh, A. Hertzmann, S.T. Roweis, and W.T. Freeman. Removing camera shake from a single photograph. *SIGGRAPH*, 25:787 – 794, 2006.

[86] Anat Levin. Blind motion deblurring using image statistics. *Advances in Neural Information Processing Systems (NIPS)*, pages 841–848, 2006.

[87] N. Joshi, R. Szeliski, and D. Kriegman. Psf estimation using sharp edge prediction. *CVPR*, pages 1–8, June 2008.

[88] J.W. Miskin and D.J.C. MacKay. *Ensemble learning for blind image separation and deconvolution*. 2000.

[89] Anat Levin, Yair Weiss, Fredo Durand, and William T. Freeman. Understanding and evaluating blind deconvolution algorithms. *CVPR*, pages 1964–1971, 2009.

[90] L. Yuan, J. Sun, L. Quan, and H. Shum. Image deblurring with blurred/noisy image pairs. *ACM Trans. on SIGGRAPH*, 26(3):1–10, 2007.

[91] A. Levin, R. Fergus, F. Durand, and W.T. Freeman. Deconvolution using natural image prior. *ETAI*, pages 1–3, 2007.

[92] E.P. Simoncelli. Bayesian denoising of visual images in the wavelet domain. *In Bayesian Inference in Wavelet Based Models*, pages 291–308, 1999.

[93] M.F. Tappen, B. C. Russell, and W. T. Freeman. Exploiting the sparse derivative prior for super-resolution and image demosaicing. *Proc. IEEE Workshop Statistical and Computational Theories of Vision*, pages 1–28, 2003.

[94] M.J. Fadili, J.L. Starck, and F. Murtagh. Inpainting and zooming using sparse representations. *The Computer Journal*, 52:64–79, 2007.

[95] M. M. Bronstein, A. M. Bronstein, M. Zibulevsky, and Y. Y. Zeevi. Blind deconvolution of images using optimal sparse representations. *IEEE Transactions on Image Processing*, 142:726–736, 2005.

[96] J. Cai, H. Ji, C. Liu, and Z. Shen. High-quality curvelet-based motion deblurring from an image pair. *In CVPR*, pages 1566–1573, 2009.

[97] L. Yuan, J. Sun, L. Quan, and H. Shum. Blurred/non-blurred image alignment using sparseness prior. *ICCV*, pages 1–8, 2007.

[98] A. Levin and Y. Weiss. User assisted separation of reflections from a single image using a sparsity prior. *In Pattern Analysis and Machine Intelligence, PAMI*, 29:1647–1654, 2007.

[99] J. Yang, J. Wright, Y. Ma, and T. Huang. Image super-resolution as sparse representation of raw image patches. *In Computer Vision and Pattern Recognition, CVPR*, pages 1–8, 2008.

[100] A. Levin, R. Fergus, F. Durand, and W. Freeman. Image and depth from a conventional camera with a coded aperture. *ACM Transactions on Graphics (Proc. SIGGRAPH)*, 2007.

[101] C. Nikias and A. Petropulu. *Higher-Order Spectra Analysis*. PTR Prentice Hall, New Jersey, 1993.

[102] J. Mendel. Tutorial on higher-order statistics (spectra) in signal processing and system theory: theoretical results and some applications. *Proc. IEEE*, 79:278–305, March 1991.

[103] A. Lohmann and B. Wirnitzer. Triple correlations. *Proc. IEEE*, 72:889–901, July 1984.

[104] M.J. Northcott, G.R. Ayers, and J.C. Dainty. Algorithms for image reconstruction from photon-limited data using the triple correlation. *JOSA.A*, 5:986–992, 1988.

[105] D.M. Goodman, T.W. Lawrence, J.P. Fitch, and E.M. Johnson. Bispectral-based optimization algorithms for speckle imaging. *In Digital Image Synthesis and Inverse Optics, Proc. Soc. Photo-opt. Intrum. Eng.*, 1351:546–560, 1990.

[106] M. Rangoussi and G.B. Giannakis. Fir modeling using log-bispectra: weighted least-squares algorithms and performance analysis. *IEEE Trans. Circuits Syst.*, 38:281–296, 1991.

[107] Z. Wen, D. Fraser, and A. Lambert. Bicoherence used to predict lucky regions in turbulence affected surveillance. *IEEE International Conference on Advanced Video and Signal Based Surveillance (AVSS'06)*, pages 108–114, Nov 2006.

[108] Z.Y. Wen, D. Fraser, and A. Lambert. Bicoherence: a new lucky region technique in anisoplanatic image restoration. *Applied Optics*, 48:6111–6119, 2009.

[109] Introducing higher order statistics (hos) for the detection of nonlinearities. *http://www.maths.leeds.ac.uk/Applied/news.dir/issue2/hos_intro.html*.

[110] H. Akaike. Notes on lecture at the institute of statistical mathematics. *The Statistical Theory of Spectral Estimation*, pages 1–130, 1964.

[111] John W. Hardy. *Adaptive Optics for Astronomical Telescopes.* Oxford University Press, 1998.

[112] A.M. Eskicioglu. Quality measurement for monochrome compressed images in the past 25 years. *IEEE conference on Acoustics, Speech, and Signal Processing*, 6:1907–1910, 2000.

[113] B. Girod. *What's wrong with Mean-Squared Error.* 1993.

[114] A. M. Eskicioglu and P. S. Fisher. Image quality measures and their performance. *IEEE Transactions on Communications*, 2959-2965:1995, 43.

[115] A. Michelson. *Studies in Optic.* U. of Chicago Press, 1927.

[116] C. Y. Wee and R. Paramesran. Measure of image sharpness using eigenvalues. *Information Science*, 177:2533–2552, 2007.

[117] Z. Wang and A. Bovik. A universal image quality index. *IEEE Signal Processing Letters*, 9:81–84, 2002.

[118] H. Akaike. Note on higher order spectra. *Ann. Inst. Statist. Math.*, 18:123–126, 1966.

[119] S. McLaughlin J. Fackrell and P. White. Practical issues concerning the use of the bicoherence for the detection of quadratic phase coupling. *IEEE workshop on HOS*, pages 10–37, 1993.

[120] Y.C. Kim and E.J. Powers. Digital bispectral analysis of self-excited fluctuations spectra. *Phys. Fluids*, 21:1452–1453, 1978.

[121] M.R. Raghuveer and C.L. Nikias. Bispectrum estimation: a parametric approach. *IEEE Acoustics, Speech and Signal Processing*, 33:1213–1230, 1985.

[122] M. Hinich and M. Wolinsky. Normalizing bispectra. *Journal of Statistical Planning and Inference*, 130:405–411, 2005.

[123] C.L. Nikias and M.R. Raghuveer. Bispectrum estimation: a digital signal processing framework. *Proc. IEEE*, 75:869–891, 1987.

[124] Y.C. Kim and E.J. Powers. Digital bispectral analysis and its applications to nonlinear wave interactions. *IEEE Trans Plasma Sci. PS*, 7:120–131, 1979.

[125] R. Haubrich. Earch noises, 5 to 500 millicycles per second, 1,. *J. Geophys. Res.*, 70:1415–1427, 1965.

[126] S.Elgar and R.T. Guza. Statistics of bicoherence. *IEEE Acoustics, Speech and Signal Processing*, 36:1667–1668, 1988.

[127] T.D. de Wit. *Spectral and statistical analysis of plasma turbulence: beyond linear techniques*. Springer, Berlin, 2003.

[128] W. Silva, T. Strganac, and M. Hajj. Higher-order spectral analysis of a nonlinear pitch and plunge apparatus. *46th AIAA/ASME/ASCE/AHS/ASC Structures, Structural Dynamics, and Materials Conference*, pages 1–20, April 2005.

[129] T. Ng, S. Chang, and Q. Sun. Blind detection of photomontage using higher order statistics. *International Symposium on Circuits and Systems, ISCAS*, 5:688–691, 2004.

[130] J. Fackrell and S. McLaughlin. Quadratic phase coupling detection using higher order statistics. *in Proceedings of the IEE Colloquium on Higher Order Statistics*, pages 1–9, 1995.

[131] H. Farid and A. Popescu. Blind removal of image non-linearities. *Proc. of IEEE, ICCV*, 1:76–81, 2001.

[132] R Shefer, M. Malhi, and A. Shenhar. Waves distortion correction using cross correlation. *http://visl.technion.ac.il/projects/2000maor/*, 2001.

[133] C. M. Harding, R. A. Johnston, and R. G. Lane. Fast simulation of a kolmogorov phase screen. *Applied Optics*, 38:2161–2170, 1999.

[134] A. J. Lambert and D.Fraser. Superresolution in imagery arising from observation through anisoplanatic distortion. *SPIE Image Reconstruction from Incomplete Data III*, 5562:65–75, 2004.

[135] M. I. Charnotskii, V. A. Myakinin, and V. U. Zavorotnyy. Observation of superresolution in nonisoplanatic imaging through turbulence. *J.Opt.Soc.Am.A.*, 7:1345–1350, August 1990.

[136] A. Lambert, D. Fraser, M. Reza Sayyah Jahromi, and B.R. Hunt. Super-resolution in image restoration of wide-area images viewed through atmospheric turbulence. *Proc. SPIE*, 4792:35–43, July 2002.

[137] M. I. Charnotskii. Imaging in turbulence beyond diffraction limits. *In Proceedings of SPIE*, 2534:289297, 1995.

[138] A. Lambert, F. Li, D. Bowman, and D. Fraser. Experiments in turbulence induced super-resolution in surveillance imagery. *International Congress on High-Speed Imaging and Photonics*, 7126:712612–712612–10, 2008.

[139] M. I. Charnotskii. Superresolution in dewarped anisoplanatic images. *Applied Optics*, 47:51105116, 2008.

[140] M. Elad and A. Feuer. Restoration of a single superresolution image from several blurred, noisy, and undersampled measured images. *IEEE Transactions on Image Processing*, 6(12):1646–1658, 1997.

[141] S.C. Park, M.K. Park, and M.G. Kang. Super-resolution image reconstruction: a technical overview. *IEEE Transaction on Signal Processing,*, 20(3):21–36, 2003.

[142] Z.Y. Wen, F. Li, D. Fraser, A. Lambert, and X.P. Jia. A super resolution algorithm for atmospherically degraded images using lucky regions and map-uhmt. *IEEE International Conference on Digital Imaging Computing: Techniques and Applications (DICTA)*, pages 1–8, 2009.

[143] F. Li, X. Jia, and D. Fraser. Universal HMT based super resolution for remote sensing images. *Proc. ICIP 2008*, pages 333–336, October 2008.

[144] J. K. Romberg, H. Choi, and R. G. Baraniuk. Bayesian tree-structured image modeling using wavelet-domain hidden markov models. *IEEE Transactions on Image Processing*, 10(7):1056–1068, 2001.

[145] Z.Y. Wen, D. Fraser, A. Lambert, and H. Li. Bispectral analysis and recovery of images distorted by a moving water surface. *Applied Optics*, 49:6376C6384, 2010.

[146] Z.Y. Wen, H.D. Li, D. Fraser, and A. Lambert. Reconstruction of underwater image by bispectrum. *ICIP*, 3:545–548, 2007.

[147] Z.Y. Wen, A. Lambert, and D. Fraser. Reconstruction of imagery reflected from water surface. *In Signal Recovery and Synthesis, Optical Society of America Technical Digest (OSA)*, pages 1–3, 2007.

[148] C. Cox and W. Munk. Slopes of the sea surface deduced from photographs of sun glitter. *Scripps Inst. of Oceanogr*, 6:401–479, 1956.

[149] A. Efros, V. Isler, J. Shi, and M. Visontai. Seeing through water. *NIPS*, pages 1–8, 2004.

[150] M.L. Hoolohan and J.C. Dainty. Low-order adaptive optics: a possible use in underwater imaging? *Optics and Laser Technology*, 29:51–55, 1997.

[151] H. Murase. Surface shape reconstruction of a nonrigid transparent object using refraction and motion. *IEEE Transaction on Pattern Analysis and Machine Intelligence*, 14:1045–1052, Oct. 1992.

[152] A. Donate and E. Ribeiro. Improved reconstructin of images distorted by water waves. *International conference on computer vision theory and applications*, 4:264–277, 2006.

[153] A. Donate, G. Dahme, and E. Ribeiro. Classification of textures distorted by water waves. *ICPR*, pages 421–424, 2006.

[154] D. M. Milder, P. W. Carter, N. L. Flacco, B. E. Hubbard, N. M. Jones, K. R. Panici, B. D. Platt, R. E. Potter, K. W. Tong, and D. J. Twisselmann. Reconstruction of through-surface underwater imagery. *Waves in Random and Complex Media*, 16:521–530, 2006.

[155] Z.Y. Wen, D. Fraser, and A. Lambert. Reconstruction of atmospherically degraded images using a sparse prior. *Applications of Digital Image Processing, Proceeding of Society of Photo-Optical Instrumentation Engineers (SPIE)*, 7073:70731P–70731P–8, 2008.

[156] Z.Y. Wen, D. Fraser, and A. Lambert. Image restoration using natural image statistics. *In Signal Recovery and Synthesis, Optical Society of America Technical Digest (OSA)*, pages 1–3, 2009.

[157] Wikipedia the free encyclopedia. Nyquist-shannon sampling theorem. *http://en.wikipedia.org/wiki/Nyquist-Shannon_sampling_theorem*.

[158] Wikipedia the free encyclopedia. Compressed sensing. *http://en.wikipedia.org/wiki/Compressed_sensing*.

[159] E. Candès, J. Romberg, and T. Tao. Robust uncertainty principles: Exact signal reconstruction from highly incomplete frequency information. *IEEE Trans. Inform. Theory*, 52:489–509, 2006.

[160] E. Candès, J. Romberg, and T. Tao. Stable signal recovery from incomplete and inaccurate measurements. *Communications on Pure and Applied mathematics*, 58:1207–1223, 2005.

[161] E. Candès and J. Romberg. ℓ_1-magic: recovery of sparse signals via convex programming. *Compressive Sensing Tutorial*, pages 1–19, Oct. 2005.

[162] E. Candès and T. Tao. Near optimal signal recovery from random projections: universal encoding strategies? *IEEE Trans. Inform. Theory*, 52:5406–5425, Dec. 2006.

[163] E. Candès. The restricted isometry property and its implications for compressed sensing. *Compte Rendus de l'Academie des Sciences*, 346:589–592, 2008.

[164] Y. Weiss. Deriving intrinsic images from image sequences. *ICCV*, pages 68–75, 2001.

[165] J. Shen, X. Jin, and C. Zhou. Gradient based image completion by solving poisson equation. *Computers & Graphics*, 31(1):119–126, 2007.

[166] R. Fattal, D. Lischinski, and M. Werman. Gradient domain high dynamic range compression. *ACM Transactions on Graphics*, 21:249–256, 2002.

[167] R. Raskar, K. Tan, R. Feris, J. Yu, and M. Turk. Non-photorealistic camera: depth edge detection and stylized rendering using multi-flash imaging. *ACM Transactions on Graphics*, 23:679–688, 2004.

[168] A. Agrawal, R. Raskar, S.K. Nayar, and Y. Li. Removing flash artifacts using gradient analysis. *ACM Transactions on Graphics*, 24:828–835, 2005.

[169] W. Press, S. Teukolsky, W. Vetterling, and B. Flannery. Numerical recipes in C: The art of scientic computing. *Cambridge University Press*, 1992.